Integrated Hollow-Core Microcavity Arrays - Building Blocks for Optical Sensing and Quantum Information

by

Mohammadhossein Bitarafan

A thesis submitted in partial fulfillment of the requirements for the degree of

Doctor of Philosophy

in

Photonics and Plasmas

Department of Electrical and Computer Engineering
University of Alberta

Abstract

This thesis describes an experimental and theoretical study of a novel class of air-core microcavities on chips, monolithically fabricated by the controlled formation of delamination buckles within a-Si/SiO_2-based multilayer thin film stacks. First, arrays of dome-shaped microcavities were fabricated via buckling over circularly patterned low-adhesion films. The stress-driven self-assembly process produces cavities with highly predictable geometries matching with elastic buckling theory. Optical experiments revealed reflectance-limited finesse of $>10^3$, implying low roughness and minimal defects. These devices were aimed at operating in a fundamental mode regime; thus, mode volumes as low as $\sim 1.3\,\lambda^3$ and potential for single-atom cooperativity of $\sim$50 were achieved, making this type of cavities an interesting candidate for quantum-optics applications.

Next, the viability of providing open-access to the core of the buckled-dome microcavities was explored by fabricating dome-shaped microcavities intersecting with hollow waveguide channels. Optical studies showed that connection to channels had minimal adverse effects on the morphological symmetry of the aforementioned devices, especially at the center where the optical modes reside. This monolithic approach, accordingly, holds promise to enable the introduction of liquid or gaseous analytes into the core of this class of microcavities. The possibility for open-access to the cavity volume, along with good optical properties, makes these cavities good candidates for applications in sensing and cavity quantum electrodynamics (CQED).

The buckled upper mirror in the dome-shaped microcavities is inherently a flexible plate, which thus allows interesting options for tuning the resonance wavelength. Hence, comprehensive studies were carried out to analytically and experimentally examine the temperature dependence of the resonance wavelength of the buckled microcavities. Aiming to explore

their potential for optomechanical studies, the effective spring constant and mechanical mode frequencies of the buckled domes were also experimentally and theoretically studied.

Related to their thermal tunability, absorption by the mirror layers of light circulating inside the core of dome-shaped cavities at or near resonance gives rise to nonlinear effects. For optical input powers in the μW range, we observed bistability in the output transmission spectra of the above-mentioned resonators. This behavior, which we showed to arise mainly due to photothermal effects, was studied analytically using first-order approximations, and the predictions were shown to be in good agreement with experimental results.

Finally, the buckling process was employed to fabricate a novel class of three-dimensional (3D) microcavities, in which the lateral confinement is provided by Bragg mirrors while axial (in-plane) confinement is provided by mode cutoff sections in the hollow waveguides. The cutoff sections were implemented as back-to-back dual tapers, which can be realized easily using the buckling-based fabrication processes. Optical experiments on numerous dual-tapers confirmed high reflection in wavelength ranges subject to cutoff, and high transmission at shorter wavelengths. Thus, the dual tapers can be used as a novel type of waveguide-based short-pass filter. Additionally, 3D microcavities were fabricated by cascading two dual-taper waveguides. Optical experiments revealed $Q > 10^4$ along with mode volume $\sim 100\,\lambda^3$, which promises a cooperativity of $C > 1$, making them of great interest in quantum information studies. Furthermore, this approach to forming axially varying hollow waveguides on chips is expected to provide new strategies for controlling the dispersion and confinement of light within optofluidic and CQED systems.

Preface

A version of Chapter 1 of this thesis has been published as M. H. Bitarafan and R. G. DeCorby, "On-chip high-finesse Fabry-Perot microcavities for optical sensing and quantum information," *Sensors*, vol. 17, no. 8, p. 1748, 2017. I was responsible for primary manuscript preparation, while R. G. DeCorby defined the research path, provided relevant articles and guidance, and worked to improve the flow of the manuscript.

Chapter 4 of this thesis has been published as M. H. Bitarafan, H. Ramp, T. W. Allen, C. Potts, X. Rojas, A. J. R. MacDonald, J. P. Davis, and R. G. DeCorby, "Thermomechanical characterization of on-chip buckled dome Fabry-Perot microcavities," *JOSA B*, vol. 32, no. 6, pp. 1214-1220, 2015. I was responsible for experimental measurements, data analysis and manuscript preparation. H. Ramp, X. Rojas, A. J. R. MacDonald and J. P. Davis helped in optomechanical measurements, and aided with manuscript edits. T. W. Allen helped in setup preparation as well as optical measurements, and also aided in manuscript edits. R. G. DeCorby who was the supervisory author helped in spring constants derivations and manuscript composition.

Chapter 5 of this thesis has been published as M. Bitarafan, H. Ramp, C. Potts, T. Allen, J. Davis, and R. DeCorby, "Bistability in buckled dome microcavities," *Optics letters*, vol. 40, no. 22, pp. 5375-5378, 2015. I was responsible for optical measurements and analysis. I was assisted by H. Ramp, C. Potts, and T. Allen in optical measurements, and manuscript edits. J. Davis helped in manuscript edits. R. G. DeCorby was the supervisory author and was involved in concept formation, theoretical modeling and manuscript preparation.

Chapter 6 of this thesis has been published as M. H. Bitarafan, C. A. Potts, and R. G. DeCorby, "Cutoff-based dual-taper reflectors in on-chip hollow waveguides," *Optics Express*, vol. 25, no. 5, pp. 5101-5106, 2017. I designed and fabricated the devices and performed all

of the experimental and theoretical studies. I was assisted with fabrication and manuscript edits by C. A. Potts. R. G. DeCorby was the supervisory author and was involved in concept formation and manuscript composition.

"And unto everyone who is conscious of God, He [always] grants a way out [of unhappiness], and provides for him in a manner beyond all expectation; and for everyone who places his trust in God, He [alone] is enough."
– Holy Quran-65:2,3

To Zahra

Acknowledgements

I wish to express my sincere thanks to Dr. Ray DeCorby, whose ideas, hard work, and mentorship provided the impetus for this thesis. Your humility, calmness, and guidance helped to build my self-esteem, allowing me to pursue my own interests within the framework of a vibrant research group. Your consistent encouragement allowed me to remain on the path towards success despite the numerous inevitable failures and difficulties arising from the experimental nature of our work. Through your guidance and wisdom, I learned what it means to be a world class researcher, and developed professional attitudes which I will carry with me throughout my future career and life. For this I will be eternally grateful.

To all the past and present members of the Integrated Optics Lab, I owe many thanks to you for making a pleasant and friendly environment for the completion of this thesis. I am indebted to Dr. Trevor Allen, for valuable advice relating to experimental optics, and for his expertise in the laboratory. I am thankful to Aaron Melnyk and Clinton Potts for countless hours spent assisting in device fabrication and their willingness to collaborate. I would also like to extend my thanks to Dr. Seyed Azmayesh-Fard, Timothy Harrison, Sanaa Al-Sumaidae, James Maldaner, Graham Hornig, and Danny Pulikkaseril.

I gratefully acknowledge Dr. John Davis at the Department of Physics for providing the opportunity to collaborate with his group. In particular, I would like to extend my thanks to Hugh Ramp for assisting in optomechanical studies on buckled cavities.

Thanks are also due to the entire nanoFAB staff for their direct and indirect assistance throughout my research work. I would like to specially thank Scott Munro, Les Schowalter and Aaron Hryciw.

Thanks to Pinder Bains for her patience and help in administrative part of my graduate studies.

To my wife, Zahra Sohrabi, I owe a debt of utmost gratitude, for her constant love, sacrifice, and infinite patience. Without your support throughout my graduate studies, it would have truly been impossible for me to accomplish what I have today. Thanks to my beloved son, Mobin, for accompanying me on this journey, and providing a source of overwhelming joy as I have watched him grow.

I am supremely thankful to my parents for their unconditional love, support, and encouragement. You have always sincerely supported me to achieve my goals and I can never thank you enough. I would like to extend my gratitude to my brothers, Reza and Amin, and my in-laws for their support and encouragement.

Thanks to all my friends, who supported and encouraged me through my time in graduate studies. I am profoundly thankful to Hamidreza Anvari for being my life-long friend, being fully supportive, and offering gentle encouragement whenever I was under pressure and frustrated. I am also deeply grateful to Ali Habibi and Fatemeh Jafari for their unwavering support and friendship over the course of my PhD program. Thanks to Pooria Joulani, Hossein Izadi, Mojtaba Izadi and their families for helping us in settling down both upon arrival in Edmonton, and later on.

I would like to acknowledge the financial support of Natural Sciences and Engineering Research Council (NSERC) and the University of Alberta, which facilitated this research.

Lastly, this research benefited from the acts of many others throughout my graduate studies whose names have been missed. However, I am very grateful for their help and they have my eternal thanks.

Contents

List of Figures

List of Tables

List of Symbols and Abbreviations

Symbols

a	Radius of a circular buckle
A	Absorptance of a film or Bragg mirror
A_{B}	Area of a circular buckle
b	Half-width of delamination buckle
b_0	Half of critical width
c	Speed of light
c_ρ	Specific heat capacity
C	Single-atom cooperativity; Constant heat capacity
C_{E}	Coupling efficiency
d_{eff}	Effective thickness of a waveguide core
d_{H}	Thickness of the higher index layer in a Bragg mirror
d_{L}	Thickness of the lower index layer in a Bragg mirror
d_{P}	Phase penetration depth
D	Flexural rigidity of a plate
E	Young's modulus
F_{R}	Radiation pressure force
F_{P}	Purcell factor
F_{PT}	Effective photothermal force

$\mathcal{F}$	Finesse
$\mathcal{F}_{\mathrm{D}}$	Defect finesse
$\mathcal{F}_{\mathrm{eff}}$	Effective finesse
$\mathcal{F}_{\mathrm{p}}$	Parallelism defect finesse
$\mathcal{F}_{\mathrm{R}}$	Reflection finesse
$\mathcal{F}_{\mathrm{rms}}$	Surface irregularities finesse
$\mathcal{F}_{\mathrm{s}}$	Spherical deviation finesse
g_0	Atom-cavity coupling rate
G_{TH}	Minimum required threshold gain
G	Energy release rate in a circular buckle (Chapter 2)
G	Constant thermal conductance (Chapter 5)
G_0	Stored energy per unit area in unbuckled film
G_{A}	Conduction through air-gap between a buckled mirror and substrate
G_{P}	Conduction through boundaries of a circular buckle
$\bar{G}$	Energy release rate averaged over curved end of buckle
h	Thickness of the buckled plate (Chapters 2, 4 and 5)
h	Height of the tunneling section in dual-taper waveguides (Chapter 6)
$\hbar$	Reduced Planck constant
H	Height of the guiding section in dual-taper waveguides
H_l, H_q	Hermite polynomial
I_i	Intensity of light incident on a resonator
I_t	Intensity of light transmitted through a resonator
k	Wavenumber

k_0	Wavenumber in free space
k_y	Transverse propagation constant in a waveguide
k_z	Modal propagation constant in a waveguide
k_B	Boltzmann constant
k_Si	Extinction coefficient of silicon
$\ker'$	First derivative of the Kelvin-real function
$K_\mathrm{B,P}$	Effective spring constant of circular buckle for point load
$K_\mathrm{B,U}$	Effective spring constant of circular buckle for distributed load
K_eff	Effective spring constant
K_F	Coefficient of finesse
$K_\mathrm{S,P}$	Effective spring constant of a shell for point load
$K_\mathrm{S,U}$	Effective spring constant of a shell for distributed load
l	Length of the tunnel section in a dual-taper waveguide
L	Length of a Fabry-Perot cavity
L_B	Phase shift coefficient of the bottom mirror in Bragg waveguides
L_eff	Effective length of a Fabry-Perot cavity
$L_p^{\lvert l\rvert}$	Laguerre polynomial
L_T	Phase shift coefficient of the top mirror in Bragg waveguides
m	Longitudinal mode order
m_B	Total mass of a circular buckle
m_eff	Effective mass
$m_{\mathrm{eff},n}$	Effective mass relating to vibrational mode of order n
n	Refractive index

n_0	Refractive index of the incident medium
n_s	Refractive index of the substrate
n_H	Refractive index of the higher index layer in a Bragg mirror
n_L	Refractive index of the lower index layer in a Bragg mirror
N	Number of discrete wavelengths in a measurement
N_0	Critical atom number
n_g	Group refractive index
n_eff	Effective refractive index
P_0	Input power
P_cav	Power of bidirectional component of standing wave inside a Fabry-Perot cavity
P_in	Coupled input power
P_T	Output power of a cavity
Q	Quality factor
r_B	Field reflection amplitude of bottom mirror in hollow core waveguides
r_T	Field reflection amplitude of top mirror in hollow core waveguides
R	Resolution; Reflectance
R_B	Reflectance of the bottom mirror
R_D	Radius of curvature of a dome with identical height and diameter with those of a circular buckle
R_S	Radius of curvature of a shell
R_T	Reflectance of the top mirror (Chapter 2)
R_T	Radius of curvature of a circular fit to the top of a circular buckle (Chapter 4)
S	Sensitivity

S^*	Time-normalized sensitivity
t	Length of a tapered waveguide
T	Transmittance of a film or Bragg mirror
T_{C}	Transmission of Fabry-Perot cavity
T_{T}	Overall transmission
$T_{\mathrm{T,max}}$	Maximum transmission of a cavity
U_0	Energy release per unit area in unbuckled regions
U_{f}	Energy release due to plastic deformation of film
U_{fric}	Energy release due to friction
U_{s}	Energy release due to plastic deformation of substrate
$\bar{U}$	Average energy per unit area in buckled regions
V_{M}	Mode volume
w	Width of the tunnel section in a dual-taper waveguide
w_0	Waist radius of a Gaussian beam
w_1	Radius of the circularly symmetric, concentrated load applied to the center of a shell
w_{I}	Mode field radius of the focused input beam
$w(z)$	Beam spot size
W	Width of the guiding section in a dual-taper waveguide
W_{A}	True work of adhesion
z_0	Rayleigh range
α	Coefficient of thermal expansion
α_m	Modal intensity attenuation factor
β	Spontaneous emission coupling factor

β_{C}	Complex modal propagation constant in a waveguide
γ	Non-resonant decay rate of the atomic dipole
γ_{C}	Rate of emission into the cavity mode at resonance
γ_{f}	Surface energy of film
γ_{fs}	Energy of the interface of a film and a substrate
γ_{s}	Surface energy of substrate
Γ	Optical confinement factor; Energy confinement factor
Γ_{21}	Free-space spontaneous emission rate
Γ_{t}	Interface toughness
δ	Peak height of a circular buckle
δ_{p}	Parallel deviation
δ_{rms}	Root-mean-square deviation
δ_{s}	Spherical deviation
$\delta\lambda_{\mathrm{D}}$	Detuning from the resonance wavelength of cavity
$\Delta(r)$	Profile of a circular delamination buckle
$\Delta\delta$	Change in height of a circular buckle
$\Delta\Theta$	Change in temperature
$\Delta\lambda_0$	Resonance wavelength shift in a cavity
$\Delta\lambda_{\mathrm{B}}$	Spectral width of the stop-band of a Bragg mirror
$\Delta\lambda_{\mathrm{T}}$	Wavelength spacing between non-degenerate transverse spatial modes
$\Delta\lambda_{\mathrm{min}}$	Minimum detectable spectral shift
Δf	Single-measurement noise bandwidth
Δn	Refractive index change

Δn^*	Refractive index change associated with a signal-to-noise ratio of unity
ΔL	Change of height in a Fabry-Perot cavity
$\Delta\theta$	Change in single-pass phase shift
$\Delta\Omega$	Effective solid angle spanned by the resonant cavity mode
$\Delta\omega$	Spectral width of the resonant mode
ϵ_0	Vacuum permittivity
$\zeta(z)$	Gouy phase of Gaussian beam
θ	Single-pass phase shift minus nearest multiple of 2π
θ_{B}	Brewster's angle
Θ	Temperature
κ	Photon decay rate of the cavity (Chapters 1 and 3)
κ	Thermal conductivity (Chapter 5)
κ_0	Rate of photon emission into a desired output channel
κ_{L}	Rate of photon loss
λ_0	Free-space resonant wavelength of a Fabry-Perot cavity
λ_{B}	Center wavelength of a Bragg mirror
λ_{C}	Resonance wavelength of an unperturbed cavity (Chapter 5)
λ_{C}	Cut-off wavelength of a Bragg waveguide (Chapter 6)
λ_{f}	Free spectral range
λ_m	Resonance wavelength of mode number m
μ	Electric dipole moment of atomic transition
ν	Poisson's ratio
ν_{f}	Free spectral range
ν_m	Resonance frequency of mode order m

ρ	Radius of curvature
ρ_0	Minimum radius of curvature of a circular buckle
ρ_d	Density of a thin film
σ	Pre-buckling stress of a film
σ_c	Critical stress
τ_{21}	Free-space spontaneous emission lifetime for atomic transition
τ_P	Photon life time of the cavity mode
ϕ	Single-pass phase shift; azimuthal angle in a cylindrical coordinate system
ϕ_m	Bouncing angle in a waveguide for mode m
Φ_B	Phase-shift on reflection from the bottom mirror in hollow waveguides
Φ_T	Phase-shift on reflection from the top mirror in hollow waveguides
χ	Coefficient of cavity height change with input power
ψ	Potential transmittance
$\psi(x, y, z)$	Wave amplitude of transverse wave profile
$\omega_{\mathrm{B},1}$	Lowest order vibrational frequency of a circular buckle
ω_cav	Resonance frequency of an unperturbed cavity
$\omega_{\mathrm{P},n}$	Natural vibrational frequencies of a thin, flat, and clamped circular plate
$\omega_{\mathrm{S},n}$	Natural vibrational frequencies for a shallow shell
Ω_R	Single-photon Rabi frequency

Abbreviations

a-Si	Amorphous silicon
ARROW	Anti-resonant reflecting waveguide
CTE	Coefficient of thermal expansion
CW	Continuous wave
DBR	Distributed Bragg reflector
DL	Detection limit
DRIE	Deep reactive ion etching
ENZ	Epsilon near zero
FC	Fluorocarbon
FDTD	Finite difference time domain
FIB	Focused ion beam
FOM	Figure of merit
FOM_D	Device-specific figure of Merit
FPC	Fabry-Perot cavity
FSR	Free spectral range
FWHM	Full width at half maximum
HWHM	Half width at half maximum
LG	Laguerre Gaussian
LOC	Lab on a chip
MEMS	Microelectromechanical systems
MOEMS	Micro-opto-electro-mechanical systems
ODD	Optical differential detection
OSA	Optical signal analyzer

PBG	Photonic crystal bandgap
PDMS	Polydimethylsiloxane
PhC	Photonic crystal
PLD	Phase lock-in detection
QWS	Quarter-wave stack
RI	Refractive index
RIU	Refractive index unit
RoC	Radius of curvature
TE	Transverse electric
TM	Transverse magnetic
SNR	Signal-to-noise ratio
SOI	Silicon on insulator
SPR	Surface plasmon resonator

Chapter 1

Introduction[1]

1.1 Overview

In its simplest form, the Fabry-Perot cavity (FPC) confines light between two planar and parallel mirrors. Its historical importance to optics and photonics (and in fact physics) is difficult to overstate. Owing to its higher resolving power and light throughput compared to diffraction grating instruments [1], the FPC played a central role in early studies of the fine structure of spectral lines [2]. In the modern era, the FPC (in one form or another) has provided the predominant means for optical feedback and spectral discrimination in lasers. Moreover, the FPC is often employed as an archetype for the description and understanding of other optical resonators (*e.g.*, ring and photonic crystal resonators), which exhibit analogous properties.

An important figure-of-merit (FOM) for the FPC is the finesse ($\mathcal{F}$), which essentially quantifies the average number of times that a resonant photon bounces back-and-forth (*i.e.*, the average number of round trips) between the mirrors, prior to being absorbed, scattered, or transmitted out of the cavity. While ultimately limited by the mirror reflectance, the finesse is typically determined in practice by non-idealities such as non-parallelism between the mirrors and the non-plane-wave nature (*i.e.*, divergence) of the incident light [3]. Historically, macroscopic planar-mirror FPCs have been limited to $\mathcal{F}$ on the order of 100. While quality factor (Q) and thus resolving power can be increased by increasing the mirror spacing (*i.e.*, since $Q \sim m\mathcal{F}$, where m is the mode order), this is at the expense of a reduction in free-spectral-range (FSR) and an increase in mode volume (V_{M}), the latter of which is a

[1] A version of this chapter was published in *Sensors*, vol. 17, no. 8, p. 1748, 2017.

critical FOM for many of the applications discussed below [4]. In the past few decades, the development of microelectromechanical systems (MEMS) processes has enabled the scalable fabrication of FPCs on chips. Nevertheless, planar-mirror MEMS-based FPCs are prone to essentially the same finesse-limiting factors as their macroscopic counterparts [5].

Many of the shortcomings of the planar FPC can be mitigated by the use of intentionally curved (often spherical) mirrors, first studied and developed for gas lasers [2]. With appropriate choice of mirror spacing and curvature, the spherical-mirror FPC (one or both mirrors can be curved) can support stable 3-dimensionally confined fields, mathematically described by the Hermite-Gaussian or Laguerre-Gaussian families of modes [6]. As early as 2000, researchers had reported [7] macroscopic spherical-mirror FPCs with $\mathcal{F} > 10^5$, by using ultra-smooth substrates and ultra-low-loss dielectric 'supermirrors'. However, those cavities were characterized by relatively large mode volumes [4], due to practical tradeoffs between the mirror curvature, aperture, and spacing. Driven by applications in fiber communications, MEMS-based spherical-mirror FPCs were developed in the late 1990s [8], and commercial devices reportedly achieved $\mathcal{F} > 10^3$ [9, 10].

As described below, many emerging applications in sensing and quantum information require cavities that simultaneously provide high Q and low V_{M}. Compared to other types of micro-cavities, the 'air-gap' FPC provides additional compelling advantages: it is inherently tunable through adjustment of the mirror spacing (*i.e.*, cavity length) and it can provide open-access (for analytes or atomic emitters, *etc.*) to the high-field regions of the cavity mode, which resides primarily in the space between the mirrors. These factors have driven a significant effort towards the realization of micro-scale, curved-mirror FPCs, using techniques such as focused-ion-beam (FIB) milling [11] or laser ablation [12] to form the curved surfaces. A popular approach, which has the significant advantage of providing a built-in means for light-coupling, is to fabricate one or both mirrors on the end-face of a single-mode optical fiber [12, 13]. Others have employed wafer-bonding approaches combined with precision alignment stages [14]. However, the realization of truly monolithic, curved mirror FPCs with high $\mathcal{F}$ and low V_{M} remains at a relatively nascent stage of development [15, 16].

In this Chapter, a primary goal is to summarize important applications in sensing and information science that can benefit from open-access FPCs, and in particular to review the

role that Q and V_{M} play in determining device performance. We also review recent efforts towards the integration of high $\mathcal{F}$, low V_{M} FPCs on (or at least with) chips containing other functional elements such as electrical and magnetic wiring. Since these efforts are at a relatively early stage of development (and also in the interest of providing appropriate context), both planar-mirror and non-monolithic approaches (*e.g.*, wafer bonding and fiber-on-chip strategies) are included in the discussion.

1.2 FPCs for sensing applications

1.2.1 Refractometric sensors - background

Optical refractive index (RI) detection is a commonly employed scheme for optofluidic sensing, owing to its potential for label-free, high-precision, and real-time detection. Thanks to their multi-pass nature, optical resonators can be used to enhance light-matter interactions, thereby improving sensitivity. A wide variety of optical resonators have been studied for RI detection including surface plasmon resonators (SPR) [17, 18], ring resonators [19, 20], fiber-grating-based cavities [21], and photonic crystal cavities [22, 23]. In all of these cases, resonant wavelengths are highly sensitive to changes in refractive index within some portion of the mode field. The change in refractive index can be induced by changes in temperature, pressure, *etc.*, or by the presence of some target analyte. For most microcavity sensors, light is confined primarily within a high index medium, for example by total-internal reflection, and only the evanescent portion of the mode field (outside the high index medium) interacts with the target analyte. Resonant cavity sensors of this type, for example whispering-gallery-mode-based sensors [24], can exhibit extremely high Q (which correlates with high sensitivity, up to a point, as discussed below). However, these cavities are not suitable for applications where tracking the entire volume of a sample is needed.

There are many sensing problems that can benefit from a stronger interaction between the cavity mode field and the analyte, including sensing of large particles such as cells [25] and sensing within weakly absorbing analyte media. One approach to 'bulk sensing' is to use hollow-core waveguides (including hollow fibers), which can simultaneously confine light and a gas- or liquid-phase medium within the same volume [26]. However, these waveguides typically need to be reasonably long ($\sim$2 cm) in order to attain a desirable signal-to-noise

ratio (SNR) for the detected index change. Alternatively, 'open-access' FPC sensors provide a platform for whole-body interactions between samples and a resonant optical field. As in any microcavity, the multi-pass nature of the light propagation can allow for high-SNR detection of minute changes in physical parameters, even for small device dimensions (*i.e.*, mirror spacing of a few microns). Most of the FPC RI sensors reported to date have employed fiber-based cavities, wherein the mirrors were deposited or bonded on the end facets of fibers [27]. However, fiber-based FPCs must be aligned with great precision, and misalignment errors combined with the lack of control over the divergence angle of the output beams can lead to low Q-factor [25,28–30]. In addition, fiber-based FPCs cannot be easily integrated onto microfluidic chips; several post-fabrication steps are typically required to make them fully compatible for lab-on-a-chip applications. Nevertheless, only a few examples of fully monolithic integrated FPCs for optofluidic RI sensing exist, as briefly reviewed below.

The sensing mechanism in FPC sensors is based on the relationship between the optical path length and the resonant wavelengths of the cavity. Indeed, any change in the optical path length, arising from changes in the refractive index of cavity medium and/or changes in the cavity length (*i.e.*, mirror spacing), will give rise to a shift in cavity transmission peak. Ignoring field penetration into the mirrors, this can be expressed [31]:

$$\frac{\Delta\lambda_0}{\lambda_0} \approx \frac{\Delta n}{n} + \frac{\Delta L}{L}. \tag{1.1}$$

Here, λ_0 is a resonant (*i.e.*, peak transmission) wavelength of the cavity. While exceptions exist, most FPC sensors employ an approximately fixed mirror spacing, so that changes in peak wavelength can be directly correlated to changes in the refractive index of the cavity medium. This is the scenario commonly known as refractometric (refractive-index, RI) sensing. A common FOM for refractometric sensors is the detection limit (DL), defined as the minimum detectable refractive index change (*i.e.*, DL $= \Delta n_{\text{min}}$). It can be expressed as DL $= R/S$ [24] where R and S are the resolution and sensitivity, respectively. The sensitivity is defined as $S = \Delta\lambda_0/\Delta n$, and is simply a measure of the resonant wavelength shift per unit refractive index change. To first-order, we can write $S = \Gamma\lambda_0/n_{\text{eff}}$ [24], where Γ is the optical confinement factor within the analyte volume (*i.e.*, the fraction of the optical

mode interacting with the analyte) and n_{eff} is an effective index for the resonant optical mode. For most sensors that employ evanescent-mode-field interactions (with SPR sensors being an exception [24]), sensitivity is relatively low because Γ is low. For the FPC sensor, Γ can approach 1 as implied by Eq. 1.1 (which neglects field penetration inside the mirrors), so that S can be significantly improved. Resolution is defined as the minimum spectral shift that can be accurately detected (*i.e.*, $R = \Delta\lambda_{\text{min}}$), and is ultimately limited by noise in the detecting apparatus.

Sensitivity (as defined above) has been commonly employed as a comparison metric for refractometric sensors. However, as discussed by Hu *et al.* [32], this quantity fails to account for the role of microcavity parameters such as Q and $\mathcal{F}$ in determining the limit of detection. Aside from cavity parameters, DL also depends on the particular characteristics (*e.g.*, wavelength resolution, noise characteristics, and noise bandwidth) of the detection instrumentation used for readout. In general, both intensity noise (*e.g.*, due to photodetector noise) and wavelength noise (*e.g.*, due to wavelength repeatability of the interrogation instruments) will impact the overall system performance. Hu suggested an alternative FOM, called the time-normalized sensitivity (analogous to the parameter 'detectivity', used to characterize photodetectors) [32]:

$$S^* = \sqrt{\frac{\Delta f}{N}}\frac{1}{\Delta n^*}, \tag{1.2}$$

where Δn^* is the refractive index change that produces a signal-to-noise ratio of unity, and $\Delta f/N$ is called the equivalent noise bandwidth of the detection system. For example, in a wavelength interrogation scheme using a tunable laser source or scanning spectrometer (see below), Δf is the single-measurement noise bandwidth and N is the number of discrete wavelength values at which measurements are made. Thus, S^* is a FOM that encapsulates characteristics of both the device (*i.e.*, the optical resonator) and the peripheral optical and electronic components (*i.e.*, laser, detector, *etc.*).

Readout of microcavity sensors is typically achieved using intensity interrogation, where the change in transmission of a fixed-wavelength laser source is monitored, or wavelength interrogation, where the peak wavelength is continuously monitored by scanning a tunable laser or spectrally selective detector across the microcavity resonance. For a given scheme,

it is possible to define a device-specific figure-of-merit ($\mathrm{FOM_D}$), which is determined solely by the characteristics of the microcavity (and not by the particular instrumentation used for interrogation). As an example, in a wavelength interrogation scheme (which is most common) operating in an intensity-noise-limited regime [32]:

$$S^* \propto \mathrm{FOM_D} = \frac{Q\Gamma\lambda_0}{n_g}, \tag{1.3}$$

where Q is the cavity quality factor, λ_0 is the peak (resonant) free-space wavelength, and n_g is the group refractive index of the cavity mode. Thus, the practical limit of detection for a microcavity sensor scales inversely with both Q and Γ, at least up to a point. For Q exceeding some maximum value (typically 10^5-10^6 [32, 33]), wavelength noise (in part arising from thermally induced variations in the resonant wavelength of the microcavity [24, 34]) becomes the limiting parameter. In other words, practical limitations of interrogation instruments (*e.g.*, the wavelength repeatability of tunable lasers, temperature variations in the microcavity, *etc.*) set an upper limit on the desirable microcavity Q, with further increases providing no significant improvement in the detection limit [24, 32, 33, 35]. Thus, while other microcavities can achieve higher Q values, the spherical-mirror FPC can easily provide the values required to maximize S^*, in addition to providing near-unity Γ. It should be also noted that, while Eq. 1.3 does not capture the impact of mode volume directly, a reduction in V_M is typically favorable for sensing applications, since it implies a smaller probed analyte volume (*i.e.*, detection of a smaller number of molecules, as discussed further below). Given its potential for moderate-to-high Q , high Γ, and low V_M, the spherical-mirror FPC is an intriguing candidate for applications in sensing. Efforts towards this goal have recently been described in the literature, and are briefly summarized in the following paragraphs.

1.2.2 Chip-based FPCs for refractometric sensing

Early work on volume refractometric FPC sensors employed relatively low finesse, planar-mirror FPCs, typically embedded within or on the end-facets of optical fibers. For example, Song *et al.* [25] used gold-coated fiber end-facet mirrors, hybrid-integrated onto a PDMS microfluidics platform, for the detection of single living cells. A similar refractometer was demonstrated by Domachuk *et al.* [21], but with fiber Bragg grating mirrors augmented by

graded-index fiber sections to provide light collimation between the fiber end facets. Chin *et al.* [36] also reported a similar device, and demonstrated optical trapping of a live cell within the cavity region. The same group later added liquid microlenses [37] for collimation of the light within the cavity. A related approach, but with integrated, vertical Bragg mirrors fabricated by deep reactive ion etching (DRIE) of silicon was described by St-Gelais *et al.* [38]. They reported a sensitivity of 907 nm/RIU (RI units) and DL $\sim$1.7 $\times$ 10^{-5} RIU [38]. The Q-factor of their FPC ($\sim$400) was limited by surface roughness and non-parallelism of the mirror sidewalls.

Other researchers have embedded vertical planar-mirror FPCs directly into microfluidic chips by using wafer-bonding processes. For example, Shao *et al.* [39] formed a dielectric-mirror FPC in a glass-based microfluidics platform, and applied it to the refractometric sensing of lymphocytes. A similar wafer-bonding strategy has been explored by a research group in China [40–42]. In their early work, wet etching on silicon-on-insulator (SOI) wafers was used to fabricate on-chip optofluidic channels, where the oxide layer functions as the etch-stop layer leading to smooth microchannel surfaces for mirror deposition. FPCs with mirror reflectance 75 % and $Q \sim 861$ were reported, enabling sensitivity of 1100 nm/RIU and DL $\sim 1.1 \times 10^{-5}$ [40]. Aiming to improve SNR and resolution, optical differential detection (ODD) method was later explored by the same group. The method is based on the spectral measurement of two cavities, one of which is filled with DI water as the reference. The refractive index change is monitored by tracking the power level at a wavelength tuned to the steepest point of the transmission spectrum associated with the water filled cavity. DL of 5.5×10^{-8} RIU was experimentally demonstrated [41]. In later work, surface roughness was further reduced by utilizing glass substrates, with the additional benefit that the operating wavelength of the refractometer could be extended to visible and ultraviolet regions. DL down to 2×10^{-9} RIU was reported for the all-glass biosensor fabricated by face-to-face bonding of HF-etched Ta_2O_5/SiO_2 Bragg coated glass substrates, with noise reduced by concurrent use of ODD and phase lock-in detection (PLD) [42].

Only recently researchers have begun to explore the use of curved-mirror FPCs for refractometric sensing [45]. In addition to enabling much higher Q than their planar-mirror counterparts, a primary motivation for this approach is that it can significantly reduce the

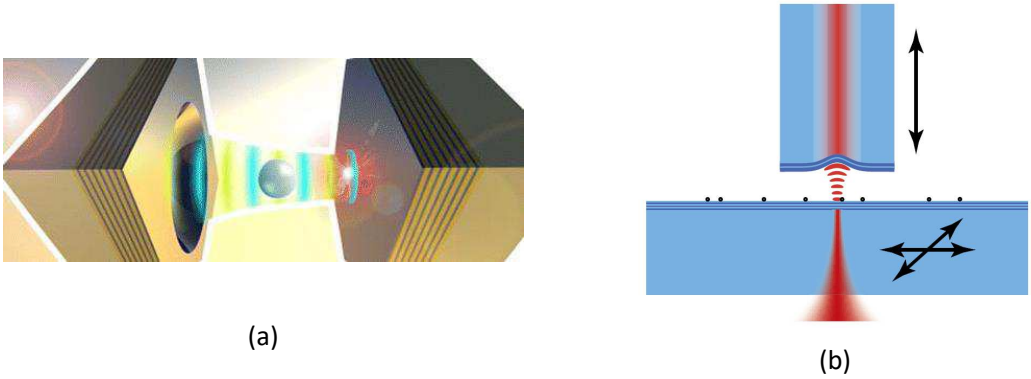

Figure 1.1: (a) Schematic representation of an open-access microcavity with a flat and a concave mirror. A nanoparticle in solution, trapped inside the optical mode is shown (taken from [43]). (b) Conceptual diagram of a laser-machined fiber with multilayer mirror on its end along with a flat mirror serving as a sample holder; black dots represent nanoparticles located on the flat mirror. (taken from [44]).

volume of the analyte needed to achieve a given sensitivity, since it employs low-V_{M} modes. For example, Trichet *et al.* [31] employed simultaneous tracking of resonance wavelengths in arrays of wafer-bonded, half-symmetric cavities, and achieved DL $\sim 3.5 \times 10^{-4}$ RIU correlated with the presence of $\sim 10^5$ glucose molecules in a 54 fL detection volume. The same group subsequently reported [43] the trapping and sensing of single nanoparticles, using spherical-mirror FPCs with $Q \sim 18000$ and $V_{\mathrm{M}} \sim 1.7\ \lambda^3$ at 560 nm wavelength (see Fig. 1.1(a)). In related work, Mader *et al.* [44] formed a high-finesse cavity using a spherical mirror on a fiber end-facet, which could be scanned to image and characterize nanoparticles attached to the opposite (planar) mirror of the cavity (see Fig. 1.1(b)). Finally, Kelkar *et al.* [46] used a low-V_{M} spherical mirror cavity to sense single nanoparticles. While at an early stage of development, spherical-mirror FPC sensors hold great promise for the detection of small particles, possibly even down to the single molecule level [31, 45]. The key FOMs of several reported FPCs used for refractometric sensing are summarized in Table 1.1.

1.2.3 Open-access FPC lasers

Monolithic integration of laser cavities within lab-on-a-chip (LOC) systems is a long-standing goal in the microfluidics research community. For example, monitoring of laser emission from such a cavity is a promising sensing modality in its own right [47]. The vast majority of lasers employ the FPC as an optical feedback element. The FPC, or any optical cavity,

Table 1.1: Summary of chip-based FPCs used for refractometric sensing

Ref.	Mirror type	Mirror material	Wavelength (nm)	Q	$\mathcal{F}$	S (nm/RIU)	DL (RIU)	V_{M} (λ^3)
[25]	Planar	Au	1550	330	5.2	-	$1.4 \times 10^{-3*}$	-
[21]	Planar	FBG	1550	-	-	6.825	$2.7 \times 10^{-3*}$	-
[36]	Planar	FBG	1258	-	-	32*	0.001	-
[37]	Planar	Au	1275	600*	18.79	960	0.01	-
[38]	Planar	Si/Air	1550	400	9*	907	1.7×10^{-5}	-
[39]	Planar	Au	890	900*	30	-	-	-
[40]	Planar	Ta_2O_5/SiO_2	1550	861	-	1100	1.1×10^{-5}	-
[41]	Planar	Ta_2O_5/SiO_2	1550	600*	14*	-	5.5×10^{-8}	-
[42]	Planar	Ta_2O_5/SiO_2	1550	875	3	650*	2×10^{-9}	-
[31]	Curved	TiO_2/SiO_2	640	-	1000	-	3.5×10^{-4}	-
[45]	Curved	TiO_2/SiO_2	640	10^5	4000	-	3.5×10^{-4}	3.8
[43]	Curved	TiO_2/SiO_2	640	18000	4500*	-	-	1.7
[44]	Curved	Ta_2O_5/SiO_2	780	1.57×10^6	57000	-	-	100*
[46]	Curved	TiO_2/SiO_2	745/785	300	70	-	-	0.8

* Estimated from related data in the paper.

plays a dual role in the laser. First, it enables the build-up of a high photon density within the optical gain medium, so that the stimulated emission rate can greatly exceed the spontaneous emission rate. Second, it acts as a frequency-selective element, determining one or more frequencies (within the gain bandwidth of the laser medium) at which lasing will occur. An early report of a FPC-based microfluidic laser was the work by Helbo *et al.* [48], which employed a relatively low-finesse cavity formed by wafer bonding of planar gold mirrors surrounding a microfluidic channel. Pulsed lasing was achieved, but with relatively high pump power requirements.

Generally speaking, there is an ongoing drive towards the development of small-scale lasers, typically enabled by photonic crystal or plasmonic resonator structures [49]. The goal is to produce lasers that can be embedded within LOC systems or even within biological systems. While such lasers typically generate relatively low output power, of greater importance is the fact that they might operate with relatively high efficiency and consume relatively low pump power [49]. A key FOM for the miniaturization of lasers is the minimum required threshold gain, which can be approximated [49, 50]:

$$G_{\mathrm{TH}} \approx \frac{2\pi n}{Q\Gamma\lambda}, \tag{1.4}$$

where Γ is the energy confinement factor (*i.e.*, the overlap factor) of the laser mode with the active gain medium and n is the refractive index of the cavity medium. As per the discussion above, the spherical mirror FPC can simultaneously provide moderate-to-high Q and $\Gamma \sim 1$. Moreover, the possibility for low V_{M} implies low pump energy requirements [49]

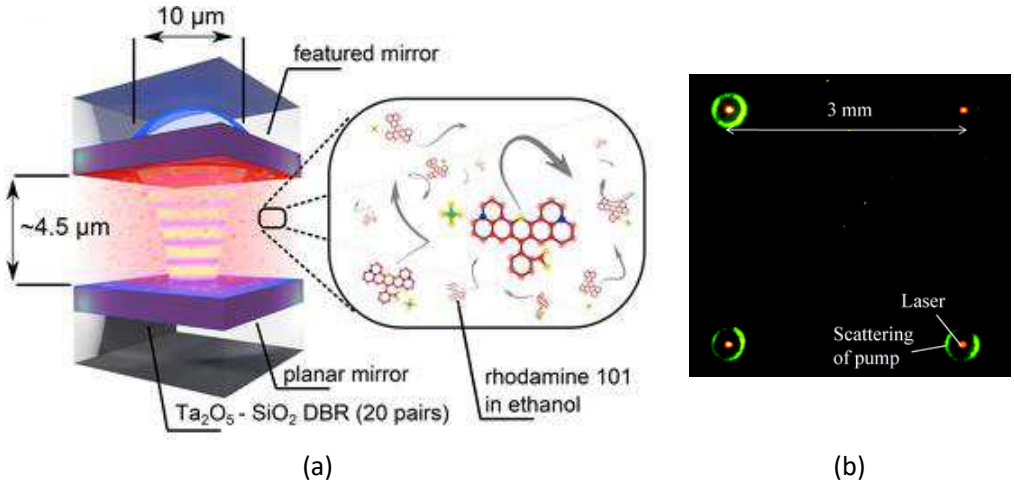

Figure 1.2: (a) Schematic representation of an open-access microcavity with a flat and a concave mirror filled with a rhodamine 101 solution (adapted from [51]). (b) Simultaneous laser emission from four spherical mirror FPCs (adapted from [52]).

and other benefits mentioned below.

The spherical-mirror, open-access FPC is emerging as a promising new platform for small-scale lasers, and is inherently well-suited for the implementation of microfluidic laser systems. An early example was the work by Patel *et al.* [53], who used a colloidal CdSe-based gain medium in a hybrid-assembled FPC chip. The same research group subsequently reported continuous-wave (CW) operation for similar laser cavities, using organic dye gain media. Typically, microfluidic pumping is required to achieve CW operation from dye-based lasers, since dye media are subject to rapid photobleaching effects. Conversely, Coles *et al.* [51] were able to achieve CW operation without pumping, owing to the diffusion of organic molecules into and out of the small V_{M} gain region of their spherical-mirror FPC (see Fig. 1.2(a)). In parallel with these efforts, a group in China [52, 54] has recently reported low-threshold dye lasers based on high-finesse ($\mathcal{F} \sim 10^3$) spherical-mirror FPCs fabricated using a wafer-bonding approach (see Fig. 1.2(b)). The field of spherical-mirror, open-access microcavity lasers is in its infancy, and promises to yield many exciting results in the coming years.

1.3 FPCs for cavity quantum electrodynamics applications

1.3.1 CQED - overview

Technologies that directly exploit quantum wave-functions are widely expected to lead to significant advances in computing [55], secure communications [56], sensing [57], and metrology [58]. Nevertheless, the current state of the art is best summed up as a "grand scientific challenge" [59]. Quantum technologies are predicated on:

(i) the ability to isolate quantum particles (*e.g.*, atoms) from the external environment - *i.e.*, to preserve quantum coherence on time-scales that are technologically useful, and;

(ii) the ability to address, control, and store quantum states, and to build scalable systems with large numbers of quantum particles ('qubits').

Optical cavities are firmly established as one of the most important tools for quantum information technologies [4, 60]. An optical cavity can greatly enhance the inherently weak interactions between light and matter, and effectively isolate an atom-photon system from the external environment [60, 61]. The study of atom-photon interactions in cavities is the domain of cavity quantum electrodynamics (CQED). CQED is expected to be a key enabler of a future 'quantum internet' [62], predicated on devices that mediate quantum entanglement between photons and atomic emitters [62, 63]. In such a network, quantum states (*i.e.*, qubits) are stored and processed at quantum nodes and optical connections enable nodes to distribute quantum entanglement across the network. It has been suggested that these networks might utilize arrays of tunable, open-access optical cavities on a single chip, into which atoms can be injected and trapped (for example, using magnetic or optical trapping methods) [60, 63].

A canonical Fabry-Perot-based CQED system is depicted in Fig. 1.3. Aside from being the archetypal CQED system, the curved-mirror FPC offers the same unique advantages mentioned in Section 1.1 (*i.e.*, tuning and open access to the cavity field for placement of atomic emitters). It is worth noting that photonic crystal cavities with air defect modes can also provide open access to the cavity mode field [64–66]. Excellent and comprehensive

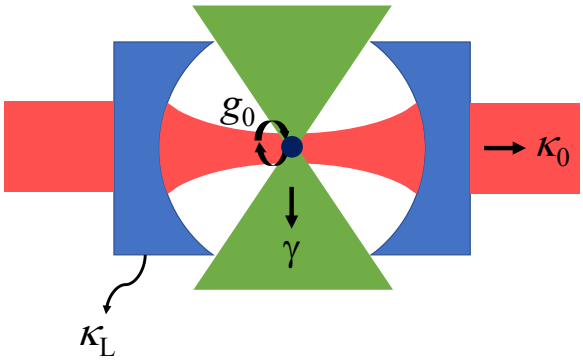

Figure 1.3: Schematic representation of a CQED system encompassing a single atom inside an FPC.

reviews of CQED are available [12, 60]. After a brief summary of a few key principles, our main goal below is to provide a survey of recent experimental work aimed at the construction of chip-integrated FPC arrays for CQED.

Interactions between atoms and photons within a cavity are governed by three rate parameters (see Fig. 1.3): the non-resonant decay rate of the atomic dipole (γ)(*i.e.*, the rate of atomic decay by emission into all modes other than the resonant cavity mode of interest), the photon decay rate of the cavity (κ), and the atom-cavity coupling rate (g_0). In keeping with most of the CQED literature [60,62], we define κ and γ as the half-width-at-half-maximum (HWHM) of the corresponding resonance line-shape plotted versus angular frequency. Thus, as discussed in more detail in Chapter 2, it follows that the cavity decay rate can be expressed [60]:

$$\kappa = \frac{\Delta\omega}{2} = \frac{1}{2\tau_P} = \frac{\pi c}{2L\mathcal{F}}, \tag{1.5}$$

where $\Delta\omega$ is the spectral width of the resonant mode and τ_P is the photon lifetime of the cavity mode. As depicted in Fig. 1.3, the decay rate can be divided into two parts, $\kappa = \kappa_0 + \kappa_L$ where κ_0 is the rate of photon emission into a desired output channel (typically by transmission through one mirror) and κ_L is the rate of photon loss (by transmission through the opposite mirror and by scattering and absorption in both mirrors).

The non-resonant decay rate γ encapsulates all processes, other than emission of a photon into the resonant cavity mode, by which the excited atom can relax towards its ground state. In the two-level-atom approximation, and neglecting the possibility of non-radiative relaxation (*e.g.*, due to collisions), γ is determined by the rate of spontaneous

emission into non-resonant modes [60]:

$$\gamma = (1 - \Delta\Omega/4\pi).(\Gamma_{21}/2). \tag{1.6}$$

Here, $\Delta\Omega$ is the effective solid angle spanned by the resonant cavity mode, $\Gamma_{21} = 1/\tau_{21}$ is the free-space spontaneous emission rate (*i.e.*, the Einstein A_{21} coefficient), and τ_{21} is the free-space spontaneous emission lifetime for the atomic transition. For conventional macroscopic FPCs, $\Delta\Omega$ is typically small, so that γ is nearly identical to half of the free-space decay rate of the atom. Wavelength-scale FPCs, however, can inhibit emission into non-resonant modes, as discussed further below.

The third parameter, the atom-cavity coupling rate, is essentially governed by the electric-dipole interaction between the atom and the cavity vacuum field (*i.e.*, the zero-point fluctuation of the electromagnetic field [67]). For a single two-level atom placed at the location of the maximum electric field of the cavity mode in an otherwise empty cavity, and with the cavity resonance tuned to match the atomic transition, g_0 can be expressed [60,67]:

$$g_0 = \sqrt{\frac{\mu^2\omega}{2\epsilon_0\hbar V_{\mathrm{M}}}}, \tag{1.7}$$

where μ is the electric dipole moment for the transition (assumed here to be aligned with the electric field polarization vector of the cavity mode [62]) and $V_{\mathrm{M}} \approx (\pi/4)w_0^2 L$ is the volume of the fundamental mode (see Chapter 2). Many fundamental studies of quantum coherence and entanglement are predicated on achieving so-called 'strong-coupling' conditions, in which the atom-cavity coupling rate exceeds both the cavity and atomic decay rates, *i.e.*, $g_0 \gg (\kappa,\gamma)$, where (κ,γ) represents the larger of κ and γ. In this regime, the atom and the cavity can exchange energy through repeated photon emission and absorption in a reversible fashion. For a single atom and a cavity initially in its vacuum state (no photons in the resonant mode), this energy exchange oscillates at the single-photon Rabi frequency $\Omega_{\mathrm{R}} = 2g_0$ [60]. In the frequency domain, this exchange manifests as a splitting of the cavity resonance, which becomes a double-peaked cavity transmission (vacuum-Rabi splitting [67]) with peaks centered at $\omega \pm g_0$. Aside from fundamental physics studies, strong-coupling CQED might enable a range of basic building blocks that rely on the observation of resolved coupled-system resonances (such as devices for coherent control and read-out of quantum

states [60]). Equation 1.7 indicates that for a given atomic transition, reduction of mode volume is the critical requirement for increasing g_0 and thus for achieving strong-coupling conditions. To date, the practical implementation of strong-coupled atom-cavity systems, especially in a scalable format, remains a significant challenge.

Fortunately, many important applications of CQED reside in the 'weak-coupling' regime, with $g_0 \ll (\kappa,\gamma)$. In this regime, an important dimensionless factor, known as the single-atom cooperativity, is defined as follows [60]:

$$C = \frac{g_0^2}{2\kappa\gamma}. \tag{1.8}$$

The inverse of the cooperativity, $N_0 = 1/C$, is termed the critical atom number [4] and can be interpreted as the number of atoms required to significantly modify the cavity field [62]. For the case that $C \ll 1$, the interaction between the atom and the electromagnetic field is not significantly modified by the cavity. In contrast, weak-coupling conditions that satisfy $\kappa \gg g_0 \gg \gamma$ and $C \gg 1$ are of great interest, and characterize the so-called "Purcell" regime. In this regime, photon emission is irreversible but nevertheless greatly altered relative to the free-space situation, due to modification of the photonic density of modes available to the emitting atom. The Purcell effect can be used to tailor and control spontaneous emission from an atom, such as by causing preferential emission into a desired resonant mode of the cavity [4]. It is the key parameter of interest for a range of novel light sources, including threshold-less lasers and single-photon sources.

In the Purcell regime, the cavity alters the density of photonic modes in a frequency-dependent fashion. Thus, depending on whether the atomic transition is resonant with a cavity mode or not, the rate of radiative emission is enhanced or suppressed, respectively, relative to the free-space rate. This modification was historically treated by Purcell using a semi-classical approach, with the essential results subsequently confirmed by rigorous quantum mechanical treatments [67]. For example, assuming an atom located at a field maximum (in an otherwise empty cavity, such that refractive index $n = 1$) and with its electric dipole aligned to the cavity mode field, and also assuming the atomic transition is exactly matched to a cavity resonance and with $\gamma < \kappa$ [46,68], then the enhancement of the

radiative decay rate is given by the so-called Purcell factor:

$$F_{\mathrm{P}} \equiv \frac{\gamma_{\mathrm{C}}}{(\Gamma_{21}/2)} = \frac{3}{4\pi^2}\frac{Q}{(V_{\mathrm{M}}/\lambda^3)}, \tag{1.9}$$

where γ_{C} is the rate of emission into the cavity mode at resonance. A high Purcell factor is of great interest for the realization of efficient quantum light sources (*e.g.*, low threshold lasers and single-photon sources), and requires a combination of high Q and low V_{M}. In light of this, it is not surprising that the Purcell factor can be directly related to the single-atom cooperativity from above. For example, using the free-space value for γ (*i.e.*, $\gamma = \Gamma_{21}/2 = \mu^2\omega^3/6\pi\epsilon_0\hbar c^3$ [67]), and assuming a perfectly resonant and aligned atom as above, it follows that $F_{\mathrm{P}} = 2.C$ [60]. A related FOM is the spontaneous emission coupling factor [60]:

$$\beta = \left(\frac{\kappa_0}{\kappa}\right).\frac{F_{\mathrm{P}}}{F_{\mathrm{P}}+1}, \tag{1.10}$$

which quantifies the fraction of emitted photons that are coupled into the desired output mode. β is a key efficiency metric for low-threshold lasers (see Section 1.2) and especially for single-photon-sources [60], and can approach unity for low-loss, high-C cavities. For a range of CQED applications, Eqs. 1.9 and 1.10 show that key requirements for the cavity are a small V_{M} (thus large g_0) and a small excess photon loss (*i.e.*, $\kappa_0 \gg \kappa_{\mathrm{L}}$). Furthermore, for full control of atomic emission, $\kappa \gg \gamma$ is required. In the case of solid-state emitters, which have relatively large γ, this implies that small V_{M} is particularly critical (*i.e.*, since increased κ implies reduced Q) [46, 68].

1.3.2 Chip-based FPCs for CQED

Early work on CQED employed macroscopic cavities, constructed from ultra-low loss dielectric mirrors deposited on super-polished spherical substrates. Finesse as high as $\sim 10^6$ was achieved [7], but the relatively large mirror 'radius of curvature' (RoC) and aperture typically implies higher-than-desirable mode waist and volume for these cavities. Moreover, this approach is not particularly scalable, due to the high cost and complexity of cavity fabrication and alignment. These limitations subsequently spurred efforts towards the miniaturization of FPC cavities, typically through the use of micro-machining techniques to form atomically smooth, small-RoC curved surfaces. In many cases, the FPC is

constructed with one or both mirrors bonded [69] or deposited [12] directly on the end facet of a single-mode optical fiber, which facilitates direct optical coupling between the cavity mode and the fiber mode. Nearly all cavities reported to date were constructed by aligning two separately deposited mirrors (*i.e.*, on two separate fibers or substrates), and thus employ non-monolithic processes. This can hinder scalability, and also creates challenges with respect to cavity noise and stability [14]. In the following, we briefly summarize micro-machining approaches that have been used to fabricate hybrid-integrated cavities, with some emphasis on recent efforts aimed at the eventual monolithic integration of mirrors and cavities with other functional devices.

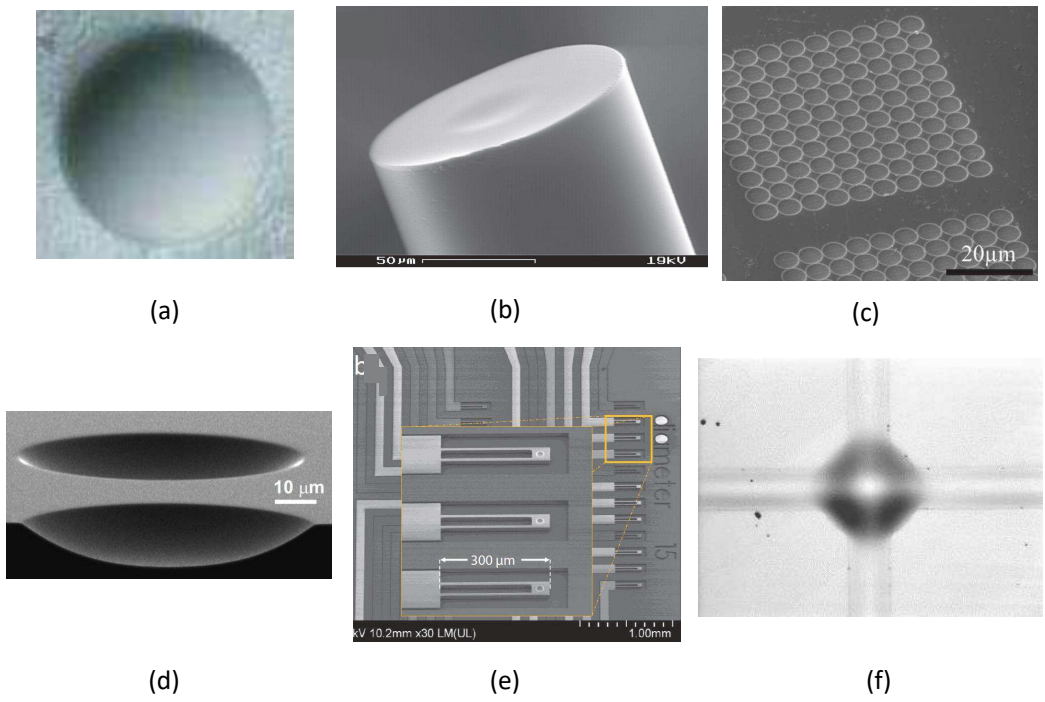

Figure 1.4: Microscope images of (a) a dimple with diameter of 200 µm formed by a bubble-trapping method [70], (b) a laser machined fiber end facet [12], (c) array of concave features made by FIB milling [11], (d) two silicon micro-mirrors fabricated by dry etching [71], (e) array of cantilever based micro-mirrors [72], (f) and a microscope image of a waveguide connected buckled-dome microcavity. The dome diameter is 100 µm.

A wide variety of micro-machining approaches have been employed to form small RoC mirrors. For example, early work by Prakash *et al.* [73] used electrochemical growth on a template of latex microspheres to form gold-based hemispherical mirrors. Cui *et al.* [70] employed a bubble-trapping method to form hemispherical surfaces on a glass substrate,

onto which a dielectric mirror was deposited (Fig. 1.4(a)). Steinmetz *et al.* [69] detached dielectric mirrors previously deposited on a spherical surface (ball lens or microlens) and glued them to the end of an optical fiber. Recently, however, the most popular techniques have involved standard micro-machining techniques such as CO_2 laser ablation (Fig. 1.4(b)) [12,74], focused ion beam (FIB) milling (Fig. 1.4(c)) [11], and dry etching (Fig. 1.4(d)) [71].

The etching approach was pioneered by Trupke *et al.* [75], and has the advantage of enabling the parallel fabrication of multiple concave surfaces. A two-cavity 'array' of this type was used for atom detection and photon generation [76]. Biedermann *et al.* [71] etched ultrasmooth surfaces in silicon to construct cavities with finesse as high as 64000 (Fig. 1.4(d)). FIB-based mirrors were originally reported by Dolan *et al.* [11]. While inherently a serial process, FIB milling can be used to fabricate large arrays of concave surfaces on a chip, with RoC as small as 5 µm or less and tailored morphology [31]. FIB-fabricated mirrors have enabled cavity finesse as high as 40000 [77]. Laser-ablation techniques are generally able to produce the smoothest concave features, owing to the melting and reflow of the machined glass surface. Muller *et al.* [13] achieved a finesse $> 10^5$, and similar results have been reported by others [12, 77]. Laser-ablated surfaces tend to be somewhat non-spherical, however, which can lead to mode-coupling loss [78] and polarization-dependence [79]. Moreover, control over the morphology, especially the relationship between feature depth and RoC, requires additional processing steps [80].

As mentioned, nearly all FPC micro-cavities developed for CQED to date have involved hybrid integration strategies. Nevertheless, some notable efforts towards monolithic integration (of at least one mirror) have been made. Purdy *et al.* [81] integrated a high-reflectance mirror with on-chip wiring for magnetic trapping of cold atoms and for temperature stabilization. They completed the cavity by hybrid alignment of a macroscopic curved mirror, and achieved a finesse $\sim 2 \times 10^5$. In another widely cited work [74], Colombe *et al.* integrated a fiber-based spherical microcavity onto a similar 'atom' chip containing magnetic trapping circuitry. Another notable work is that by Derntl *et al.* [72], in which curved mirrors (fabricated via dry etching) were integrated onto an array of individually tunable cantilevers on a silicon MEMS chip (see Fig. 1.4(e)). Cavities were formed by mating the cantilever array with flat mirrors formed on the end facets of an array of single mode fibers.

These examples illustrate that many options exist for hybrid integration of low V_{M}, high Q open-access cavities with other chip-based componentry. However, there are few options that promise fully monolithic integration of tunable high-finesse, open access microcavities on chips. Our group has reported a thin-film buckling approach [15, 16, 82, 83] with potential to address this latter point. We've shown that circular delamination buckles can be controllably formed within a multilayer thin film stack, and that these features can behave as half-symmetric Fabry-Perot cavities. The buckling self-assembly produces cavities with a high degree of geometrical perfection, characterized by cylindrically symmetric Laguerre-Gaussian modes and reflectance-limited finesse. Recently, Potts *et al.* reported arrays of these microcavities [16] with SiO_2/Ta_2O_5 Bragg mirrors, and exhibiting $\mathcal{F} \sim 3500$ and mode volume $\sim 35\,\lambda^3$. These cavities were designed for operation near 780 nm wavelength, and could be thermally tuned to the D2 transition of Rb. While the buckled cavities are inherently closed features, open access was demonstrated by FIB milling holes into the upper mirror. Even more recently, we reported Si/SiO_2-based cavities operating in fundamental mode regime with $V_{\mathrm{M}} \sim 1.3\lambda^3$ at 1550 nm wavelength and $Q \sim 1800$ [84]. These parameters correspond to a Purcell factor $F_{\mathrm{P}} \sim 100$, making these cavities of interest for CQED applications. Finally, that work also reported fabrication of channel-connected cavities by the same monolithic process (see Fig. 1.4(f)). Those cavities retain good optical properties while gaining an 'open-access' characteristic.

In summary, tremendous progress has been made towards the integration of high Q, low V_{M} FPCs at the chip scale. However, most of the reported work involves hybrid assembly of the FPCs, using precision alignment stages. The monolithic integration of complete FPC-based CQED systems (*i.e.*, full cavities along with magnetic control functions, *etc.*) onto single chips remains a challenge, and an intriguing avenue for future research. The key FOMs of several reported on-chip FPCs for CQED applications are summarized in Table 1.2.

Table 1.2: Summary of chip-based, curve-mirror FPCs proposed for CQED.

Ref.	Fabrication method	Mirror material	Wavelength (nm)	Q	$\mathcal{F}$	V_{M} (λ^3)	C
[69]	Deposition on microlens	TiO_2/SiO_2	780	-	1000	1260	2.1
[73]	Self-assembled templating	Au	747*	300	15	2.1	-
[70]	Bubble trapping	TiO_2/SiO_2	750	-	200	74*	-
[74]	Laser ablation	Ta_2O_5/SiO_2	780	-	37000	-	145
[71]	Dry etching	Ta_2O_5/SiO_2	780	-	64000	-	200
[39]	Wet etching	Au	780	10^6	6000	-	39
[11]	FIB milling	ZrO_2/SiO_2	637	10^4	460	8.5	10*
[13]	Laser ablation	Ta_2O_5/SiO_2	920	3.3×10^6	1.5×10^5	51	-
[80]	Laser ablation	Ta_2O_5/SiO_2	637	10^5	2.5×10^4	-	-
[81]	Dry etching	Ta_2O_5/SiO_2	780	$1.4 \times 10^{7*}$	2×10^5	-	50
[16]	Buckling delamination	Ta_2O_5/SiO_2	780	-	3500	35	32
[84]	Buckling delamination	Si/SiO_2	1550	1800	1800	1.3	50

* Estimated from related data in the paper.

1.4 Conclusions

We have reviewed the current state-of-the-art for chip-based, curved-mirror, Fabry-Perot cavities with applications in refractometric sensing, microlasers, and cavity QED. We have furthermore discussed the role of cavity finesse (or Q-factor) and mode volume in the performance of FPCs for the aforementioned applications, emphasizing the importance of high finesse and small mode volume. A high Q, small mode-volume FPC is predicated on 3D confinement of light using intentionally curved mirrors, which can mitigate finesse-limiting defects associated with conventional planar-mirror FPCs.

Various micro-machining techniques, such as FIB milling, CO_2 laser ablation, or isotropic etching, have been utilized to fabricate high-curvature surfaces at the micro-scale, either on the end facet of an optical fiber or on a wafer. These methods have recently been employed in the construction of curved-mirror FPCs for each of the application areas mentioned above; an overview of key experimental work was provided. In the vast majority of cases, the FPCs were implemented by means of hybrid assembly and positioning techniques, which creates challenges with respect to cost, stability, and scalability. There is a need for monolithically integrated, curved-mirror, open-access FPCs on chips, which will likely require that concepts from the micro-optical-electromechanical systems (MOEMS) literature [8] be adapted for requirements in sensing and CQED. This is a relatively unexplored approach and should be an interesting avenue for future exploration.

1.5 Summary of thesis

This thesis is an extensive study on a novel class of integrated microcavities having potential for applications in sensing and CQED. Two different types of microcavities were fabricated using a buckling self-assembly technique developed previously in Dr. DeCorby's group. The dome-shaped cavities described in Chapters 3-5 are a particular class of Fabry-Perot interferometers with curved Bragg mirrors. Contributions from this thesis related to these cavities can be viewed as a continuation on previous research works conducted in our group. However, the dual-taper waveguides described in Chapter 6 are based on a new idea, aimed at the possibility of attaining in-plane coupled, inherently open-access microcavities on a chip.

Chapter 2 outlines required background information about Bragg mirrors, omnidirectional reflectance, Fabry-Perot cavities, optical modes in spherical-mirror cavities, hollow waveguides, and the theory of elastic buckling delamination. Details about fabrication of devices presented in Chapter 3 and 6 are also described.

Chapter 3 presents small-mode-volume dome-shaped microcavities fabricated as part of this PhD work. Comprehensive studies on mode volume were carried out theoretically, numerically and experimentally. Additionally, channels connected to cavities are shown to provide open access to the core.

Chapter 4 investigates the thermomechanical characterization of buckled-dome microcavities fabricated by other group members in 2011. The study covers morphology, thermal tuning, mechanical and dynamic properties such as vibrational resonant frequencies of the buckled plate and effective spring constant of the buckled-dome microcavities.

Chapter 5 describes the nonlinearity of devices presented in the preceding Chapter. It is shown that photothermal effects lead to bistability in dome microcavities. This behavior was modeled to first order, and theoretical results were shown to be in good agreement with experimental results.

Chapter 6 proposes an alternative approach to fabricating in-plane coupled cavities in a fully monolithic fashion. In-plane reflection in this category of resonators is provided by cascading two dual-taper hollow waveguides operating in cutoff mode. The cutoff-based

mirrors offer high reflection, while not blocking the access to the cavity core. Comprehensive numerical and experimental studies on dual-taper waveguides are presented. Preliminary results on cavity structures fabricated based on dual-taper mirrors are also presented.

Chapter 2

Background theory and description of fabrication processes

This chapter provides background information pertaining to Bragg mirrors, omnidirectional reflectance, planar and curved mirror FPCs, and optical modes in spherical-mirror resonators. These are prerequisite materials to grasp the topics discussed in the Chapters 3, 4, and 5. The principle of operation of hollow waveguides is subsequently explained, as a basic introduction to Chapter 6. Next, a brief overview of key results from the theory of elastic buckling of thin films is provided, as context for related material in subsequent chapters. The Chapter ends with a brief description of the experimental processes used to fabricate buckled-dome FPCs and dual-taper waveguides, whose experimental data are presented in the remainder of the thesis.

2.1 Distributed Bragg reflectors

Mirrors are ubiquitously used in optical systems and are the building blocks of various components such as optical resonators and waveguides. There exist two main classes of mirrors in optics: (i) metallic, and (ii) dielectric mirrors. Notwithstanding that the former offer reasonably high reflectance (*e.g.*, $R_{\mathrm{Au}} \sim 0.993$ at 1550 nm [85]) and are useful in many applications, they are not particularly suitable for applications such as CQED and sensing where low-loss, high-finesse optical resonators are needed. In contrast, multilayer dielectric coatings, known as distributed Bragg reflectors (DBRs), can provide substantially higher reflectance up to $\sim$0.999 999 (six 9's) [86, 87], making them indispensable elements in low-loss hollow waveguides and high-finesse cavities.

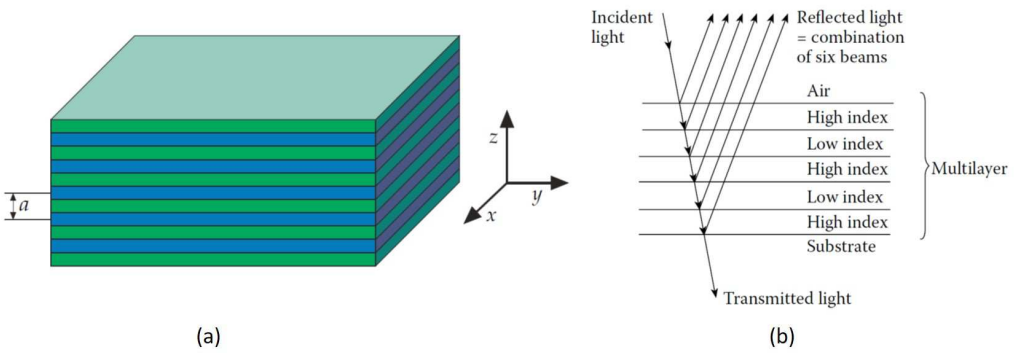

Figure 2.1: (a) Schematic representation of a one-dimensional photonic crystal with alternating layers of high and low refractive indices, with a period a along the z axis (adapted from [88]). (b) A multilayer as in (a), indicating the reflection of light at each surface (adapted from [89]).

A DBR, which is also well-known as a one-dimensional photonic crystal (PhC), consists of a stack of dielectric layers with alternating refractive index. The periodic boundary conditions result in a forbidden wavelength range known as a photonic band gap (PBG), over which light propagation is prohibited (see Fig. 2.1) [88]. A particular example of a DBR is a multilayer with dielectric layers of quarter-wave thicknesses, *i.e.*, $d = \lambda_B/4n$, where λ_B is wavelength in vacuum, and n is the refractive index of the layer. Such a multilayer is known as a quarter-wave-stack (QWS).

Consider a QWS multilayer as shown in Fig. 2.1(b) with a high index layer next to an air incident medium, and where the incident light is partially reflected at each boundary. The first reflected component undergoes a π shift due to 'external reflection', while the second one experiences a π phase shift due to a round-trip propagation in the first layer. The third component of light experiences a round-trip in two QWS layers in addition to an 'external reflection' leading to a total 3π phase shift. As such, all reflected components are subject to an effective phase shift of π at the incident boundary. Hence, all components at the interface of the first layer and air interfere constructively, which enables high reflectance at the Bragg wavelength determined by:

$$\lambda_B = 4n_L d_L = 4n_H d_H, \tag{2.1}$$

where n_H and n_L are the refractive indices of higher and lower index layers, respectively.

The peak reflectance of an N-period QWS with lossless layers is given by [89]:

$$R_{\text{Bragg}} = \left[\frac{1-(n_{\text{s}}/n_0)(n_{\text{L}}/n_{\text{H}})^{2N}}{1+(n_{\text{s}}/n_0)(n_{\text{L}}/n_{\text{H}})^{2N}}\right]^2, \tag{2.2}$$

where n_{L} is assumed to be the starting layer, n_{H} is the ending layer next to the exit medium, and n_0 and n_{s} are the refractive index of the incident and exit media, respectively. As can be seen, R_{Bragg} scales with N, which means a reflectance approaching unity is possible by increasing the number of layers. In practice, mirrors exhibit $R < 1$, as a consequence of residual absorption and scattering in the layers. In addition, another subtlety in Eq. 2.2 is the impact of the index contrast, say $(n_{\text{H}} - n_{\text{L}})$. In fact, the higher the index contrast in a QWS, the smaller the number of periods required for maximum possible reflectance $R_{\text{Bragg}} \sim 1$. For instance, a 4-period a-Si/SiO_2 mirror [82] exhibits virtually the same reflectance ($R \sim 0.999$) as a 10-period Ta_2O_5/SiO_2 multilayer [16].

As mentioned, a QWS mirror exhibits high reflectance over a range of wavelengths in the vicinity of λ_{B}, known as the stop-band. Given $R \sim 1$, from appropriate choice of material and N, the spectral width of stop-band can be expressed [89]:

$$\Delta\lambda_{\text{B}} = \lambda_{\text{B}}.\left(\frac{4}{\pi}\right).\sin^{-1}\left(\frac{n_{\text{H}}-n_{\text{L}}}{n_{\text{H}}+n_{\text{L}}}\right). \tag{2.3}$$

Their potential to simultaneously provide ultra-high reflection and low absorption have made QWS mirrors very important in optics and optoelectronics.

2.2 Omnidirectional reflectance

Metallic mirrors provide high reflection over a broad wavelength range for virtually all angles of incidence and all polarization states. This feature is known as 'omnidirectional reflectance'. Quite the contrary, Bragg mirrors are typically designed to reflect light over a narrow range of wavelengths, and from a single angle (*e.g.*, normal incidence) or a certain range of angles of incidence. Indeed, omnidirectional reflectance is not a general property of dielectric mirrors.

It was thought, in the past, that high reflection from a dielectric mirror at all angles and for all polarizations would require a complete three-dimensional photonic bandgap. Nonetheless, in 1998, Winn *et al.* showed that even a one-dimensional photonic crystal

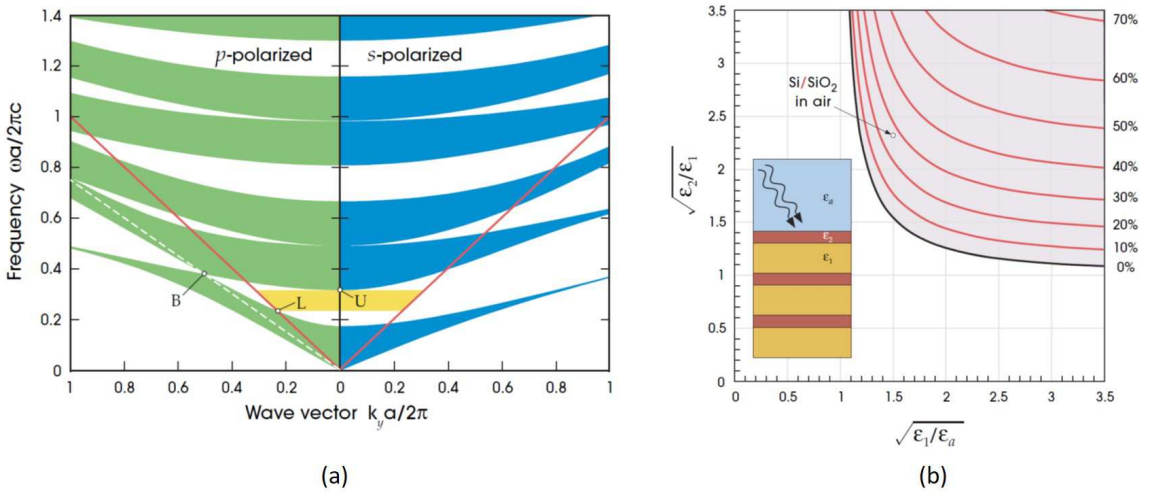

Figure 2.2: (a) Projected band structure for a QWS multilayer with $n_{\mathrm{L}} = 1.4$ and $n_{\mathrm{H}} = 3.6$. The right side indicates TE modes, while the left side TM modes. The straight solid (red) line is the light line $\omega = ck_y$. The dashed line represents the Brewster's angle. The yellow region indicates the first omnidirectional region (adapted from [88]). (b) The size of omnidirectional gap as a function of refractive index contrasts of the QWS. The shaded area represents the ratio of the omnidirectional bandwidth over the midband wavelength. In this plot dielectric constant is used instead of refractive index (adapted from [88]).

(*i.e.*, a dielectric multilayer stack) can exhibit omnidirectional reflection [90], provided that (i) the index contrast between the two constituent materials is adequately large, and (ii) the refractive index of the lower index layer is sufficiently larger than that of the incident medium (n_0) [88,90,91]. Figure 2.2(a) illustrates the band diagram of a QWS with $n_{\mathrm{L}} = 1.4$ and $n_{\mathrm{H}} = 3.6$, for both TE- (right side) and TM-polarized light (left side). The incident medium light line (*i.e.*, $\omega = ck_y$) is plotted in red, above which extended modes exist in the incident medium (air in this example). Hence, we only consider the modes above the light line; otherwise propagation in the air is evanescent. Colored regions are areas where electromagnetic modes are supported, while in white areas there are no electromagnetic modes. The first omnidirectional region is shaded in yellow with points U and L representing the upper and lower frequency limits, respectively. The width of this region is proportional to the index contrast of layers, *i.e.*, $(n_{\mathrm{H}} - n_{\mathrm{L}})$. In the p-polarized section, there exists a point at which the lowest two bands cross. This point corresponds to the Brewster's angle $\theta_{\mathrm{B}} = \tan^{-1}(n_{\mathrm{H}}/n_{\mathrm{L}})$ at which the reflection of TM-mode light vanishes. The second criterion for omnidirectional reflectance, mentioned above, is to preclude the existence of this crossing

above the light line. Thus, by appropriate selection of n_L, the Brewster's angle becomes inaccessible by plane waves in the incident medium, enabling an omnidirectional band for both polarizations. Figure 2.2 demonstrates the ratio of omnidirectional bandwidth over the center wavelength (*i.e.*, λ_B) versus the refractive index contrasts for a QWS starting with a high index layer. The horizontal axis represents n_L/n_0, while the vertical axis depicts n_H/n_L (the labels have the same meaning despite different convention for representation). The shaded zone in the figure is the area at which a non-zero omnidirectional band exists. An example of a multilayer based on Si/SiO_2 in air is also indicated in the shaded area. Even though achieving omnidirectional reflection by means of dielectric multilayers is plausible in theory, practical realization of a truly broadband omnidirectional mirror is difficult, especially in the visible range.

2.3 Fabry-Perot cavities (FPCs)

All optical cavities (optical resonators) 'trap' light at one or more resonant frequencies, in the form of standing waves confined by reflective boundaries [4]. The FPC is the archetypal, and arguably also the most important type of optical resonator. As described below, FP resonators can be categorized into two groups: planar-mirror and curved-mirror FPCs.

2.3.1 Planar-mirror FPCs

In its most basic form (see Fig. 2.3(a)), a FPC consists of two plane mirrors M_1 and M_2, with reflectance R_1 and R_2, respectively, separated by a medium with refractive index of n and length L. For an 'empty' cavity (*i.e.*, with a non-solid cavity medium), the cavity length can be adjusted (*i.e.*, tuned) by moving one or both mirrors. The resonant condition for the FPC is essentially as follows: the round-trip phase shift for light bouncing back and forth between the mirrors must be a multiple of 2π, in order that the infinite set of partial reflections interferes constructively. For the planar-mirror FPC (Fig. 2.3(a)), if we assume that the mirrors have infinite extent in the directions parallel to the medium boundaries, then the problem can be analyzed using plane waves. For the applications discussed here, we shall restrict our attention to normally incident light. Furthermore, the discussion that follows assumes a symmetric cavity ($R_1 = R_2 = R$) and 'hard-mirror' boundary conditions.

In other words, the phase change on reflection, which results in an effective increase in the cavity length for real mirrors [92], is initially neglected.

If light in the form of a plane wave is normally incident onto the planar-mirror cavity, it undergoes multiple partial reflections, leading to numerous transmitted and reflected field components. Light traveling a single round trip is subject to a propagation phase shift given by:

$$2\phi = \frac{4\pi}{\lambda_0} nL, \tag{2.4}$$

where λ_0 is wavelength of light in vacuum and ϕ is single-pass phase shift. The overall (net) transmission can be obtained by a summation over the infinite set of transmitted sub-components, and is expressed:

$$\frac{I_t}{I_i} = \frac{1}{1 + K_{\mathrm{F}} \sin^2(\phi)}, \tag{2.5}$$

where I_i and I_t are, respectively, the total incident and transmitted intensity, R is the reflectance of the mirrors, and K_{F} is the 'coefficient of finesse' and is defined as:

$$K_{\mathrm{F}} \equiv \frac{4R}{(1-R)^2}, \tag{2.6}$$

From Eq. 2.5, one can readily find that unity transmission is predicted whenever $\phi = 2m\pi$, where m is an integer representing the *longitudinal* mode order. Incorporating this condition into Eq. 2.4 results in the condition for a resonance frequency:

$$\nu_m = m\frac{c}{2nL}, \tag{2.7}$$

Accordingly, the allowed modal resonance wavelengths can be written as:

$$\lambda_m = \frac{2nL}{m}. \tag{2.8}$$

Another important factor of a FPC is 'Free Spectral Range' (FSR), which is defined as the frequency difference between two consecutive resonance frequencies of mode order m and $m+1$ (see Fig. 2.3(b)) and can be simply found from Eq. 2.7 [93]:

$$\nu_{\mathrm{f}} = \frac{c}{2nL}. \tag{2.9}$$

FSR indeed represents the frequency range over which a FPC can be tuned. Neglecting material dispersion and mirror penetration effects, FSR is a constant factor over the entire

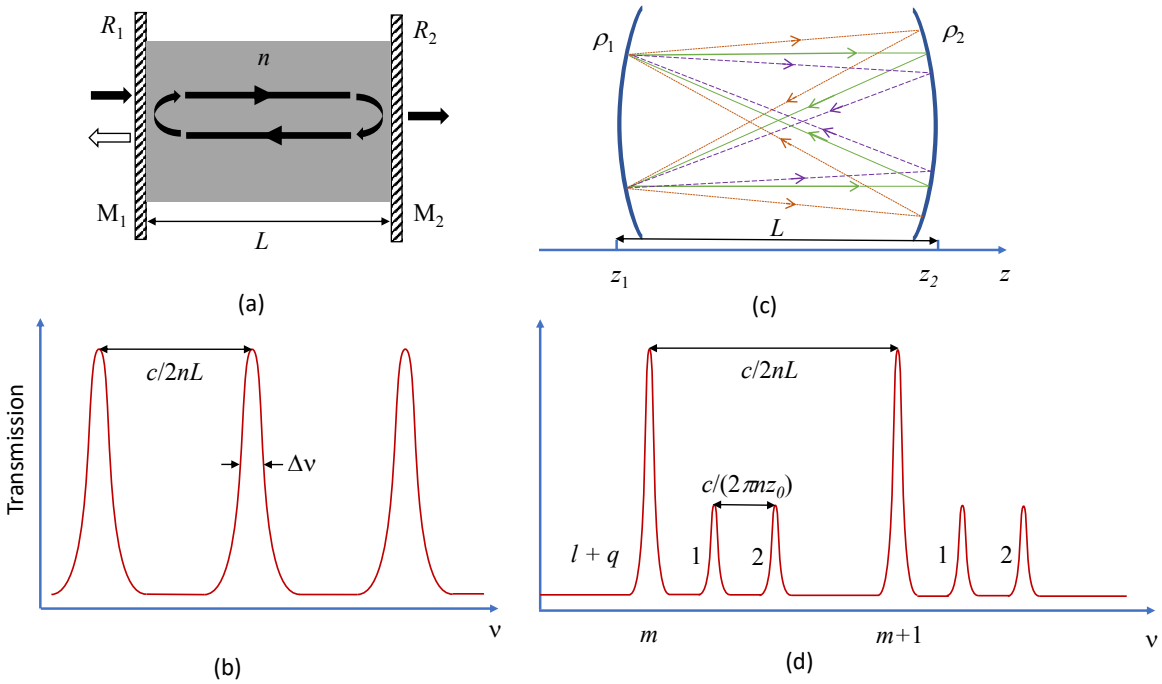

Figure 2.3: (a) Schematic of a Fabry-Perot resonator consisting of parallel mirrors M_1 and M_2 with reflectances of R_1 and R_2, respectively, surrounding a cavity medium of refractive index n and thickness L. Light introduced from one side undergoes multiple reflections, leading to partial transmission from the other side. (b) Typical transmission of a planar FPC depicting frequency spacing (*i.e.*, the FSR) of adjacent longitudinal modes and the full-width at half-maximum ($\Delta\nu$) of an individual modal peak. (c) Schematic representation of a curved-mirror FPC with length L, where mirrors with radii of curvature ρ_1 and ρ_2 are placed at z_1 and z_2, respectively. (d) Typical transmission spectrum of a curved-mirror FPC as a function of mode numbers l, q, and m, where $\rho_1, \rho_2 \gg L$ is assumed.

frequency range; however, in terms of wavelength, FSR is inversely proportional to the mode order:

$$\lambda_{\mathrm{f}} = \frac{\lambda_m}{(m+1)}. \tag{2.10}$$

There exist two FOMs to quantify the frequency selectivity of an optical resonator; quality factor (Q) and finesse ($\mathcal{F}$). The Q-factor is often used for electrical resonance circuits and microwave resonators, and is universally defined as:

$$Q \equiv 2\pi \left(\frac{\text{stored energy}}{\text{energy loss per cycle}} \right). \tag{2.11}$$

For sufficiently high values, Q is conveniently expressed in terms of the resonance frequency and the full-width-at-half-maximum or FWHM ($\Delta\nu$) of the resonator line-shape:

$$Q = \frac{\nu_m}{\Delta\nu}. \tag{2.12}$$

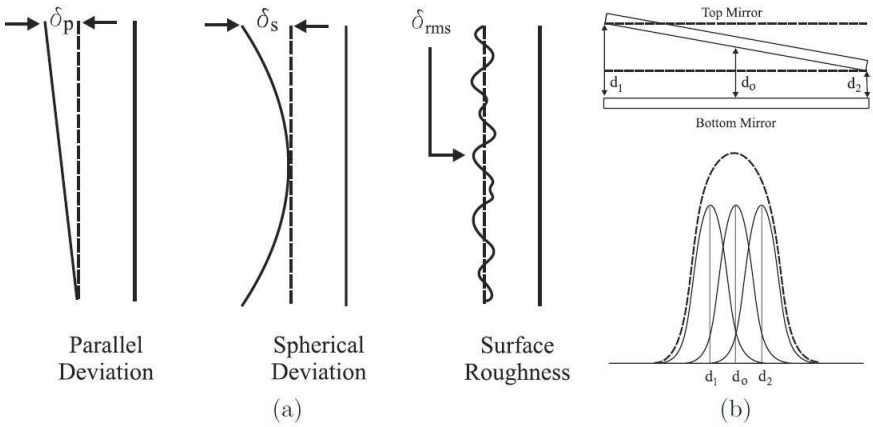

Figure 2.4: (a) Different types of defect in mirrors of a FPC. (b) The effect of non-parallelism of mirrors on the effective finesse of a FPC (adapted from [94]).

The reflection finesse ($\mathcal{F}_{\mathrm{R}}$) is defined as:

$$\mathcal{F}_{\mathrm{R}} \equiv \frac{2\pi}{\gamma}, \tag{2.13}$$

where 2π is fringe spacing and γ is the FWHM of the fringes in terms of ϕ. Assuming reflectance of $R \lesssim 1$, the reflection finesse can be worked out from Eq. 2.5 and is given by:

$$\mathcal{F}_{\mathrm{R}} = \pi\sqrt{R}/(1-R). \tag{2.14}$$

It can be also shown that:

$$\mathcal{F}_{\mathrm{R}} = \frac{\nu_{\mathrm{f}}}{\Delta\nu}. \tag{2.15}$$

Combining Eqs. 2.15 and 2.12, one can readily verify that $Q = m\mathcal{F}_{\mathrm{R}}$. The physical interpretation of finesse is that it represents the average number of round-trips made by a resonant photon before it leaves the cavity.

It should be noted that the effective finesse usually differs from the reflection finesse given in Eq. 2.14 due to defects in the mirrors. The so-called defect finesse can be sub-categorized into three groups (see Fig. 2.4): (i) parallelism defects ($\mathcal{F}_p$), (ii) spherical deviations ($\mathcal{F}_{\mathrm{s}}$), and (iii) surface irregularities ($\mathcal{F}_{\mathrm{rms}}$) which are given by [3]:

$$\mathcal{F}_{\mathrm{p}} = \frac{\lambda}{\sqrt{3}\delta_{\mathrm{p}}}, \tag{2.16}$$

$$\mathcal{F}_{\mathrm{s}} = \frac{\lambda}{2\delta_{\mathrm{s}}}, \tag{2.17}$$

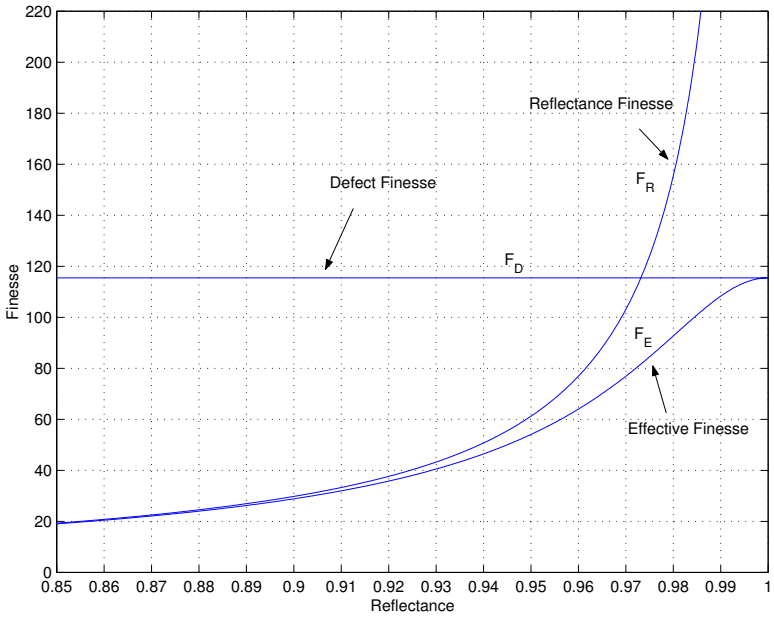

Figure 2.5: A plot showing how effective finesse is limited to defect finesse, base on Eq. 2.20 (adapted from [94]).

$$\mathcal{F}_{\mathrm{rms}} = \frac{\lambda}{4.7\delta_{\mathrm{rms}}}, \tag{2.18}$$

where δ_{p} and δ_{s} are the parallel and spherical deviation from a planar reference, and δ_{rms} is the root-mean-square deviation of a Gaussian distribution of the surface roughness. Hence, the total defect finesse is expressed:

$$\mathcal{F}_{\mathrm{D}} = \left(\frac{1}{\mathcal{F}_{\mathrm{p}}^2} + \frac{1}{\mathcal{F}_{\mathrm{s}}^2} + \frac{1}{\mathcal{F}_{\mathrm{rms}}^2} \right)^{-1/2}. \tag{2.19}$$

As such, the overall effective finesse can be estimated as:

$$\mathcal{F}_{\mathrm{eff}} = \left(\frac{1}{\mathcal{F}_{\mathrm{D}}^2} + \frac{1}{\mathcal{F}_{\mathrm{R}}^2} \right)^{-1/2}. \tag{2.20}$$

Equation 2.20 suggests that the effective finesse asymptotically saturates to a point determined by defect finesse (see Fig. 2.5). For simplicity throughout this report, we drop the subscript from $\mathcal{F}_{\mathrm{eff}}$, and thus $\mathcal{F}$ stands for the effective finesse in the remainder of the thesis.

2.4 Curved-mirror Fabry-Perot cavities

As discussed, in planar-mirror FPCs, non-parallelism and uncontrolled curvature of the mirrors leads to degradation of Q and $\mathcal{F}$. These parameters can be further reduced by beam

walk-off arising from the non-plane-wave nature of a real beam [95]. To avoid excessive walk-off losses, the flat mirrors need to have transverse dimensions that are significantly larger than the input beam. FPCs constructed from curved mirrors can mitigate many of the aforementioned problems. In these cavities, light rays 'retrace themselves' as they travel back and forth between the mirrors, which means the mirrors effectively refocus the circulating light (see Fig. 2.3(c)) .

2.4.1 Gaussian beam modes

The modes of a curved-mirror resonator are the beam-like solutions of the paraxial Helmholtz equation with the boundary condition imposed by the mirrors [93]. Applying the paraxial approximation, the Helmholtz equation is reduced to [96]:

$$\frac{\partial^2\psi}{\partial x^2} + \frac{\partial^2\psi}{\partial y^2} - 2k\frac{\partial\psi}{\partial z} = 0, \tag{2.21}$$

where $\psi(x, y, z)$ is a complex scalar wave amplitude for the transverse wave profile. The term $\partial^2\psi/\partial z^2$ is not present in Eq. 2.21 due to the paraxial approximation, in which it is assumed that rays diverge with small angle (*i.e.*, $\theta \ll 1$ rad) through the optical system.

A Gaussian beam is a beam with circular symmetry around the propagation axis and with energy confined near the axis. The wave front of the beam is a group of paraxial rays with small divergence angle (see Fig. 2.6). The intensity of a Gaussian beam is given by:

$$I = I_0 \left(\frac{w_0}{w_z}\right) \exp\left[\frac{-2(x^2+y^2)}{w^(z)}\right], \tag{2.22}$$

where w_0 is the beam waist radius, and $w(z)$ is the beam spot size given by:

$$w(z) = w_0 \left[1 + \left(\frac{z}{z_0}\right)^2\right]^{1/2}, \tag{2.23}$$

where $z_0 = \pi n w_0^2/\lambda_0$ is known as 'Rayleigh range', which is the distance from waist to the point where the beam area has doubled. The radius of curvature (RoC) of a Gaussian beam wavefront is given by:

$$\rho(z) = z + \frac{z_0^2}{z}. \tag{2.24}$$

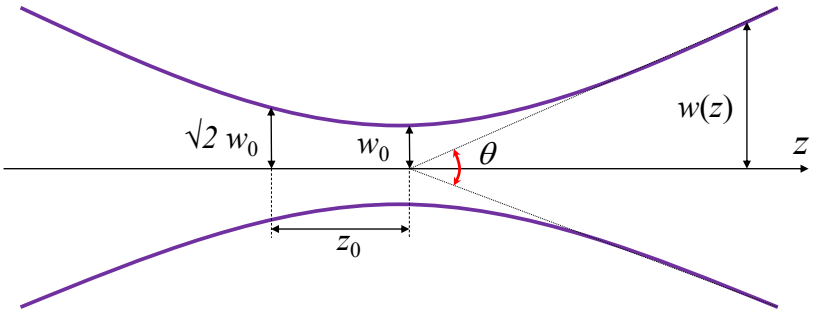

Figure 2.6: A schematic showing a Gaussian beam width $w(z)$ along the propagation axis z. w_0 is the minimum spot size, θ is the beam divergence angle, and z_0 is the distance between minimum spot to a point where beam area is doubled.

It should be noted that circulation of a Gaussian beam inside a spherical-mirror resonator only occurs if the wavefronts of the beam match the mirrors' RoC. This way, the beam satisfies Helmholtz equation and the boundary conditions at the mirrors.

Solution of Eq. 2.21 for a cavity with rectangular symmetry leads to higher order modes adjacent to each longitudinal mode calculated from Eq. 2.7. These modes are called Hermite-Gaussian modes whose transverse field distribution is given by [6]:

$$\begin{aligned} E_{l,q}(x,y,z) =& E_0 \frac{w_0}{w(z)} H_l\left(\sqrt{2}\frac{x}{w(z)}\right) H_q\left(\sqrt{2}\frac{y}{w(z)}\right) \\ & \times \exp\left[-\frac{x^2+y^2}{w^2(z)} - ik\frac{x^2+y^2}{2\rho(z)} - ikz + i(l+q+1)\zeta(z)\right], \end{aligned} \tag{2.25}$$

where H_l and H_q are the Hermite polynomials of orders l and q, respectively, and $\zeta(z)$ is the 'on-axis longitudinal phase delay' known as the 'Gouy phase' of the beam and is given by [93]:

$$\zeta(z) = \tan^{-1}(z/z_0) = \tan^{-1}\left(\frac{\lambda_0 z}{\pi w_0^2 n}\right). \tag{2.26}$$

The intensity profile of some low order Hermite-Gaussian modes are shown in Fig. 2.7(a).

An alternative solution to the paraxial wave equation can be found in cylindrical coordinates. These family of solutions are known as 'Laguerre-Gaussian' modes and are given by [6]:

$$\begin{aligned} E_{p,q}(r,\phi,z) =& E_0 \frac{w_0}{w(z)} \left(\frac{\sqrt{2}r}{\omega(z)}\right)^{|q|} L_p^{|q|}\left(\frac{2r^2}{\omega^2(z)}\right) \\ & \times \exp\left[-\frac{r^2}{\omega^2(z)} - ik\frac{r^2}{2\rho(z)} - ikz + iq\phi + i(2p+|q|+1)\zeta(z)\right], \end{aligned} \tag{2.27}$$

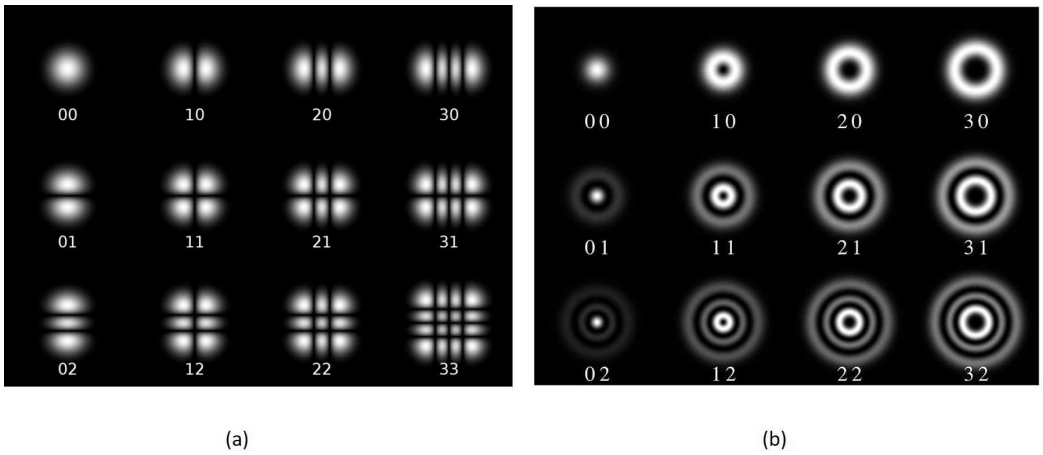

Figure 2.7: Intensity profiles of the first twelve (a) Hermite-Gaussian and (b) Laguerre-Gaussian modes (adapted from [97]).

where L_p^q are the Laguerre polynomial of order (p, q), p and q are *radial* and *azimuthal* mode orders and ϕ is the azimuthal angle in a cylindrical coordinate system (r, ϕ, z). The intensity profile of some low order Laguerre-Gaussian modes are shown in Fig. 2.7(b).

2.4.2 Mode stability

In an unstable condition, the beam size in the cavity grows with repeated reflections and ultimately gets larger than the size of the cavity mirrors, so that power is not confined for a significant period of time. The general stability criterion for spherical-mirror resonators is calculated utilizing ray transfer matrix analysis and is given by [93]:

$$0 \leq g_1 g_2 \leq 1 \tag{2.28}$$

where $g_1 = 1 - L/\rho_1$ and $g_2 = 1 - L/\rho_2$.

Amongst several types of cavities with curved mirrors, hemispherical (known as half-symmetric) cavities, constructed using one flat and one curved mirror, have attracted significant interest for MEMS-based Fabry-Perot cavities and practical applications. In order to find the stability criterion for this type of cavity, assume $\rho_1 = \rho$ and $\rho_2 = \infty$; then, Eq. 2.28 is simplified to:

$$\rho \geq L. \tag{2.29}$$

The half-symmetric resonator is of primary importance to this research, as discussed below. Equation 2.29 is satisfied for all of the buckled-dome microcavities studied in this thesis, and stable cavity modes have been verified.

2.4.3 Mode volume

Mode volume (V_{M}) is another factor which is of significant importance in FPCs and is defined as [98]

$$V_{\mathrm{M}} = \frac{\iiint_V \epsilon |E(x,y,z)|^2 dx\, dy\, dz}{E_0^2}, \tag{2.30}$$

where E_0 is the peak value of the electric field in the cavity. The mode volume for a standing-wave associated with the TEM_{00} mode is approximately given by [12]:

$$V_{\mathrm{M}} \approx \frac{\pi}{4} w_0^2 L, \tag{2.31}$$

where w_0 can be estimated as [12]:

$$w_0 = \sqrt{\frac{\lambda}{\pi}} \left(L \frac{\rho_1 \rho_2}{\rho_1 + \rho_2} \right)^{1/4}, \tag{2.32}$$

For the case of plano-concave or half-symmetric cavities where ρ_2 is infinite and thus $|\rho_1| \ll |\rho_2|$ (as in the case of Refs. [15, 16, 52, 82, 99]), the beam waist lies at the planar mirror and is given by the expression:

$$w_0 = \sqrt{\frac{\lambda}{\pi}} \left(L.\rho_1 \right)^{1/4}, \tag{2.33}$$

It is worth noting that Q and V_{M} essentially quantify the degree of temporal and spatial confinement, respectively, of the field by the cavity [67].

2.4.4 Resonance frequencies

For stable modes, the wavefront curvature at the positions of the mirrors matches the radii of curvature of the mirrors. Applying the phase condition to the Hermite-Gaussian beam yields the resonance frequencies as follows [93]:

$$\nu_{l,q,m} = m\nu_{\mathrm{f}} + (l + q + 1) \frac{\Delta\zeta}{\pi} \nu_{\mathrm{f}}, \tag{2.34}$$

where $\Delta\zeta = \zeta(z_2) - \zeta(z_1)$, and z_1 and z_2 are positions of mirrors M_1 and M_2 , respectively. Equation 2.34 indicates that the longitudinal modal spacing is independent of the mirror

curvatures, and is the same as that for the planar mirror Fabry-Perot. The second term in Eq. 2.34 represents a shift in all resonance frequencies, and is dependent on mirror curvatures.

It is useful to know the frequency spacing between transverse modes. To this end, we restrict ourselves to short cavities in which $L \ll |\rho_1|, |\rho_2|$. The frequency spacing for this specific case is given by [6]:

$$\Delta\nu \approx \frac{c}{2\pi n z_0}\Delta(l+q). \tag{2.35}$$

Figure 2.3(d) illustrates this spacing for two adjacent transverse modes.

2.5 Hollow core waveguides

A waveguide is basically a FPC which is open along the propagation direction (see Fig. 2.8). For a waveguide to support a mode, the following self-consistency condition must be satisfied [100]:

$$r_{\mathrm{T}} r_{\mathrm{B}} \exp(-j2k_y d) = 1, \tag{2.36}$$

where k_y is the transverse propagation constant, and r_{T} and r_{B} are the field reflection amplitude of the top and the bottom mirrors, respectively (see Fig. 2.8), and are given by:

$$r_{\mathrm{T}} = |r_{\mathrm{T}}| \exp(j\Phi_{\mathrm{T}}), \tag{2.37}$$

$$r_{\mathrm{B}} = |r_{\mathrm{B}}| \exp(j\Phi_{\mathrm{B}}), \tag{2.38}$$

in which Φ_{T} and Φ_{B} are phase shift on reflection from top and bottom mirrors. Assuming perfectly reflecting mirrors, and hard boundary conditions (*i.e.*, no penetration into mirrors), Eq. 2.36 is simplified to:

$$2k_{ym}d - \Phi_{\mathrm{T}} - \Phi_{\mathrm{B}} = 2m\pi. \tag{2.39}$$

where m is an integer representing the mode order. This can be simplified further by the assumption of metallic mirrors where $\Phi_{\mathrm{T}} = \Phi_{\mathrm{B}} = \pi$:

$$k_{ym}d = m\pi. \tag{2.40}$$

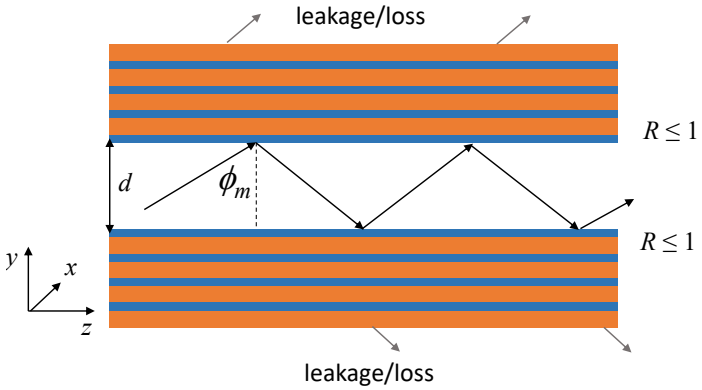

Figure 2.8: Conceptual schematic of slab model of a hollow core waveguide with Bragg mirror cladding and height d. ϕ_m indicates the bouncing angle for mode m. The finite number of multilayer results in reflection less than unity and in turn leakage of propagating light. The gray arrows at the outer side of mirrors indicate leakage.

Therefore the 'propagation constant' along the z axis can be easily worked out through its trigonometric relation with other wavevectors and is given by [101]:

$$\beta_m = k_0 \sin\phi_m = \left(\frac{2\pi}{\lambda}\right) \sin\phi_m. \tag{2.41}$$

where k_0 is free-space propagation constant.

It is worthwhile noting that the above-derived propagation constant is solely applicable to lossless waveguides with hard boundary condition. Theoretically, perfect reflection occurs by (i) total internal reflection (TIR) – not pertinent to hollow waveguides, (ii) perfectly conducting mirrors, and (iii) lossless photonic crystals with infinite number of periods. Unfortunately, non of the aforementioned circumstances exist in reality, and the assumption of perfectly reflecting mirrors is only a theoretical abstraction. Therefore, while light is propagating along a hollow core waveguide, its power decays due to absorption loss and/or radiation through imperfect mirrors. Since, on-chip hollow core Bragg waveguides, fabricated by buckling self-assembly technique, presented in this thesis (see Chapter 6), are also considered as leaky/lossy waveguides, it would be advantageous to succinctly go through some theoretical treatments on leaky/lossy waveguides.

Figure 2.8 illustrates a planar leaky waveguide with finite-period Bragg mirrors, where the leakage due to non-unity reflectance of mirrors is shown by gray arrows at the outer side of the mirrors. In such a waveguide, both k_y and k_z are complex, and in turn a self-consistency condition must be satisfied for both phase and amplitude of the field using Eq.

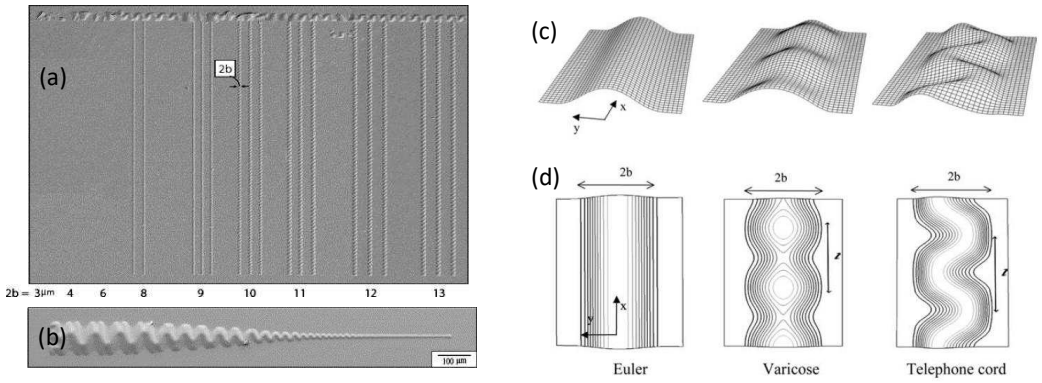

Figure 2.9: (a) Buckle delamination along patterned strips of low adhesion, representing telephone cord and Euler morphologies . (b) Propagation of delamination along a tapered strip of low adhesion, showing telephone cord morphology at wider sections, and Euler shape in narrow parts . (c) and (d) schematics of various buckling phenomena that occur along strips clamped at $y = \pm b$. Adapted from [103].

2.36. This leads to a 'complex' modal propagation constant:

$$k_z = \sqrt{k_0^2 - k_y^2} = \beta_{\mathrm{C}} = \beta_m - j\frac{\alpha_m}{2}, \tag{2.42}$$

where α_m is the 'modal intensity attenuation coefficient' which is associated with non-unity reflecting mirrors. In a slab structure, the attenuation factor can be estimated using a Ray-optics model [102]:

$$\alpha_m \approx \frac{-\ln\left(R_{\mathrm{T}} R_{\mathrm{B}}\right)}{2 d_{\mathrm{eff}} \tan\phi_m}, \tag{2.43}$$

where R_{T} and R_{B} are reflectance of the top and the bottom mirrors, respectively, and d_{eff} is the effective thickness of the waveguide, accounting for the penetration depth into both mirrors.

2.6 Buckling delamination of thin films

Since this research work is devoted solely to devices fabricated by a buckling self-assembly process, knowledge about the theory of buckling delamination could provide useful context. Buckling delamination is a phenomenon in which a deposited thin film delaminates from its substrate due to its biaxial compressive stress. Buckling delamination is traditionally viewed as a failure mechanism in compressed films [103]. However, by intentionally patterning regions of low adhesion between the film and substrate, interesting optical and MEMS-like devices can be fabricated [16, 82, 83, 104].

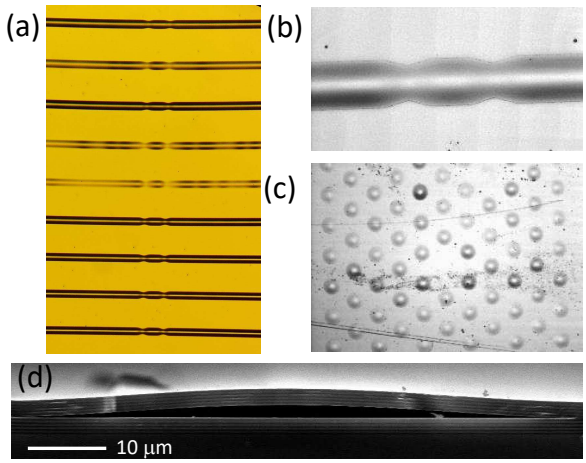

Figure 2.10: Microscope image of (a) array of cascaded dual-taper cavities with length 100 µm, (b) a dual-taper cavity with length 50 µm, and (c) array of buckled-dome microcavities with diameter 50 µm. (d) SEM image of a cleaved buckled waveguide facet.

The morphology of a buckled feature depends on several factors, such as film thickness and stress, and the pattern of the low-adhesion areas. In strip patterns, once delamination is nucleated, it propagates along the strip if the width of the strip ($2b$) is greater than a critical width ($2b_0$) which is described further below. This delamination primarily propagates through the film in two different shapes; (i) straight-sided buckles (known as 'Euler' buckles) and (ii) 'telephone cord' buckles, the latter of which is more prevalent (see Figs. 2.9). Nonetheless, by controlling the aforementioned parameters, design of low-adhesion areas gives rise to the formation of hollow waveguides on chips (see Fig. 2.10(a) and 2.10(b)) [83]. In contrast, placing circular low-adhesion patterns under the film which is subject to delamination can result in dome-shaped cavity formation (see Fig. 2.10(c)) [15, 16, 82].

2.6.1 Thin strips

To model the behavior of buckling of a film under equi-biaxial compressive stress and to find the corresponding critical stress (σ_c), and buckling amplitude (Δ), it is assumed that the film is fully clamped along its edge (see Fig. 2.9(c) and 2.9(d)). This assumption is valid only if the Young's modulus of the substrate is greater than one fifth of that of the buckled plate [103].

Buckling delamination can occur along a narrow strip provided the stress of the film is

greater than the critical stress which is given by [103]:

$$\sigma_c = \frac{\pi^2}{12}\frac{E}{1-\nu^2}\left(\frac{h}{b}\right)^2, \tag{2.44}$$

where E is the Young's modulus, ν is the Poisson's ratio of the film, and h is the film thickness. As such, the normal displacement of the buckled feature is given by [103]:

$$\Delta = \frac{\xi h}{2}\left(1+\cos\left(\frac{\pi y}{b}\right)\right), \tag{2.45}$$

where ξ is a dimensionless factor determined by the ratio of the initial pre-buckled film stress (σ) to the critical stress and is expressed [103]:

$$\xi \equiv \left(\frac{\Delta_{max}}{h}\right) = \sqrt{\frac{4}{3}\left(\frac{\sigma}{\sigma_c}-1\right)}. \tag{2.46}$$

In this report, the peak height of the buckled waveguides and microcavities are shown as δ; thus, Eq. 2.46 can be re-written as follows:

$$\delta = \Delta_{max} = h\sqrt{\frac{4}{3}\left(\frac{\sigma}{\sigma_c}-1\right)}. \tag{2.47}$$

It is straightforward to find the minimum half-width a_0 associated with the onset of buckling for a given film stress of σ. Substituting $\sigma_c = \sigma$ into Eq. 2.44 gives:

$$a_0 = \frac{\pi h}{2\sqrt{3}}\sqrt{\frac{E}{(1-\nu^2)\sigma}}. \tag{2.48}$$

As a result

$$\frac{\sigma}{\sigma_c} = \left(\frac{b}{b_0}\right)^2. \tag{2.49}$$

This implies that the ratio of σ/σ_c is proportional to the ratio of the strip width over the minimum width.

In the context of straight-sided buckling delamination, it is useful to estimate the energy release rate while delamination is propagating along a thin strip. Consider an infinitely long low-adhesion thin strip which is subject to equi-biaxial compressive stress, and clamped along its edges. Now, assume that the delamination has been nucleated at one end of the strip and propagated long enough (with Euler mode) such that the length of the buckled section is several times the strip width, satisfying the steady-state condition for energy release per unit area. In this case the average energy release rate $\bar{G}$ is estimated by [103]

$$\bar{G} = U_0 - \bar{U}, \tag{2.50}$$

where U_0 is the energy release per unit area in the unbuckled regions and is given by [103]

$$U_0 = \frac{(1-\nu)\sigma^2 h}{E}, \tag{2.51}$$

while $\bar{U}$ is the average energy per unit area in the buckled regions and is given by [103]

$$\bar{U} = U_0 \left[1 + \left(\frac{1+\nu}{2}\right)\left(1 - \frac{\sigma_c}{\sigma}\right)^2\right]. \tag{2.52}$$

Thus, Eq. 2.50 can be written as

$$\bar{G} = G_0 \left(1 - \frac{\sigma_c}{\sigma}\right)^2, \tag{2.53}$$

where G_0 is the stored energy per area which is subject to release once a film buckles, and can be expressed

$$G_0 = \frac{1+\nu}{2} U_0 = \frac{(1-\nu^2)\sigma^2 h}{2E}. \tag{2.54}$$

It is worth noting that, Eq. 2.53 for the Euler mode is valid for $\sigma/\sigma_c < 6.5$ or $b/b_0 < 2.5$ [103]. Beyond that, delamination buckle transfers to varicose or more commonly to telephone cord modes (see Fig. 2.9).

Another important parameter for thin film buckling is the 'toughness' (Γ_t) of the interface between the compressively stressed plate and the low-adhesion layer, indicating the 'practical work of adhesion'. Propagation along a straight-sided strip continues if $\bar{G} > \Gamma_t$. The interface toughness is given by [105]:

$$\Gamma_t \approx W_A + U_f + U_s + U_{fric}, \tag{2.55}$$

where U_f and U_s are the energy release due to plastic deformation of the film and the substrate, respectively, U_{fric} is the energy release due to friction, and W_A is called 'the true work of adhesion' which is the amount of energy required to separate two bonded surfaces and is given by [105]:

$$W_A = \gamma_f + \gamma_s - \gamma_{fs}, \tag{2.56}$$

where γ_f and γ_s are the surface energy of the film and the substrate, respectively, and γ_{fs} is the energy of the interface of the film and the substrate.

2.6.2 Circular patterns

For the case of a circular plate with clamped boundary conditions, the critical stress is given by [106]

$$\sigma_{\mathrm{c}} = 1.2235 \frac{E}{1-\nu^2} \left(\frac{h}{a}\right)^2, \tag{2.57}$$

where a is the radius of circular buckle. The profile of a circular buckled film is well approximated as a shallow spherical shell. Nonetheless, the practical shape is mainly determined by elastic buckling mechanics which can be impacted by other factors such as plastic deformation and relaxation of compressive stress over time. Assuming purely elastic deformation and perfectly clamped boundary conditions, the buckling profile for a circular delamination buckle is given by [106]:

$$\Delta(r) \approx \delta[0.2871 + 0.7129 J_0(\mu r)], \tag{2.58}$$

where Δ is the vertical deflection, r is the radial coordinate (normalized to a), δ is the peak height of the buckle, J_0 is the Bessel function of first kind and order zero, and $\mu = 3.8317$ is the first zero of the Bessel function of the first kind and order one.

The energy release rate is given by [106]

$$\frac{G}{G_0} = c_2 \left[1 - \left(\frac{\sigma_{\mathrm{c}}}{\sigma}\right)^2\right], \tag{2.59}$$

where $c_2 = 1 + 0.902(1-\nu)$ and G_0 is the stored energy per unit area in the unbuckled film which is subject to release under plane strain conditions, given by [106]

$$G_0 = (1-\nu) h \sigma^2 / E. \tag{2.60}$$

It should be noted that, circular buckling also occurs if the energy release rate exceeds the interface toughness, *i.e.*, $G > \Gamma_{\mathrm{t}}$.

2.7 Fabrication

This section describes the general procedures used to fabricate devices by buckling self-assembly, including straight and axially varying waveguides and dome-shaped microcavities. The fabrication process is divided primarily into three phases: (i) deposition of Bragg mirrors, (ii) patterning and deposition of low-adhesion layers (LALs), and (iii) inducing loss

of adhesion in LALs. The fabrication steps are depicted in Fig. 2.11 and described below. Note that specific data such as film stresses and refractive indices are subject to change from time to time due to the change in targets, variations in the conditions of a multi-user sputtering chamber, and many other uncontrolled factors. Therefore, information given in these respects are associated with the devices presented in Chapters 3 and 6, which were made around the same time with minimal variations between film characteristics.

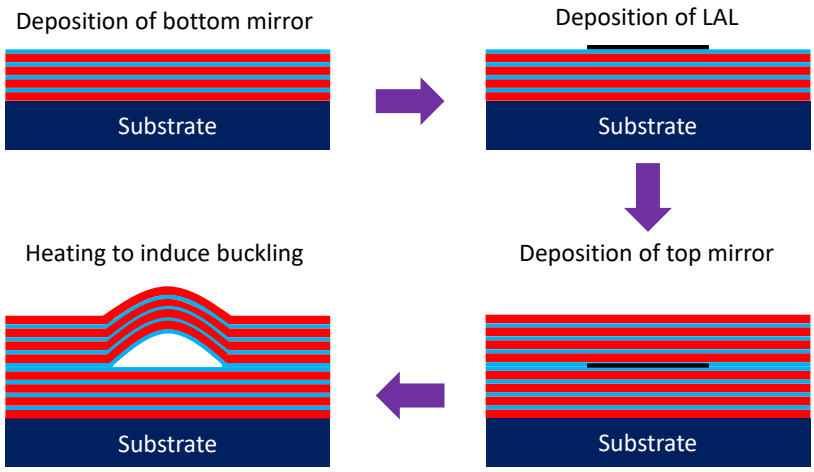

Figure 2.11: Schematic diagram of fabrication steps pertaining to controlled formation of delamination buckles.

To begin with, a 5-period a-Si/SiO_2 multilayer (starting with SiO_2) was deposited onto a piranha cleaned silicon wafer via reactive magnetron sputtering. For the case of buckled domes, a double-side-polished silicon wafer was chosen to facilitate optical detection in transmission scans. In all depositions, the process chamber was pumped down over night to a base pressure of $< 10^{-6}$ Torr, substrate temperatures were set to 150°C, and Ar flow rate was fixed at 50 SCCM. Identical targets of 99.999 % pure n-type Si were used for both a-Si and SiO_2 depositions. Other deposition parameters are summarized in Table 2.1. For the case of buckled-dome microcavities, slightly lower power was used for SiO_2 depositions, aiming to attain lower-loss layers. Variable-angle spectroscopic ellipsometry (VASE) verified that these parameters resulted in films with refractive index of ∼3.7 and ∼1.46, and extinction coefficient of $< 8 \times 10^{-4}$ and $< 1 \times 10^{-5}$ for a-Si and SiO_2, respectively, at 1550 nm wavelength. Bragg mirror layers were designed to be quarter-wave layers centered at 1550 nm. Figure 2.12 shows the reflectance characteristics of a 5-period sputter-deposited

Table 2.1: Sputtering parameters

	Power (W)	**Frequency (kHz)**	**Duty cycle (%)**	**Oxygen flow (SCCM)**	**Deposition pressure (mTorr)**
a-Si	200	150	92.5	NA	3
SiO_2	200/175	150	88	3.2	4

a-Si/SiO_2 mirror measured by VASE ellipsometer at 20° and estimated by transfer matrix simulation for s-polarized light at 20° and 88° incident angles. The reflectance around 1700 nm is slightly greater than one which can be attributed to the low input-power signal at the edge of VASE operating wavelength range and the artifacts due to noise floor. In spite of this, the plot depicts good agreement with transfer-metrix simulations and exhibits a broad omnidirectional reflectance over ∼1000 nm wavelength range, which is favorable for applications in axially varying hollow waveguides discussed in Chapter 6.

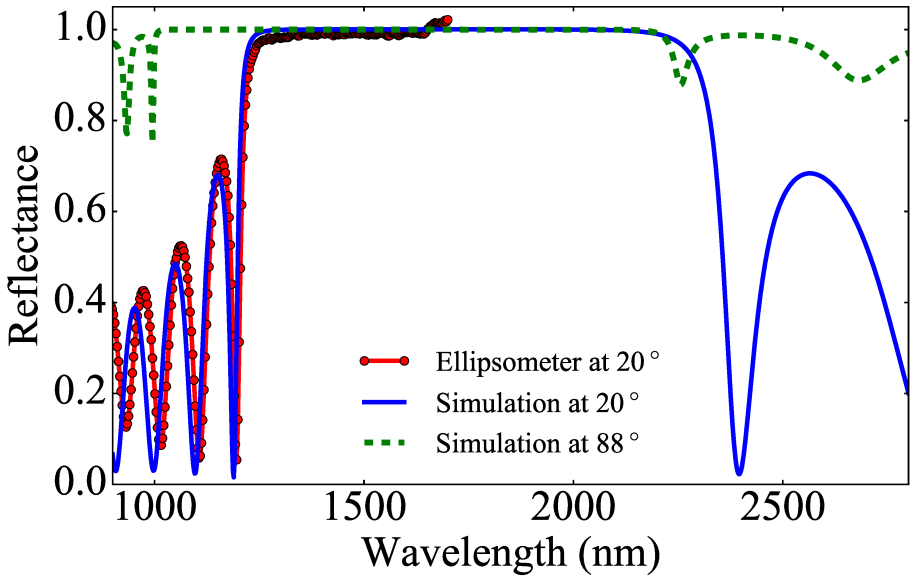

Figure 2.12: Predicted and experimentally determined reflectance characteristics of a sputtered 5-period a-Si/SiO_2 Bragg mirror. Results are for s-polarized light at 20° and 88° incident angles.

The crucial step after deposition of the first mirror is patterning and deposition of low-adhesion thin layers to constrain buckling delamination to straight/tapered strips or circular regions. Amongst various candidates for low-adhesion layer, such as silver and carbon, fluorocarbon (FC) offers many advantages. This material can be deposited with

characteristics similar to bulk Teflon. The films are transparent in a broad wavelength range of interest (*i.e.*, visible to infrared), enable low adhesion, are robust enough to survive the high temperature deposition circumstances of the top mirror, are not chemically reactant, and are amenable to being patterned using a standard optical lithography liftoff process. FCs have been used previously in our group for fabrication of a variety of devices for the infrared operating wavelength range [82, 83] and further optimizations were recently made for visible range devices [16, 107].

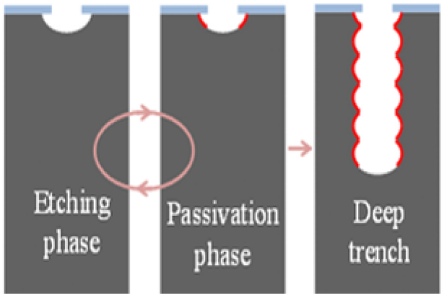

Figure 2.13: Schematic representation of the DRIE Bosch process. The etching and the passivation cycles alternate until a deep trench is created into a substrate (adapted from [108]).

In keeping with the standardized process in our group, these layers were deposited as part of a DRIE Bosch process by 'inductively coupled plasma reactive-ion etching' (ICPRIE) method using the 'Alcatel AMS110' machine, housed in the class 10 cleanroom of the nanoFAB at the University of Alberta. The Bosch process consists of two alternating cycles: passivation cycle and etching (or depassivation) cycle (see Fig. 2.13). The former is aimed at protecting the sidewalls during etching, while in the latter, ion bombardment of a gas (typically 'sulfur hexafluoride' (SF_2) for silicon etching) selectively removes the layers (typically 'octafluorocyclobutane' (C_4F_8)) deposited during the passivation cycle, mostly from the bottom of the trench. The process continues until a deep etched trench is made [108]. In order to adapt this passivation cycle for the deposition of the LAL, two main parameters needed to be modified: RF coil power, and deposition pressure. Further details about optimization of FC deposition using 'Alcatel AMS110' can be found in [109].

Using the parameters presented in Table 2.2, FC layers were deposited on a lithographically patterned bottom mirror, followed by a liftoff step with acetone sonication. Then, a

Table 2.2: Parameters related to 'Alcatel AMS110' used for FC films deposition.

Pressure (mTorr)	**C_4F_8 flow rate (SCCM)**	**Chuck temperature (°C)**	**Chuck bias (W)**	**Chuck position (mm)**	**Coil power (W)**
5	60	10	0	120	600

5.5-period a-Si/SiO_2 Bragg mirror (starting with a-Si) was deposited. The total thickness of the upper mirror were estimated to be ∼2 µm. Later on, the stress of the deposited mirror was measured by 'Flexus Wafer Stress Measurement System', indicating an effective compressive stress of ~ -240 MPa.

In the last step, the wafer was diced/cleaved into smaller pieces (typically a quarter wafer), and mounted on top of a hotplate set at ∼100 °C. Then, the temperature was ramped up rapidly to ∼400 °C. This leads to loss of adhesion in fluorocarbon layers, inducing the formation of buckled features. Examples of some buckled structures are depicted in Fig. 2.10. Heights of the features is proportional to the widths of LAL. More details about the shape of structures will be provided in subsequent chapters.

Chapter 3

Small-mode-volume, channel-connected Fabry-Perot microcavities on a chip[1]

A monolithic thin-film buckling process was used to fabricate arrays of high-finesse curved-mirror Fabry-Perot cavities on a silicon chip, with areal density $\sim 10^4$ per square centimeter. The microcavities exhibit high yield, good uniformity, and nearly reflectance-limited finesse $\sim 2 \times 10^3$. The cavity shape matches the predictions of elastic buckling theory, with maximum curvature at the center where the fundamental mode resides. We describe cavities with mode volume $< 1.5\lambda^3$ for the fundamental spatial resonance. We also describe cavities connected to air-core channels. Preliminary light-coupling results suggest that these structures have potential to enable the side-coupling of gases, liquids, and pump, probe or trapping beams.

3.1 Introduction

Cavity quantum electrodynamics (CQED) - the study of atomic emitters interacting with optical resonators - is amongst the most promising approaches for quantum information technologies [61]. Many important building blocks (*e.g.*, single-photon sources and logic gates) can be implemented using CQED systems operating in either the strong-coupling regime, with coherent exchange of quanta between a light emitter and a cavity field, or in the weak-coupling regime, but with a high Purcell factor so that photon emission is deterministic and controllable [4]. For both the strong-coupling and high Purcell-factor regimes, the key ingredients are a high Q factor, to minimize spurious photon loss, and a low

[1]This chapter has been submitted for publication.

mode volume (V_{M}), to maximize the atom-photon coupling rate [60]. Low V_{M} is particularly important for the Purcell enhancement of solid-state emitters, where the relatively broad emission linewidth typically limits the effective Q factor [46, 68]. Also important are an ability to locate emitters within the cavity mode field and a convenient method to tune the cavity into resonance with the atomic transition of interest.

These requirements have motivated diverse research on the fabrication of 'open access', micro-scale, curved-mirror Fabry-Perot cavities (FPCs) [13,14,70–72,110,111]. For the most part, this work has employed micro-machining processes such as CO_2 laser ablation [13,14], isotropic plasma etching [71,72], or focused ion beam (FIB) milling [111] to form atomically smooth curved surfaces with effective radii of curvature (RoC) in the ∼10-1000 µm range. Aside from being relatively expensive and time-consuming (especially for the serial FIB and CO_2-laser approaches), these techniques have other drawbacks. For example, laser-ablated mirrors have morphology (in particular, the relationship between feature depth and RoC) that is determined primarily by the Gaussian intensity profile of the laser beam [12], although recent work [80] has employed pre- or post-processing steps to mitigate this. Furthermore, the ablated surfaces are often elliptical, which can result in polarization mode splitting [110], and aspherical, which can lead to loss from coupling between transverse modes [78].

For all of these approaches, perhaps the most significant drawback is that they require serial processing steps and a non-monolithic cavity construction. It is challenging to deposit high-reflectance coatings onto small-RoC curved surfaces, since the thin films can be subject to thickness variations [70] and cracking [111]. Moreover, to construct the cavity, two mirrors (*e.g.*, on separate substrates or fiber end-facets) must be subsequently aligned and held with extreme precision, which can create challenges with respect to cavity stabilization and noise [14, 72]. Also, implementing a mirror spacing on the order of 1 µm or less, required for operation in a low V_{M} regime, while retaining open access (for atoms, *etc.*) to the cavity, is non-trivial to say the least. In short, tradeoffs between mirror curvature, mirror diameter (which impacts diffraction losses), and minimum cavity spacing are inherent to hybrid assembly approaches [46, 68, 80].

We have previously described half-symmetric cavities fabricated by guiding the forma-

tion of delamination buckles within a thin-film mirror stack [15, 16, 82]. This is a uniquely monolithic approach, involving only thin film deposition and patterning on a single wafer, and it results in arrays of self-aligned FPCs that support stable modes, and for which reflectance-limited finesse has been demonstrated [82]. However, the process presents challenges with respect to providing 'open-access' to the mode field volume, since the buckled dome cavities are inherently closed features.

Here, we report for the first time buckled dome cavities operating in the fundamental (longitudinal) mode regime, with thermally tunable cavity resonances exhibiting $Q > 10^3$ and mode volume as small as $\sim 1.3\,\lambda^3$ at 1550 nm wavelength. High-density arrays of these cavities show good uniformity, especially given the experimental nature of the process. We also describe cavities intersected by hollow waveguide channels; these cavities retain excellent optical properties while enabling side-access to the cavity volume for the introduction of gases, liquids or pump/probe beams.

3.2 Fabrication and cavity morphology

The fabrication process has been described elsewhere [82,83]; only a few essential details are summarized here. The process started with the sputtering deposition of a 5-period SiO_2/Si-based quarter-wave-stack (QWS) mirror, nominally centered at 1550 nm wavelength, onto a double-side-polished silicon wafer. Next, a fluorocarbon low-adhesion layer with thickness $\sim$25 nm was deposited and patterned using a liftoff technique. These features define the regions of subsequent delamination and buckle formation within the multilayer stack; straight-sided strips become hollow waveguides [83] and circular features become Fabry-Perot 'dome' microcavities [15, 16, 82]. After patterning of the fluorocarbon layer, a 5.5 period QWS mirror was deposited with a tailored amount ($\sim$250 MPa here) of compressive stress [83]. Finally, hollow cavities were formed by heating the sample to drive buckling delamination between the lower and upper QWS mirrors, over the regions defined by the patterned fluorocarbon layer.

The primary goals of the present study were two-fold: first, we aimed to fabricate dome cavities operating in a fundamental (longitudinal and transverse) optical mode regime, and second, we aimed to further optimize the fabrication of channel-connected domes [16]. Fig-

ure 3.1 shows images of representative features that were fabricated in parallel on a single wafer. A portion of an array of dome microcavities, each having nominal base diameter of 50 µm (*i.e.*, the diameter of the circular fluorocarbon feature), is shown in Fig. 3.1(a). For domes of this size, the buckling process produced a peak height (*i.e.*, peak mirror spacing) on the order of 750 nm, or roughly half the design center wavelength of the QWS mirrors, making them well-suited for studies of fundamental resonant modes. From optical profilometer (ZYGO[2]) scans of ∼100 cavities, the average peak height was estimated as ∼710 nm, with standard deviation ∼60 nm. A similar 50-µm-base-diameter dome, but symmetrically intersected by 4 waveguide channels, is shown in Fig. 3.1(b). For these domes, the modified boundary conditions resulted in a larger peak height on the order of ∼1 µm. Since this height produces resonances which lay outside the range of our tunable laser, optical studies were conducted on larger (100 µm base diameter) channel-connected domes, as discussed below. The larger domes were also connected to wider (and thus taller) channels, enabling the side-coupling of light into the cavities.

As discussed elsewhere [82], the buckled domes form half-symmetric FPCs with optical properties that are well predicted by paraxial Gaussian beam optics. The half-symmetric cavity design is commonly employed for hybrid-assembled FPC microcavities [12–14, 46, 68, 70–72, 78, 80, 110, 111], because it simplifies transverse alignment, allows emitters such as quantum dots to be embedded within the flat mirror, and can also result in improved coupling efficiency to fiber modes [112]. The shape of the curved mirror is, of course, highly dependent on the fabrication process, ranging from hemispherical [70,110] to Gaussian [12]. For Gaussian-like surface profiles, the absence of sharp corners at the edges is beneficial for subsequent deposition of thin film mirrors [111]. However, deviations from a spherical shape can result in undesirable mode coupling effects [78].

As shown in Fig. 3.1(c), and consistent with our previous results for larger domes [15], we found that the profile is well approximated by the predictions of elastic buckling theory. For

[2]ZYGO is a noncontact profilometer based on white-light interferometry. White light from a lamp is divided into two beams, one of which is reflected off an internal high-quality mirror while the other is reflected off the sample. The reflected light beams are subsequently re-combined and detected by a solid-state camera. The surface of the sample is determined by the fringes resulted from the interference of the two beams. The device is able to measure depths up to 150 µm with 0.1 nm resolution and 0.4 nm RMS repeatability. Lateral measurements are performed based on the pixel size from the field of view of the used objective lens.

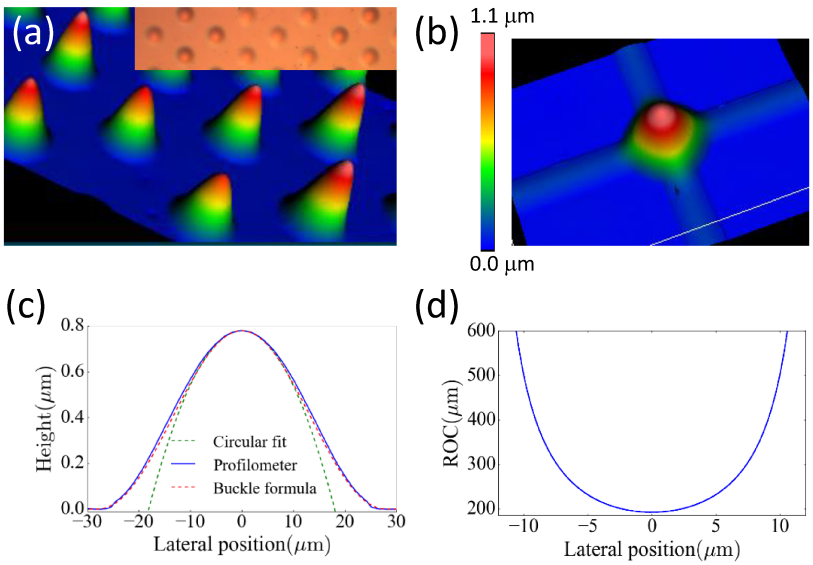

Figure 3.1: (a) Surface relief plot of an array of buckled dome cavities with 50 µm base diameter and peak height ∼750 nm. The inset shows a microscope image of a similar array. (b) Surface relief plot of a channel-connected dome; the dome has a base diameter of ∼50 µm and the channels are ∼20 µm wide. (c) Cross-sectional profile of a single dome as measured using an optical profilometer, along with a profile predicted by elastic buckling theory. A base diameter of 56 µm was assumed in the model. Also shown is a circle fit to the top portion of the experimental profile, revealing an effective RoC ∼200 µm. (d) Local RoC for the buckle profile from part c.

a circular delamination buckle, the profile can be expressed $\Delta(r) = \delta.[0.2871+0.7129.J_0(\mu r)]$ [106], where Δ is the vertical displacement, r is the radial coordinate (normalized to the base radius of the dome, a), δ is the peak height of the buckle, J_0 is the Bessel function of first kind and order zero, and $\mu = 3.8317$. In order to obtain a good fit to the experimental profile, we found it necessary to assume a base radius that is slightly larger than the nominal value associated with the fluorocarbon feature. We attribute this to the finite thickness of the fluorocarbon layer, which modifies the boundary conditions at the edge of the circular buckle. Note that a step-like offset of ∼25 nm near the buckle peripheries (at $\sim \pm 25$ µm) is apparent in the experimental profile, Fig. 3.1(c). We believe this step causes the delamination to extend slightly beyond the nominal perimeter of the fluorocarbon feature.

Using the buckle formula and standard expressions for curvature, it is straightforward to plot the local RoC (an example is shown in Fig. 3.1(d)). The Bessel function profile has

minimum RoC at its peak, given by:

$$\rho_0 \equiv \mathrm{RoC}(0) = \frac{2}{0.7129.\delta}.\left(\frac{a}{\mu}\right)^2 \tag{3.1}$$

For example, for the cavity profile in Fig. 3.1(c), with peak height $\delta = 780$ nm and (effective) base radius $a = 28$ µm, $\rho_0 \sim 190$ µm is predicted, in very good agreement with the numerical circle fit to the top region of the buckle.

As mentioned, minimizing mode volume is crucially important for most CQED applications. Nearly all of the half-symmetric microcavities from the literature (*e.g.*, [12–16, 46, 68, 71, 72, 78, 80, 82, 111]) can be well-described using paraxial Gaussian beam approximations. Moreover, most of them satisfy the condition $L \ll \rho$, where L is the effective cavity length (*i.e.*, the sum of mirror spacing and mirror penetration depths) and ρ is the effective RoC of the curved mirror. Under these conditions, which are well satisfied for the cavities studied here, the minimum beam waist radius for the fundamental mode lies at the flat mirror and is given by $w_0 \sim (\lambda/\pi)^{1/2}(L.\rho)^{1/4}$ [12]. Furthermore, the fundamental mode volume follows as:

$$V_\mathrm{M} \approx (\pi/4) w_0^2 L \approx (\lambda/4) L^{3/2} \rho^{1/2}. \tag{3.2}$$

Small V_M is often pursued through the minimization of ρ [46, 70, 80]. However, as mentioned above, the use of very small RoC mirrors presents fabrication challenges. Furthermore, in practice there is a need to ensure a reasonably large aperture for the curved mirror, in order to minimize diffraction losses. For example, a hemispherical cavity [70] with $L \sim \rho$ represents a marginally stable limiting case, which requires high NA optics for efficient coupling. Moreover, since typically $\rho \gg \lambda/2$, these cavities generally operate at a higher mode order. Indeed, for any cavity that employs a micron-scale RoC mirror, it is challenging to operate in a fundamental longitudinal mode order while retaining an acceptable mirror aperture [46].

Interestingly, Eq. 3.2 shows that V_M is actually more sensitive to L than it is to ρ. Thus, it is preferable for the FPC to operate in the fundamental longitudinal mode order and with minimal mirror penetration [68] (*i.e.*, with $L \sim \lambda/2$), even if this requires the use of a slightly larger value for ρ. Larger ρ also favors mode stability and enables lower diffraction losses. For the buckled cavities, it might be possible to reduce ρ further while

retaining fundamental mode operation, by increasing the film stress, so that similar cavity heights arise from smaller delamination features. Ultimately, the maximum curvature would be limited by factors such as the yield strength of the film materials, since cracking and plastic deformation are likely at high stress levels. Study of these details is left for future work.

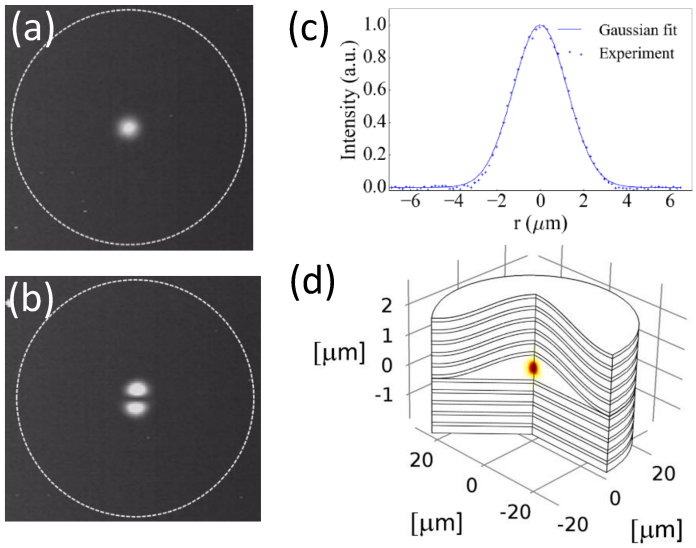

Figure 3.2: (a) Camera image of the fundamental mode for a cavity with peak height ∼780 nm and base diameter ∼50 µm. The white dashed line indicates the perimeter of the buckled dome. (b) Image of the first-order transverse mode for the same cavity. (c) Cross-sectional intensity profile for the fundamental mode. (d) Intensity plot for the fundamental mode, simulated using COMSOL.

3.3 Small V_{M} cavities - optical and tuning properties

The optical properties of the cavities were studied using a transmission setup. Light from a tunable laser operating in the 1520-1620 nm wavelength range was coupled into a cavity using a lensed optical fiber (OZ Optics) with nominal focal length ∼17 mm and spot size diameter ∼10 µm. Transmitted light was collected using an objective lens followed by a beam splitter, with one port coupled to a photodetector and the other to an infrared camera. Figures 3.2(a) and 3.2(b) show typical examples of the fundamental and first-order transverse modes observed for a 50 µm diameter cavity operating at a fundamental longitudinal mode order. As discussed elsewhere [16,82], these cavities have a high degree of cylindrical symmetry and thus preferentially exhibit Laguerre-Gaussian (LG) spatial modes

(see below).

Figure 3.2(c) shows the cross-sectional intensity profile for the fundamental mode, extracted from the camera image and fit to a Gaussian curve with waist $w_0 \sim 2.5$ µm. From the paraxial approximations above, and assuming $\rho \sim \rho_0$, the predicted fundamental mode radius is $w_0 \sim 2.6$ µm. For this calculation, the effective cavity length was estimated as $L \sim 0.95$ µm, including a phase penetration depth of ∼85 nm into each mirror [113]. Note that it is actually the so-called energy penetration depth [92] that is relevant here, but it becomes equivalent to the phase penetration depth for mirrors with near-unity reflectance. Also note that the commonly used expression cited in our previous work [7] significantly overestimates the penetration depth for the Si-terminated mirrors (see [113] for further insight). Using the mentioned values for ρ and L, Eq. 3.2 predicts that $V_{\mathrm{M}} \sim 1.3\lambda^3$ at 1600 nm wavelength.

For further verification of the results, the experimental cavity profile from the ZYGO profilometer was imported into COMSOL. Figure 3.2(d) shows the simulated mode field intensity for the fundamental spatial resonance. From this simulation, $w_0 \sim 2.55$ µm and $V_{\mathrm{M}} \sim 1.25\lambda^3$ were extracted, in good agreement with the paraxial approximations and the experimental results. Slight discrepancies can be attributed to the approximate nature of the Gaussian beam formulae for such small cavities [110], and also to the approximate nature of the formula used to estimate mirror penetration depth [113]. It is worth noting that the high index-contrast of the Si/SiO_2 system is a key reason for the smaller V_{M} here compared to FPCs constructed from smaller RoC, lower-contrast mirrors [111].

As with our earlier work [82], it was straightforward to isolate individual LG modes by adjusting the laser wavelength. Figure 3.3(a) shows a typical transmission scan over the entire wavelength range for the tunable laser. The observed LG spatial mode profiles associated with the first four transverse modes are included, revealing some deviation from cylindrical symmetry. Nevertheless, from transmission scans of many similar cavities, very little polarization-mode splitting was observed. In the paraxial approximation, and assuming a spherical mirror, the wavelength spacing between adjacent transverse modes is given by $\Delta\lambda_{\mathrm{T}} \sim \lambda^3/(2\pi^2 w_0^2)$, or $\Delta\lambda_{\mathrm{T}} \sim 25$ nm for the parameters above based on $\rho \sim \rho_0$. The experimental value is closer to ∼22 nm, which can be attributed to the fact that the higher-

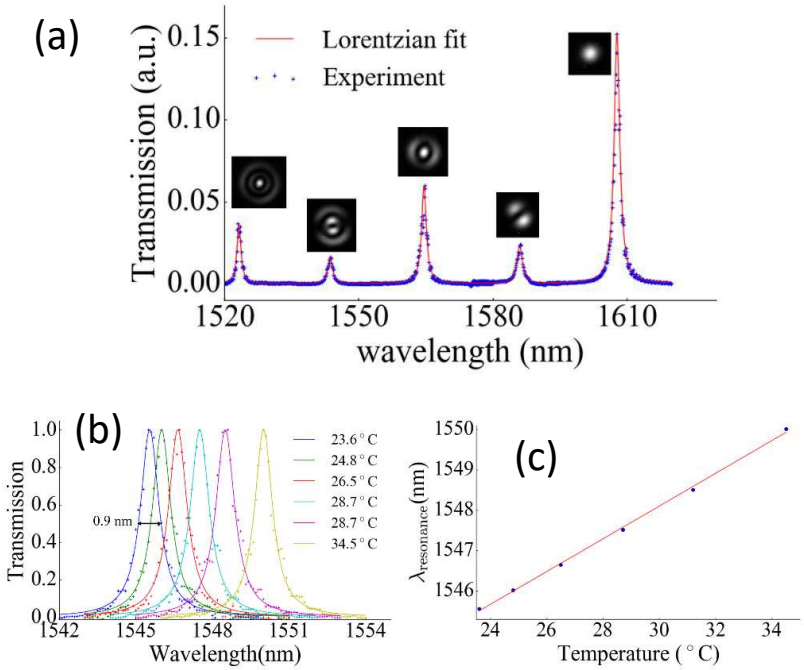

Figure 3.3: (a) Transmission scan for a 50 µm-base-diameter cavity, showing a fundamental resonance at ∼1607 nm. The insets show camera images captured at the adjacent transverse resonance wavelengths. (b) Fundamental resonance line-shape for a similar cavity is plotted at various temperatures as indicated by the legend. (c) The fundamental resonance wavelength versus temperature for the cavity from part b.

order modes occupy a larger portion of the cavity and are thus subject to a higher effective RoC (see Fig. 3.1(d)).

To verify the thermal tuning characteristics of the cavities [15,16], we mounted chips on a thermo-electric cooler. The fundamental line-shape for a particular cavity is plotted at various temperatures in Fig. 3.3(b), and the center resonant wavelength is plotted versus temperature in Fig. 3.3(c), revealing a linear relationship with slope $\sim 0.5\,\mathrm{nm\,K^{-1}}$. In future work, it might be interesting to explore the integration of heating electrodes, to enable tuning of individual microcavities. While the scatter in buckle heights described above (∼50 nm) implies a need for large-range temperature tuning, it is expected that a more tightly controlled fabrication process would enable arrays of domes with much less variation in height.

Also labeled on Fig. 3.3(b) is the linewidth of the fundamental resonance (∼0.9 nm), corresponding to $Q \sim 1700$ for the case shown. From measurements on many cavities of the same size, an average $Q \sim 1800$ was estimated for the fundamental resonance, which

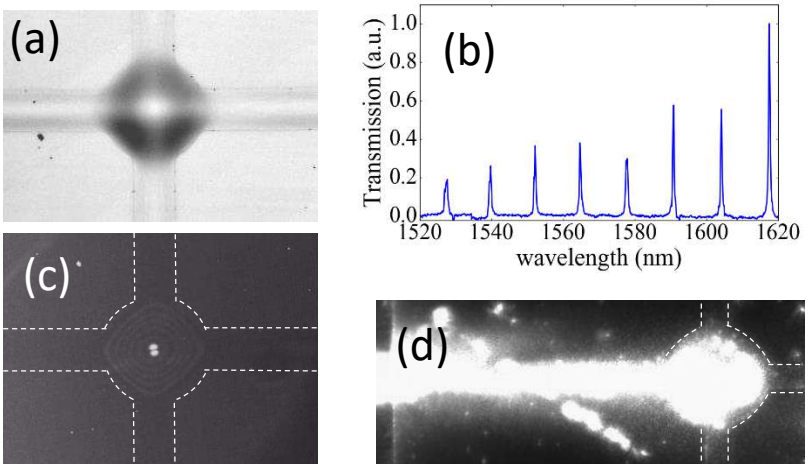

Figure 3.4: (a) Microscope image of a channel-connected dome. The dome has nominal base diameter of 100 µm and the channels are 40 µm wide. (b) Transmission scan for a cavity similar to that shown in part a. (c) Mode-field intensity image for the first-order transverse mode at ∼1617 nm. The perimeter of the buckled pattern is indicated by the white dashed lines. Interference fringes surrounding the mode are due to a white light source used to illuminate the chip for imaging purposes. (d) Image showing the side-coupling of white light into the dome cavity from a cleaved facet at the left side of the image.

also corresponds to the average finesse. This is similar to the reflectance-limited finesse we reported previously [82] for cavities constructed from similar mirrors.

3.4 Channel-connected cavities - optical properties

As discussed above, one of the compelling attributes of FPCs is their potential to provide open access to the high field regions of the cavity mode. This can enable 'side-coupling' of atomic emitters and laser beams (for control and trapping, *etc.*) [63]. We previously explored FIB milling of holes through the buckled upper mirror [16] as a means to provide open access to the inherently closed buckled dome microcavities. An alternative approach is to pattern the fluorocarbon 'release' layer so as to create straight-sided buckle features intersecting with circular dome microcavities (see Fig. 3.1(b)). The straight-sided buckle can potentially act as a microfluidic channel, and as a low-loss waveguide within wavelength ranges determined by the buckle height and the properties of the thin film mirrors [83]. Access to these channels is easily obtained by appropriate dicing of the wafer to create open waveguide facets.

A representative microscope image of a channel-connected dome is shown in Fig. 3.4(a).

The central cavity has a base diameter of 100 µm and the four intersecting channels have width of 40 µm. This geometry led to an average peak buckled dome height of ∼3.2 µm, suitable for observing 4th-order longitudinal modes in the wavelength range of interest. From optical profilometer scans of many similar domes (see for example Fig. 3.1(b)), it was observed that the central portion of the channel-connected dome retains good cylindrical symmetry and a nearly spherical shape. Optical transmission measurements also support this conclusion. For example, Fig. 3.4(b) shows a wide-range scan of a cavity similar to that depicted in Fig. 3.4(a). While the fundamental resonance lies outside the range of the tunable laser, eight higher-order transverse resonances are displayed. The resonance at ∼1617 nm is the first-order (LG01) mode, as verified by the camera image in Fig. 3.4(c), and exhibits $Q \sim 4 \times 10^3$. The transverse modes are equally spaced with $\Delta\lambda_T \sim 12$ nm, indicating an effective RoC on the order of 250 µm. The regular spacing of the transverse modes supports the observation that the central portion of the channel-connected dome is approximately spherical, although some polarization mode splitting is evident in the higher-order line-shapes below ∼1580 nm.

For the wafers studied here, the choice of thin film stress was dictated primarily by the desire to optimize the domes described in Section 3.3. As a result, the straight-sided delamination buckles, with widths in the 20-40 µm range, exhibited peak heights of ∼500 nm or less. Note that the Si/SiO_2-based mirrors provide a wide stop-band, with potential to guide TE-polarized light over the ∼1100-1700 nm wavelength range [83]. Unfortunately, air-guiding of light in this range requires core heights significantly greater than 500 nm.

To facilitate a preliminary demonstration of the side-coupling of light, we diced chips so that the distance between the facet and the dome cavity was on the order of only ∼0.5 mm. For such short channel lengths, it was possible to couple shorter-wavelength light into the dome via the air channel. For example, Fig. 3.4(d) shows light from a supercontinuum source (NKT superK compact) transmitted through a short section of channel and into a dome. Most of the light captured by the camera is subject to considerable loss in the channel, since it lies outside the stop-band of the cladding mirrors, and also because the amorphous silicon cladding layers are strongly absorbing below ∼900 nm. Nevertheless, light guidance along the channel and into the dome is evident, suggesting that the side-coupling of control

and trapping beams should be feasible (*i.e.*, with further refinement of the buckling process to provide a more favorable combination of cavity and channel heights). It is also worth noting that thin film mirrors provide considerable flexibility for customizing the spectral response of hollow waveguides [114]. For materials with extended transparency bands [16], it might be possible to design mirrors that enable cavity modes at certain wavelengths while simultaneously enabling waveguide propagation at shorter wavelengths. There is also potential to exploit recently demonstrated in-plane waveguide reflectors [104], for example to create standing-wave-based trapping beams [115].

3.5 Discussion and conclusions

For many emerging CQED applications, a key figure of merit is the single-atom cooperativity, $C = g^2/2\kappa\gamma$, where g is the atom-cavity coupling rate (*i.e.*, $g = \Omega_R/2$, where Ω_R is the single-photon Rabi frequency), κ is the cavity decay rate, and γ is the non-resonant decay rate of the atomic dipole transition [4, 60, 61]. In keeping with the conventions in Ref. [60], κ and γ are defined as the half-widths of their corresponding spectral line-shapes. In most cases, the cavity modes of interest occupy only a small fraction of solid angular space, so that $\gamma \sim \Gamma_{21}/2$, where $\Gamma_{21} = 1/\tau_{21}$ and τ_{21} is the free-space spontaneous emission lifetime of the atomic transition. Assume a two-level atom placed at the location of maximum field, with its dipole axis aligned to the cavity field, and with its transition in resonance with a cavity mode. Under these conditions, $C = F_P/2$ [60], where F_P is the well-known Purcell factor:

$$F_P \equiv \frac{\gamma_C}{\Gamma_{21}/2} = \frac{3}{4\pi^2}\left(\frac{Q}{V_M/\lambda^3}\right), \tag{3.3}$$

and γ_C is the rate of photon emission into the cavity mode. Furthermore, the fraction of photons emitted into the cavity mode is given by $\beta = F_P/(F_P + 1)$, and can approach unity for high F_P. It is important to note that Eq. 3.3 assumes that the emitter linewidth is significantly smaller than the cavity linewidth [46, 68]; otherwise Q must be replaced by an effective value that incorporates both the emitter and cavity lifetimes.

For the cavities discussed in Section 3.3, with $V_M \sim 1.3\lambda^3$ and $Q \sim 1800$, it follows that $F_P \sim 100$. This high Purcell factor is in large part attributable to the small mode volume achieved. The cavity linewidth is on the order of 1 nm, so that the enhancement

is not restricted to extremely narrow-band emitters. As discussed, the small mode volume is partly attributable to the small mirror penetration depth for the high-index-contrast Si/SiO_2-based mirrors employed. These mirrors are well-suited to Purcell enhancement of 1550-nm-range emitters such as Er-doped SiO_2 or PbS quantum dots. It might also be interesting to explore the use of these mirrors at shorter wavelengths, for the Purcell enhancement of broad-band solid-state emitters [46,68]. In those applications, lower cavity Q (due to higher material loss) can be tolerated, but low V_M is critical. It is worthwhile noting that, the assumption of γ to be half of the free space spontaneous emission is probably an over-estimation. Given the omni-directional reflectance of the mirrors encapsulating the emitter, γ is expected to be smaller than $\Gamma_{21}/2$ which would lead to Purcell enhancement greater than estimated above. However, a more accurate estimation for γ requires rigorous analytical and numerical treatments [116], which is left for future work.

Finally, we note that the buckling self-assembly process offers significant scope for further optimization of the channel-connected cavities. Proper design of the mirrors and the delamination patterns should enable high Q cavities to be interconnected by low-loss channel waveguides. Furthermore, the hollow channels have potential to act as conduits for fluids or even possibly gas-phase media, opening the possibility of CQED studies in future work.

Chapter 4

Thermomechanical characterization of on-chip buckled dome Fabry-Perot microcavities[1]

We report on the thermomechanical and thermal tuning properties of curved-mirror Fabry-Perot resonators, fabricated by the guided assembly of circular delamination buckles within a multilayer a-Si/SiO_2 stack. Analytical models for temperature dependence, effective spring constants, and mechanical mode frequencies are described and shown to be in good agreement with experimental results. The cavities exhibit mode volumes as small as $\sim 10\,\lambda^3$, reflectance-limited finesse $\sim 3 \times 10^3$, and mechanical resonance frequencies in the MHz range. Monolithic cavity arrays of this type might be of interest for applications in sensing, cavity quantum electrodynamics, and optomechanics.

4.1 Introduction

On-chip, high-finesse Fabry-Perot (FP) cavity arrays are of interest for lab-on-a-chip [31] and optomechanical [117] sensing systems. Compelling applications can also be found in the field of cavity quantum electrodynamics (CQED), where a major topic is the strong coupling between atoms and photons in an optical resonant cavity [4]. Optical cavities could potentially be the nodes within a "quantum Internet" [62,63], with information carried by single photons whose quantum state is manipulated at the nodes by interactions with atoms [118, 119].

Although there are alternatives [4], the FP cavity is the prototypical structure for CQED [62,63,118,119]. To facilitate strong coupling (*i.e.*, coherent interactions) between light and

[1]This chapter was published in *JOSA B*, vol. 32, no. 6, pp. 1214-1220, 2015.

matter, the cavity should satisfy several key requirements [11–13, 63, 72]: (1) it should provide access to an air (or vacuum) core, so that atoms can be placed and trapped in the region of high photon density, (2) it should have high finesse ($\mathcal{F}$) and quality factor (Q), so that the decay rate of the cavity mode is small, (3) it should have a small optical mode waist and volume, so that the atom-photon energy exchange rate is high, and (4) it should be tunable so that the cavity can be brought into resonance with the atomic emitter. In addition, cavities should be sufficiently robust to survive and operate at low temperatures and in a vacuum, and (where applicable) should exhibit high mechanical resonance frequencies [72]. It is anticipated that a quantum network will require arrays of tunable microcavities on a single chip [63, 72, 120].

Macroscopic curved mirror cavities with $\mathcal{F} > 10^5$, but relatively large mode volume, were reported more than 10 years ago [7]. Micro-machining techniques such as CO_2 laser ablation [12], focused-ion-beam (FIB) milling [11], and dry etching [71] have been studied in an effort to reduce size and enhance scalability. Often, one or both mirrors are formed on the end of an optical fiber [12], which provides a convenient means for light coupling. $\mathcal{F} \sim 10^5$ and mode volumes as small as $\sim 40\,\mu m^3$ have been achieved [13]. However, serial manufacturing approaches inhibit scalability, and fully monolithic integration strategies remain elusive [14, 121]. Efforts toward the construction of high-finesse Fabry-Perot cavity arrays on a chip [11, 121], particularly with individually tunable cavities [72], are at an early stage.

In a recent paper [82], we described curved-mirror, FP microcavities fabricated using a MEMS-like, thin film buckling technique. With this approach, the roughness of the mirror surfaces is determined mainly by deposition processes, rather than by a micro-machining process. Moreover, owing to their stress-driven self-assembly, the cavities exhibit an uncommon degree of morphological and optical predictability, including reflectance-limited finesse and textbook manifestations of Laguerre-Gaussian and Hermite-Gaussian modes. The technique enables straightforward fabrication of on-chip arrays, and the cavity size can be varied (within limits) through lithographic feature control. As shown below, a fundamental mode volume as small as $\sim 10\,\lambda^3$ has been realized. Since the buckled mirror is essentially a flexible plate, the cavities can be mechanically tuned and have the potential

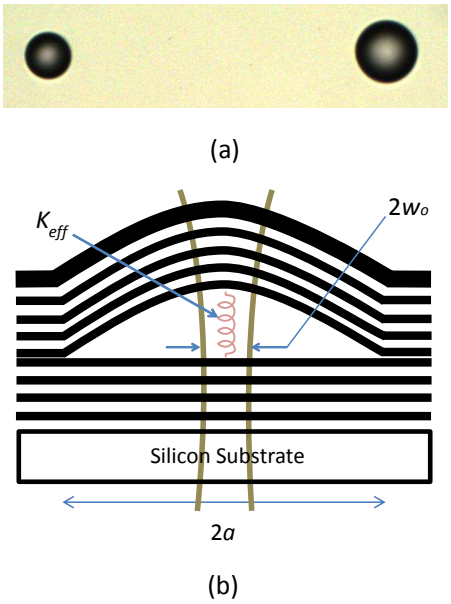

Figure 4.1: (a) Microscope image showing two adjacent domes, one with 150 µm diameter and the other with 200 µm diameter. (b) Schematic illustration of a buckled dome microcavity in a cross section. The waist diameter of the fundamental optical mode ($2w_0$) is typically much less than the diameter of the dome base ($2a$). The upper buckled mirror is a flexible plate with quasi-clamped boundaries, and its movement is subject to an effective spring constant K_{eff}.

for use in the study of optomechanics [117].

Understanding the thermal and mechanical properties [122] of the buckled microcavities is a prerequisite for the applications mentioned above. In the following, we describe the thermal dependence of the cavity resonance, which can be attributed primarily to the coupling between in-plane stress and out-of-plane deflection of the buckled mirror. We also describe the vibrational characteristics of the buckled mirrors, including mechanical resonance frequencies and effective spring constants. Approximate analytical theories are shown to be in good agreement with experimental observations.

4.2 Morphology of the buckled cavities

The buckled microcavities are essentially half-symmetric Fabry-Perot resonators (see Fig. 4.1), and their fabrication and optical properties were described previously [82]. Within a certain range of base diameters ($2a$), the profile of the buckled mirror is well approximated as a spherical dome segment (*i.e.*, a shallow spherical shell). However, the exact shape is

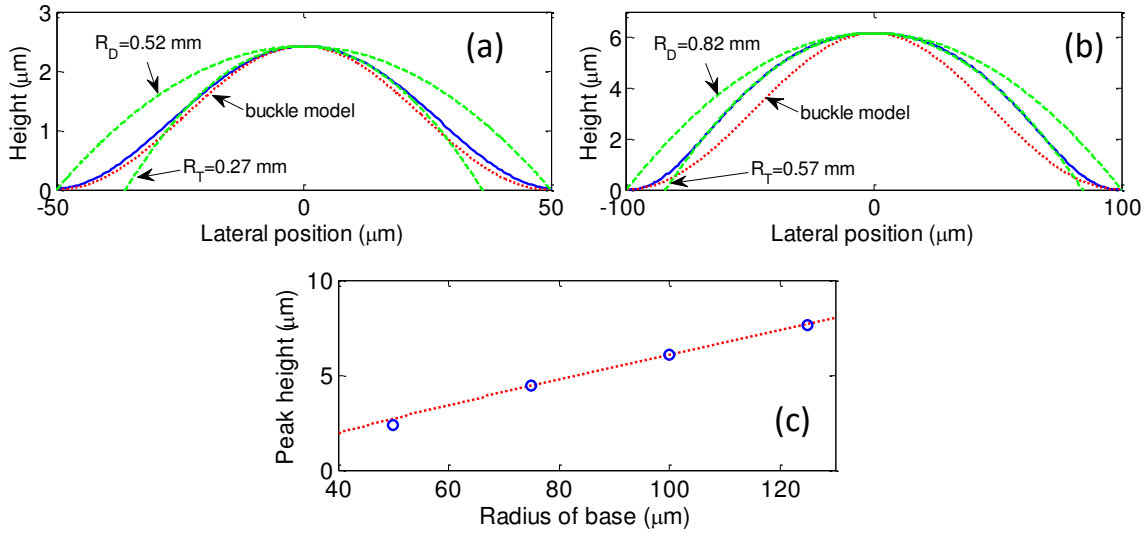

Figure 4.2: (a) Experimental cross-sectional profile (blue solid line) for a typical 100 µm diameter cavity is compared to predictions based on a spherical dome assumption (green dashed lines) and a clamped circular buckle assumption (red dotted line). For the dome model, curves are shown for two different radii of curvature, as explained in the main text. (b) As in part (a), except for a typical 200 µm diameter cavity. (c) A plot of the peak buckle height versus base radius is shown. The red curve is the prediction of the elastic buckling model, assuming pre-buckling compressive stress of 180 MPa and the effective medium parameters shown in Table 4.1. The blue symbols are average values measured for cavities of varying base radius.

determined primarily by elastic buckling mechanics, influenced by secondary factors such as plastic deformation and relaxation of compressive stress over time. Assuming purely elastic deformation and perfectly clamped boundary conditions, the fundamental (axisymmetric) buckling profile for a circular delamination buckle can be expressed [106] as

$$\Delta(r) \approx \delta[0.2871 + 0.7129 J_0(\mu r)], \tag{4.1}$$

where Δ is the vertical deflection, r is the radial coordinate (normalized to a), δ is the peak height of the buckle (see Section 4.3 below), J_0 is the Bessel function of first kind and order zero, and $\mu = 3.8317$.

Figures 4.2(a) and 4.2(b) show the experimental cross-sectional profiles of typical 100 and 200 µm diameter cavities, compared to the shapes predicted for a dome and a clamped, elastic buckle. The experimental profiles were obtained using an optical profilometer (ZYGO NewView 5000). The dome and buckle models were normalized to the experimentally deter-

mined peak height in each case. For the dome model, curves are shown for two curvatures: R_T is the curvature estimated from a fit near the top of the buckled mirror [82], while R_D is the curvature for a dome that spans the same base diameter as the actual buckle. As illustrated by the data shown, the profile of smaller cavities is closer to the predictions of the elastic buckling theory while the profile of larger cavities is more dome-like. Generally speaking, the experimental profiles are intermediate with respect to the dome and buckle models.

Deviation from elastic behavior is not unusual for thin film delamination buckles [123]; plastic deformation near the boundaries can occur, and the assumption of clamped boundaries is often too simplistic. Nevertheless, using the measured pre-buckling compressive stress for the multilayer mirrors ($\sigma \sim 180\,\mathrm{MPa}$) in the elastic buckling model (see Eq. 4.3 below), good agreement between predicted and measured peak buckle heights was verified (see Fig. 4.2(c)).

Given the complex shape of the cavities, an exact treatment of their mechanical properties would require numerical simulations. Here, we aim instead to estimate the main parameters of interest (mechanical resonance frequencies, spring constants, etc.) by employing analytical approximations. This provides significant insight, without obscuring the essential physics. We invoke results from the literature on both shallow spherical shells (the terms "shell" and "dome" are used interchangeably in the following) and buckled circular plates. Encouragingly, predictions from both models are in good mutual agreement and show good agreement with experimental observations.

In keeping with an approximate approach, we treat the buckled mirror as a single plate characterized by effective medium parameters (see Table 4.1). The mirror is a four-period quarter-wave stack (QWS) with a half-wave amorphous Si (a-Si) capping layer, deposited by magnetron sputtering [82]. It has a total thickness of $h \sim 1.6\,\mu\mathrm{m}$ and is $\sim$37 % a-Si and $\sim$63 % SiO_2 by volume. As is well known, thin films show significant variation in their thermal and elastic properties depending on deposition details. This is particularly the case for Young's modulus and the coefficient of thermal expansion (CTE), both of which play central roles in the analyses below. For these quantities, we based the effective medium parameters on values reported in the literature for similar a-Si (*e.g.*, $E \sim 80\,\mathrm{GPa}$ [123],

$\alpha \sim 4.5 \times 10^{-6}\,\mathrm{K}^{-1}$ [124]) and SiO_2 (*e.g.*, $E \sim 60$ GPa, $\alpha \sim 3.1 \times 10^{-6}\,\mathrm{K}^{-1}$ [125]) thin films. The other parameters in Table 4.1 were estimated from widely reported [126, 127] values for SiO_2 and amorphous or polycrystalline Si thin films.

4.3 Optical and thermal tuning properties

In a previous study [82], the optical properties of cavities with base diameters in the 200-400 µm range were reported. For the applications discussed above, cavities with even smaller dimensions (and mode volumes) are desirable. Consider the 100 µm diameter domes, which have peak height $\delta \sim 2.4$ µm and radius of curvature $R_T \sim 270$ µm. In the paraxial approximation, the beam waist (radius) for the fundamental mode of the half-symmetric cavity can be approximated as [12]:

$$w_0 \approx \sqrt{\frac{\lambda}{\pi}}(L.R)^{1/4}, \tag{4.2}$$

where L is the effective cavity length, R is the radius of curvature for the curved mirror, and $L \ll R$ was assumed. Here, $L = \delta + 2d_P$, where d_P is the phase penetration depth into the dielectric mirrors [92]. For operation near the stop-band center wavelength ($\lambda \sim 1.55$ µm here), $L \sim \delta + (\lambda/2)\{1/(n_H - n_L)\}$ [7], where n_H and n_L are the refractive indices of the high and low index layers[2]. Using $n_H = 3.6$ and $n_L = 1.5$ gives $d_P \sim 200$ nm and $L \sim 2.8$ µm. Because of their high index contrast, the phase penetration depth is relatively small for these mirrors. Using $R = R_T$ (since the mode is confined to the central portion of the curved mirror), Eq. 4.2 then produces $w_0 \sim 3.7$ µm.

To experimentally assess the mode size, a tunable laser (Santec TSL-320) was coupled to the cavity using a tapered lensed fiber (Oz Optics) with a nominal focal spot diameter of ~10 µm. The laser was tuned to the frequency of a fundamental resonance to isolate and image the TEM_{00} mode of the cavity [82]. Figure 4.3(a) shows the mode field image captured using an infrared camera, and Fig. 4.3(b) shows a transverse intensity profile extracted from such an image. From the $1/e^2$ intensity points, an experimental mode waist of $w_0 \sim 4.5$ µm was estimated. This is in good agreement with the prediction above, especially given the limited pixel resolution of the camera images. For the standing-wave field associated with

[2]It was discussed in Chapter 3 that given the high-contrast multilayer, $(\lambda/2)\{1/(n_H - n_L)\}$ overestimates the penetration depth for an a-Si/SiO_2 Bragg mirror.

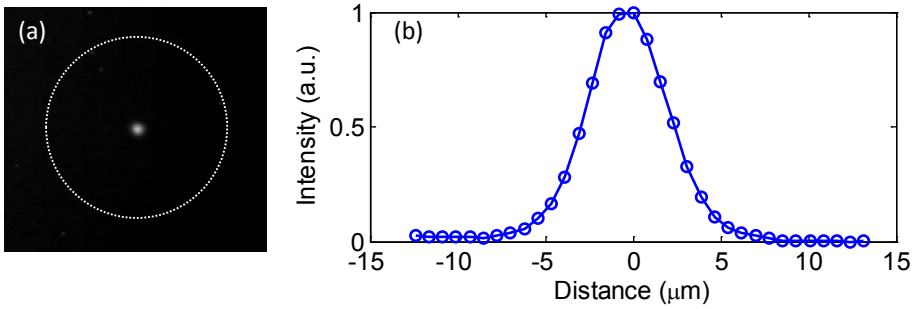

Figure 4.3: (a) Image of the fundamental mode for a 100 µm diameter cavity is shown. The white dotted line indicates the dome boundary. (b) A plot of the transverse intensity profile for the fundamental mode from part (a) is shown. The $1/e^2$ mode waist radius is ∼4.5 µm.

the TEM_{00} mode, the effective mode volume can be approximated as $V_\mathrm{M} \sim (\pi/4){w_0}^2 L$ [12]. For the 100 µm diameter cavity $V_\mathrm{M} \sim 10\lambda^3$; similar wavelength-scaled values have been reported for visible-band cavities [4, 11–14].

The optical linewidth was studied using the tunable laser and a calibrated photodetector. It is worth noting that laser power was set low ($\ll 100\,\mu\mathrm{W}$) for all measurements described here, to avoid significant heating of the mirrors by laser absorption. At higher powers, we observed clear signatures of photo-thermal bistability and hysteresis [128]. Figure 4.4(a) shows a typical fundamental resonance line for a 100 µm diameter cavity, with an input laser power of $\sim 3\,\mu\mathrm{W}$. The experimental linewidth (∼ 0.16 nm) corresponds to $Q \sim 9600$ and finesse $\mathcal{F} \sim Q/m \sim 3200$, where $m = 3$ is the longitudinal mode order for the cavity. This is in excellent agreement with the reflectance-limited finesse we reported for larger cavities with the same mirrors [82].

A unique feature of buckled structures is that in-plane stress is directly coupled with out-of-plane deflection [127, 129, 130]. We have previously developed and experimentally verified a model for the thermal tuning of straight-sided (Euler) delamination buckles [130], where out-of-plane deflection is driven by the difference in CTE between the buckled feature and the substrate. For a clamped *circular* plate, the critical buckling stress is given by [106] $\sigma_\mathrm{c} = 1.2235[E/(1-\nu^2)](h/a)^2$, where E is Young's modulus, ν is Poisson's ratio, and h and a are the thickness and radius of the plate. When compressive stress exceeds σ_c (within limits), the plate buckles with an axisymmetric profile (see Eq. 4.1) and peak height:

$$\delta = h\left[1.96\left(\frac{\sigma}{\sigma_\mathrm{c}}\right) - 1\right]^{1/2}, \tag{4.3}$$

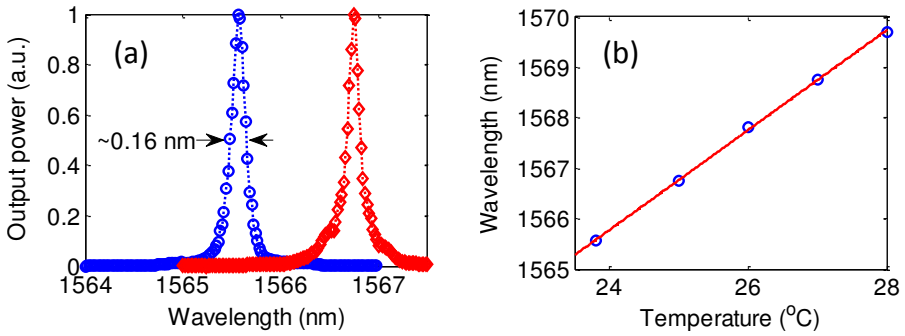

Figure 4.4: (a) Experimental linewidth plots are shown for the fundamental resonance of a 100 µm dome at 23.8 °C (circles) and 25 °C (diamonds). (b) The plot shows the variation in the fundamental resonance wavelength with temperature, revealing a red-shift $\Delta\lambda/\Delta\Theta \sim 1\,\mathrm{nm/K}$. Blue symbols are experimental data points and red line is a linear fit to the data.

where σ is the biaxial compressive stress and $\nu = 0.2$ was assumed. For a pre-existing circular buckle, an analogous treatment to that found in [130] leads to an estimate of the change in peak height with temperature:

$$\frac{\Delta\delta}{\Delta\Theta} \approx 0.80(1+\nu)\frac{a^2}{\delta}\Delta\alpha, \tag{4.4}$$

where $\Delta\alpha$ is the difference in CTE between the buckled plate (*i.e.*, the mirror) and the silicon substrate ($\alpha_{\mathrm{Si}} \sim 2.5 \times 10^{-6}$) and δ is the initial peak height. For example, using $\Delta\alpha \sim 1.1 \times 10^{-6}$, Eq. 4.4 predicts $\Delta\delta/\Delta\Theta \sim 1.1\,\mathrm{nm/K}$ for $a = 50\,\mu\mathrm{m}$ and $\delta = 2.4\,\mu\mathrm{m}$. Moreover, using $\Delta\lambda/\Delta\Theta \sim (\lambda/\delta)(\Delta\delta/\Delta\Theta)$, it follows that $\Delta\lambda/\Delta\Theta \sim 0.7\,\mathrm{nm/K}$ is predicted for the 100 µm diameter domes.

To corroborate this theory, samples were mounted on a thermo-electric cooler and scanned at various temperatures using either the optical profilometer to determine height changes or the tunable laser to determine changes in the spectrum. While the two types of measurements were in good general agreement, the spectral scans were more consistent and repeatable. As shown in Fig. 4.4(b) for a typical 100 µm diameter cavity, a red-shift of the resonant wavelength ($\Delta\lambda/\Delta\Theta \sim 1\,\mathrm{nm/K}$) was observed, in good agreement with the theoretical prediction. Uncertainty in the CTE of the buckled mirror is probably the main source of residual discrepancy. Similar levels of agreement were found for the other cavity sizes.

Table 4.1: Effective medium parameters assumed for the buckled mirrors

	Thickness	**Density**	**Young's modulus**	**Poisson's ratio**	**Thermal expansion coefficient**
Symbol	h (µm)	ρ_{d} (kgm^{-3})	E(GPa)	ν	α(K^{-1})
Value	1.6	2240	70	0.2	3.6×10^{-6}

The temperature dependence provides a convenient tuning mechanism, and integrated heater electrodes might even be feasible. However, this dependence could also be detrimental in some cases. For example, some CQED applications require resonance wavelength stability on the order of 1 pm [72], implying the need for a rather challenging temperature stability of ∼0.001 K for the present cavities. This could be mitigated by matching the CTE of the mirror and substrate [126] and using an alternative (*e.g.*, electrostatic) tuning mechanism.

4.4 Mechanical and dynamic properties

To exploit the buckled microcavities as sensors or optomechanical elements, a basic understanding of their mechanical and dynamical properties is required. This can be accomplished by employing a "thermomechanical calibration" technique [122], where the random motion of a structure is extracted from the noise of a nominally steady-state signal. Here, the steady-state signal is the cavity transmittance at fixed laser detuning [14], and measurements of the noise on this signal yield the mechanical resonance frequencies ω_n for the upper (deformable) mirror. Within the limits of a classic harmonic oscillator model applied to each mode, these frequencies are related to the effective spring constant and mass of the mirror as $\omega_n = (K_{\mathrm{eff},n}/m_{\mathrm{eff},n})^{1/2}$. Furthermore, the mean-square amplitude of the fluctuations in mirror position (for a given mode) can be estimated by invoking the equipartition-of-energy theorem [122, 128]:

$$\left\langle a_n^2(t) \right\rangle = \frac{k_{\mathrm{B}}\Theta}{m_{\mathrm{eff},n}\omega_n^2} = \frac{k_{\mathrm{B}}\Theta}{K_{\mathrm{eff},n}}, \tag{4.5}$$

where k_{B} is the Boltzmann constant and Θ is temperature. In the following, we describe analytical approximations for the resonance frequencies and effective spring constants of the buckled mirror. These are corroborated by experimental results.

4.4.1 Vibrational resonance frequencies

As mentioned, the buckled mirror is analogous to a shallow spherical shell [129], so that analytical treatments from the theories of shells and plates are useful. The natural vibra-

tional frequencies of a thin, flat, and clamped circular plate are well known [131], and can be expressed as $\omega_{\mathrm{P},n} = \Omega_{\mathrm{P},n}(1/a^2)(D/(\rho_\mathrm{d} h))^{1/2}$, where $D = Eh^3/(12(1-\nu^2))$ is the flexural rigidity of the plate and tabulated values of $\Omega_{\mathrm{P,n}}$ are available (*e.g.*, $\Omega_{\mathrm{P},1} = 10.216$, $\Omega_{\mathrm{P},2} = 21.261$, and $\Omega_{\mathrm{P},3} = 34.877$ [131]). Soedel [132] showed that the natural frequencies for a shallow shell (*i.e.*, a dome) can be estimated from those of the equivalent plate with the same projected boundary dimensions:

$$\omega_{\mathrm{S},n} = \sqrt{\omega_{\mathrm{P},n}^2 + E/(\rho_\mathrm{d} R_\mathrm{S}^2)}, \tag{4.6}$$

where R_S is the shell radius of curvature. Consider for example the 200 µm diameter domes, and let $R_\mathrm{S} \sim R_\mathrm{T} = 0.57$ mm, justified by the excellent fit to the dome model in that case (see Fig. 4.2(b)). Using the effective medium parameters from Table 4.1, these equations predict $f_{\mathrm{P},1} = 430$ kHz and $f_{\mathrm{S},1} = 1.6$ MHz. We found that Eq. 4.6 provides accurate predictions of the lowest-order mechanical resonance frequency (especially for the larger cavities, as evidenced below), but is less accurate for the higher-order modes. This might be because the fundamental (axisymmetric) vibrational mode is most closely aligned with the central, spherical portion of the buckle. Furthermore, the shell formula neglects residual stress in the buckled plate [120].

An alternative approach is derived from the literature on the vibration of buckled structures [127, 133]. For a symmetrically buckled structure, the resonance frequency of the lowest-order (*i.e.*, symmetric) vibrational mode can be estimated as [134]

$$\omega_{\mathrm{B},1} = \omega_{\mathrm{P},1}.\sqrt{2}.\sqrt{(\sigma/\sigma_\mathrm{c}) - 1}, \tag{4.7}$$

where σ is the pre-buckling biaxial stress, σ_c is the critical buckling stress (see Eq. 4.3), and $\omega_{\mathrm{P},1}$ is the fundamental resonance frequency for the stress-free and flat plate from above. Encouragingly, Eq. 4.7 produces good agreement with the numerical results for a buckled circular plate reported by Williams *et al.* [133]. For the 200 µm diameter buckle $\sigma_\mathrm{c} \sim 22.8$ MPa and using $\sigma \sim 180$ MPa as above, Eq. 4.7 predicts $f_{\mathrm{B},1} = 1.6$ MHz, in good agreement with both the shell-based prediction and the experimental observations below.

As discussed above, experimental resonance frequencies can be obtained by observing the random thermomechanical motion of the buckled domes. We used a "tuned-to-slope"

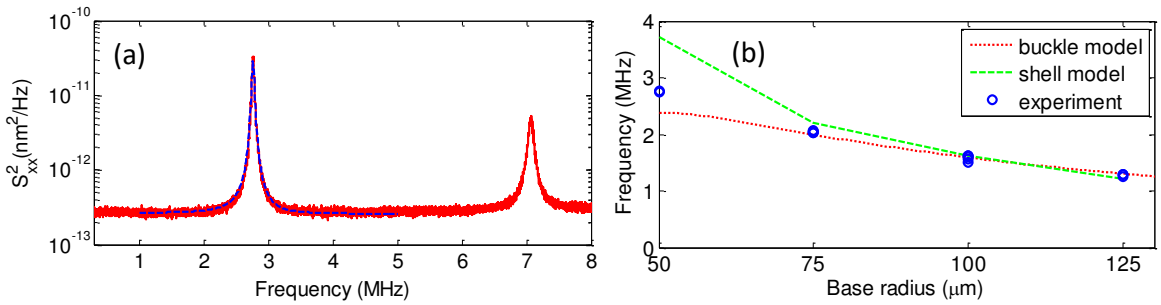

Figure 4.5: (a) Mechanical spectrum arising from thermal noise, captured from a typical 100 µm diameter microcavity. $S^2{}_{XX}$ (red solid line) is the displacement spectral density of the measured time-domain signal [122]. The blue dashed line is a Lorentzian fit. (b) A plot of the fundamental mechanical resonance frequency versus radius of the cavity base is shown. The blue symbols are experimental data points; at least three of each size were measured, but data points overlap in some cases.

technique, similar to that used in other studies [14, 135]. The frequency of a tunable laser was slightly detuned from an optical resonance, nominally at the point of maximum slope of the transmission. Random thermal motion of the buckled mirror changes the cavity length, shifts the optical resonance frequency, and hence changes the transmission through the structure. The time-dependent transmittance of the dome was captured and digitized using a high-speed analog to digital converter. This data was subsequently Fourier transformed and averaged to increase the signal-to-noise ratio.

Figure 4.5(a) shows a typical data set extracted from a 100 µm diameter dome in air and at room temperature. The set of peaks was fit to a series of Lorentz oscillator displacement spectral densities, using thermomechanical calibration techniques described elsewhere [122]. For example, the fit of the fundamental resonance line is shown in the plot. Note that the mechanical Q (*e.g.*, $Q \sim 75$ for the lowest-order mode in the case shown) is undoubtedly affected by squeeze-film damping and viscous damping because of collisions with air molecules [128]. It would be interesting to perform similar measurements in a vacuum, and possibly at a low temperature, but this is left for future work.

As shown in Fig. 4.5(b), the positions of the lowest-order vibrational modes were generally in excellent agreement with the theoretical predictions. For the shell model (Eq. 4.6), we used $R_{\mathrm{S}} = R_{\mathrm{T}}$ as the best estimate of the actual plate curvature. $R_{\mathrm{T}} \sim 0.27$, 0.43, 0.57, and 0.75 mm were experimentally estimated for the 100, 150, 200, and 250 µm diameter

cavities, respectively. Except for the smallest cavities, this resulted in very good agreement between Eq. 4.6 and experimental data. On the other hand, the buckle model (Eq. 4.7) produced reasonable agreement with experimental observations for all cavities studied.

It is worth reiterating that these measurements were performed under ambient pressure, which introduces significant viscous damping of the mechanical motion. Moreover, relatively small-amplitude thermomechanical motion is predicted by Eq. 4.5 (given the relatively high effective spring constant of the present mirrors, discussed below). A numerical treatment of the buckled domes (not shown) confirmed that the low-order mechanical modes have similar wave functions to those of the equivalent flat plate [131], implying that the optical and mechanical modes are characterized by a high degree of spatial overlap in these cavities. Thus, high optomechanical coupling coefficients are anticipated.

4.4.2 Effective stiffness (spring constants)

As per Eq. 4.5, thermomechanical calibration requires, in addition to the resonance frequencies, knowledge of the effective masses or spring constants [122]. The effective spring constant is also needed when assessing bistability and related effects [128]. It is important to note that $K_{\mathrm{eff},n}$ (as well as the effective mass of a given mode) will vary depending on how it is defined [122]. Moreover, deflection (and thus spring constant) will generally depend on the distributed nature of the load. Here, we will use the definition $K_{\mathrm{eff}} = F/\Delta\delta$, where $\Delta\delta$ is the deflection of the buckle at its midpoint and F is the applied force. Note that we have dropped the subscript "n" because the approximate theories presented below are not tailored or restricted to a specific vibrational mode.

Some forces of interest, such as the radiation pressure associated with the fundamental optical mode, are essentially concentrated (point) loads, while others, such as the photothermal force associated with changes in buckle temperature, are more closely approximated as distributed loads. Intuitively, we can expect a larger deflection (*i.e.*, lower effective spring constant) if the force is concentrated near the center of the buckle. In the following, we discuss various approximations for the effective spring constant K_{eff}, and label them as $K_{\mathrm{I,J}}$. Here the subscript I refers to the use of a shell (I = S) or buckle (I = B) model, and the subscript J refers to the assumption of a concentrated point (J = P) or uniformly

distributed (J = U) load.

We first consider the concentrated load, and model the buckled mirror as a shallow shell. In this case, and for small deflections, an effective spring constant can be derived from the work by Lukasiewicz [136]:

$$K_{\mathrm{S,P}} \approx \frac{\pi E h^2}{\sqrt{12(1-\nu^2)}.R_{\mathrm{S}}.\left[(1/w^2)+(1/w)\mathrm{ker}'w\right]}, \tag{4.8}$$

where $w = w_1/l$, w_1 is the radius of the circularly symmetric, concentrated load applied to the center of the shell, and l is a characteristic length for the shell:

$$l = \sqrt{R_{\mathrm{S}}h}/\sqrt[4]{12(1-\nu^2)}. \tag{4.9}$$

Furthermore, "ker$'$" is the first derivative of the Kelvin-real function [137]. Note that Eq. 4.8 does not contain the base radius a; this is because, for a load concentrated near the apex and for small deflections, the central deflection of the shell is approximately independent of the boundary conditions. Consider for example a 200 µm diameter cavity, and the case where $w_1 = w_0 \sim 5\,\mu\mathrm{m}$ (*i.e.*, the approximate size of the fundamental optical cavity mode [82]). This would describe the situation in which the mirror is deflected by radiation pressure forces. Using $R_{\mathrm{S}} \sim R_{\mathrm{T}} = 0.57$ mm (since the bending occurs primarily near the central part of the buckle in this case) and the other parameters from above, then $l \sim 16.4\,\mu\mathrm{m}$, $w \sim 0.3$, and $K_{\mathrm{S,P}} \sim 800\,\mathrm{N\,m^{-1}}$.

Given the approximate nature of the shell analogy, it is useful to corroborate this result using the buckling literature. For a circular buckle, and in the limit of small deflections by a point load, an effective spring constant can be approximated from the numerical results of Jensen [138] (see Fig. 8 of that article):

$$K_{\mathrm{B,P}} \approx \frac{32\pi.E.h^3}{a^2.3(1-\nu^2)}, \tag{4.10}$$

which produces $K_{\mathrm{B,P}} \sim 1000\,\mathrm{N\,m^{-1}}$ for the 200 µm cavity, in reasonable agreement with $K_{\mathrm{S,P}}$.

Of greater interest here is the response to a distributed force (*i.e.*, $F = P\pi a^2$, where P is a uniform pressure) such as the thermal Langevin force that drives thermomechanical motion. As mentioned, a higher effective spring constant is anticipated in this case, and

Table 4.2: Estimated spring constants and effective masses

Base diameter (μm)	m_B **(ng)**	R_D **(mm)**	$K_{S,U}$ **(N/m)**	$m_{eff,1}/m_B$
100	28	0.52	4.7×10^3	0.56
150	63	0.64	5.0×10^3	0.47
200	113	0.82	4.8×10^3	0.42
250	176	1.02	4.7×10^3	0.40

this is supported by results from the literature on delamination buckles. In the limit of small deflections, the deflection for a point-loaded circular buckle is four times that for a uniformly loaded buckle [106]. It follows that $K_{B,U} \sim 4K_{B,P} \sim 4000\,\mathrm{N\,m^{-1}}$ should be a reasonable approximation for the 200 µm cavity.

As above, we seek to corroborate this result by considering the literature on shallow spherical shells. From the work by Jones [139], an effective spring constant for a uniformly loaded shell can be derived:

$$K_{S,U} \approx 64\pi.D \left[1 + (1+\nu)\left(\frac{a^4}{8R_S^2h^2}\right)\right] \Big/ a^2. \tag{4.11}$$

It is somewhat problematic to define the radius of curvature for the real structures, as discussed in Section 4.2. However, it is reasonable to use $R_S \sim R_D$ in Eq. 4.11 because of the strong dependence on the dome radius a. For the 200 µm dome cavity with $R_D = 0.82\,\mathrm{mm}$, we find $K_{S,U} \sim 4800\,\mathrm{N\,m^{-1}}$, which is in good agreement with the buckle estimate. As shown in Table 4.2, Eq. 4.11 predicts that $K_{S,U}$ is fairly insensitive to the cavity size for the structures studied. These cavities are quite rigid in comparison to many MEMS-based cavities [72], and thus should suffer less from thermally induced degradation of the optical finesse [128].

These estimates are expected to be correct to first-order only, especially since the shell and buckle models do not exactly describe the real structures. Nevertheless, the experimental data on the fundamental resonance frequencies suggests that the approximations are reasonable, as follows. Combining ω_1 and $K_{S,U}$ produces an estimate for the effective mass of the fundamental vibrational mode: $m_{eff,1} \sim K_{S,U}/\omega_1^2$. For example, using the data from Fig. 4.5 and Table 4.2 produces $m_{eff,1} \sim 48\,\mathrm{ng}$ for the 200 µm cavity. The buckled mirror has a total mass $m_B \sim 113\,\mathrm{ng}$ in that case, and the ratio $m_{eff,1}/m_B \sim 0.42$ is quite reasonable for the fundamental vibrational mode of a circular plate [122]. As shown in Table 4.2, similarly reasonable results were obtained for the other cavity sizes. A more precise

numerical analysis, and a more detailed experimental study of cavity stiffness, is left for future work.

4.5 Discussion and conclusion

The buckled dome microcavities can be fabricated in large arrays, and might provide an interesting platform for sensing, CQED, and optomechanical coupling studies [4, 31, 117]. The mode volume and finesse demonstrated above are well within the ranges required to achieve strong coupling in CQED experiments [12, 72]. Moreover, the finesse of the cavities might be increased by reducing the absorption loss in the mirrors, for example, by using hydrogenated amorphous silicon for the high index layers. It should be noted that most CQED studies to date use Rb atoms and operate in the 700-800 nm wavelength range. In principle, it should be possible to fabricate compatible buckled microcavities using alternative mirrors based on SiO_2/TiO_2 or SiO_2/Ta_2O_5. The development of such a process, including control over adhesion and stress in these material systems, would be an interesting avenue for future study.

For many of the applications mentioned, it is necessary to incorporate "open access" to the hollow cavity of the nominally enclosed buckle. It might be possible to incorporate this functionality directly into the buckling process by creating an on-chip network of intersecting hollow channels and microcavities [82]. However, a simpler alternative might be to machine "micropores" or "nanopores" directly through the upper mirror using a technique such as focused-ion-beam milling [140]. We hope to explore these options in future work.

Chapter 5

Bistability in buckled dome microcavities[1]

We describe optical bistability in monolithically integrated, curved-mirror Fabry-Perot microcavities. The cavities were fabricated by controlled formation of circular delamination buckles within sputtered Si/SiO_2 multilayers. The dominant source of the bistability is heating due to residual absorption in the mirror layers, which leads to out-of-plane deflection of the buckled mirror. Hysteresis occurs for sub-milliwatt input powers.

5.1 Introduction

Owing to their interesting physics and potential to enable all-optical signal processing systems, bistable and multistable devices have been widely studied [141, 142]. In optics, the archetypal system is a Fabry-Perot resonator in which the cavity medium has nonlinear properties (*e.g.*, saturable absorption or nonlinear refractive index [143]). However, bistability can also arise in cases where the cavity medium is air or vacuum and where the pertinent light-matter interaction occurs at one or both mirrors. Bistability associated with radiation pressure [144] and photothermal forces [145] in "empty" cavities is an important topic for MEMS-based tunable filters [128] and optomechanical sensing [146].

Photothermally derived bistability in air-core Fabry-Perot cavities with metal mirrors was reported by Pirani *et al.* [147]. Later, An *et al.* [148] showed that photothermal bistability could be used to assess the absorption loss of high-finesse, air-core cavities bounded by low-loss dielectric "super-mirrors." Photothermal forces have played an important role

[1]This chapter was published in *Optics letters*, vol. 40, no. 22, pp. 5375-5378, 2015.

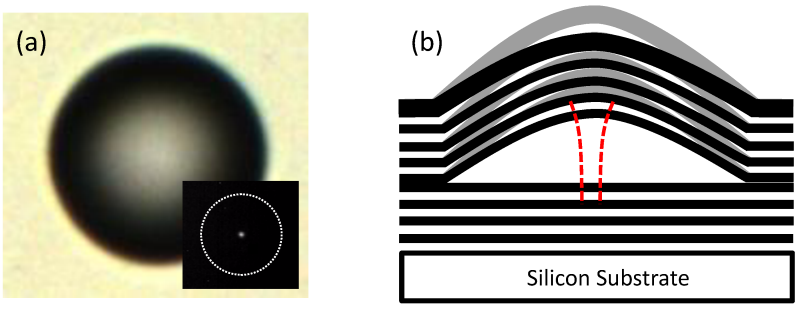

Figure 5.1: (a) Microscope image of a buckled dome microcavity with base diameter of 150 µm. The inset shows a fundamental mode-field intensity image captured by an infrared camera. The perimeter of the dome is indicated by the white dotted line. (b) The buckled mirror is depicted in two different positions, illustrating the effect of changes in temperature. The profile of the fundamental mode is represented by the red dotted line (not to scale).

in the study of dynamical effects such as self-cooling [149] and self-oscillation [150] of Fabry-Perot cavities with a deformable mirror.

We recently reported curved-mirror microcavities [82,83] fabricated by guided formation of delamination buckles within an optical multilayer. Buckled thin film structures present unique options for thermal actuation because there is coupling between in-plane strain and out-of-plane deflection [129]. In previous work, we verified that the buckle cavities are sensitive to temperature, thus exhibiting a shift in resonance wavelength on the order of 1 nm/K [15]. Given their relatively high finesse (linewidth < 0.1 nm), it follows that very small changes in temperature can induce large changes in the cavity resonance conditions. Here, we show that these characteristics result in hysteresis and bistability for input powers in the submilliwatt range.

For the mirror curvatures and cavity dimensions produced by the buckling process [15], the fundamental mode is tightly confined to the center (see Fig. 5.1(a)), with a typical spot diameter on the order of 10 µm. As depicted in Fig. 5.1(b), residual absorption of light circulating in the fundamental mode can induce a temperature change and thereby alter the shape and position of the flexible upper mirror of the cavity. The magnitude of the temperature increase depends on the effective intensity of the light circulating in the cavity, which, in turn, depends on the length of the cavity. Feedback between the cavity field and the cavity length is a well-known source of optical hysteresis [148, 149].

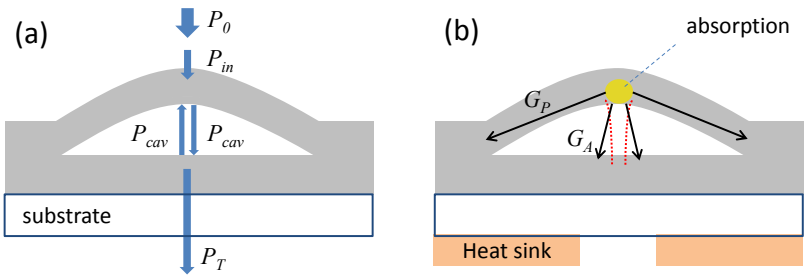

Figure 5.2: Illustration of (a) the power labeling system used and (b) the main thermal mechanisms considered in the analytical model.

5.2 Theoretical analysis

Consider the cavity depicted in Fig. 5.2(a), where some portion (P_{in}) of an incident laser beams power (P_0) is coupled into a (fundamental transverse) cavity mode of interest, defining a coupling efficiency $C_{\mathrm{E}} = P_{\mathrm{in}}/P_0$. Furthermore, some portion (P_{T}) of the coupled power is transmitted through the cavity, and we define the cavity transmittance as $T_{\mathrm{C}} = P_{\mathrm{T}}/P_{\mathrm{in}}$. Assuming nominally identical mirrors with reflectance R, transmittance T, and absorptance A, the cavity transmittance is given by the modified Airy function [89]:

$$T_{\mathrm{C}} = \frac{\psi^2}{1 + K_{\mathrm{F}} \sin^2 \phi} \approx \frac{\psi^2}{1 + K_{\mathrm{F}} \theta^2}, \tag{5.1}$$

where $\psi = T/(T + A)$ is the potential transmittance of each mirror (viewed from inside the cavity) [89], $K_{\mathrm{F}} = 4R/(1 - R)^2$ is the coefficient of finesse, ϕ is the single-pass phase shift, and $\theta = \phi - \{\text{nearest multiple of } 2\pi\}$ [142]. Moreover, the approximation on the right-hand side of Eq. 5.1 holds for small θ (*i.e.*, near resonance), and for those conditions we can assert that

$$\theta = \theta_0 + \Delta\theta = \frac{(\omega - \omega_{\mathrm{cav}})}{c} L + \frac{\omega}{c} \Delta L. \tag{5.2}$$

Here, ω is the angular frequency of the source, c is the speed of light, ω_{cav} and L are the resonance frequency and effective length of the unperturbed cavity, and ΔL is a change in cavity length caused by photothermal effects.

In order to predict bistability, a model for the photothermally driven changes in cavity length is needed. As depicted in Fig. 5.2(b), we assume that the dominant thermal effect is the heating of the buckled mirror through residual absorption of the light circulating within the cavity mode. Note that the resonant mode is a standing wave, whose bidirectional

components (see Fig. 5.2(a)) have power $P_{\mathrm{cav}} = (P_{\mathrm{in}}T_{\mathrm{C}})/T$ [148]. Due to the high finesse of the cavities, P_{cav} can be several hundred times larger than P_{in}. Since the buckled mirror is thermally isolated from its surroundings, absorbed light can cause significant changes in its temperature [126]. For simplicity, however, we neglect temperature variations in the substrate-attached mirror.

The heating of the buckled mirror by the circulating light is undoubtedly nonuniform, with a "hot spot" [137] near the center (assuming laser light is primarily coupled into the fundamental cavity mode, see Fig. 5.1). However, the temperature increase induced by circulating light is relatively small (< 1 K) for the experimental conditions described. Thus, similar to the approach used in Ref. [126], we made the approximation that absorbed laser light induces a uniform temperature increase over the entire volume of the buckled mirror. It can furthermore be shown [126] that heat transfer from a buckled MEMS plate is typically dominated by conduction, with convection and radiation making negligible contributions. Given these assumptions, the problem is characterized by a constant thermal conductance G, a constant heat capacity $C = c_\rho \rho_{\mathrm{d}} V$, and a thermal time constant $\tau = C/G$ [126]. Here, c_ρ, ρ_{d}, and V are the specific heat capacity, density, and volume of the buckled plate, respectively.

As shown in Fig. 5.2(b), we consider two dominant contributions to G. Thermal conductance through the buckled circular plate (and into the substrate via the clamped boundaries) has a characteristic time constant $\tau_P \sim (c_\rho \rho_{\mathrm{d}}/\kappa)(a/2.4)^2$ [129], where κ and a are the thermal conductivity and radius of the plate, respectively. Using $\tau_P = C/G_{\mathrm{P}}$ gives an estimate for the thermal conductance through the plate boundaries, $G_{\mathrm{P}} \sim \pi(2.4)^2 h\kappa$, where h is the thickness of the plate. We also consider conduction through the air gap between the buckled mirror and the substrate, which can be estimated as $G_{\mathrm{A}} \sim \kappa_{\mathrm{air}} A_{\mathrm{B}}/\Delta_{\mathrm{ave}}$, where A_{B} is the area of the buckle and Δ_{ave} is an average air gap over this area. The total thermal conductance is then estimated as $G \sim G_{\mathrm{P}} + G_{\mathrm{A}}$. The temperature increase for the buckled plate can be approximated as $\Delta\Theta \sim P_{\mathrm{cav}} A/G$, where Θ is the temperature. This change in temperature causes a change in cavity length, which can be expressed as [15]

$$\frac{\Delta L}{\Delta \Theta} \approx 0.8\,.\,(1+\nu)\frac{a^2}{\delta}\alpha, \tag{5.3}$$

where ν and α are the effective medium Poisson's coefficient and thermal expansion coefficient for the buckled mirror, and δ is the peak height of the unperturbed cavity. This equation is slightly modified compared with the result in [15], in that we have replaced $\Delta\alpha$ (the difference between the thermal expansion coefficient of the buckle and the substrate) with α here. This is because, as mentioned above, the substrate temperature is assumed to be fixed here. Combining the results from above, we arrive at an expression for the photothermal change in cavity length as a function of the input power coupled into the mode of interest:

$$\Delta L = \left(\frac{\Delta L}{\Delta \Theta}\right) \Delta\Theta \approx \frac{0.8\,.\,(1+\nu)\,.\,a^2\,.\,\alpha\,.\,P_{\text{in}}\,.\,A}{\delta\,.\,T\,.\,G}\,.\,T_{\text{C}}\,. \tag{5.4}$$

Equations 5.1-5.4 can be solved numerically to predict the hysteresis and bistability curves for the cavities.

We have previously shown [15] that an effective medium approach can be used to describe the thermomechanical properties of the buckled mirror. The mirror has total thickness $h \sim 1.65$ µm and is ∼37 % a-Si and ∼63 % SiO_2 by volume. Some relevant effective medium parameters are listed in Table 5.1. The value used for the thermal expansion coefficient was previously discussed [15], while the other parameters were estimated from widely accepted values reported in the literature for a-Si and SiO_2 thin films [126, 127, 151].

In the following, we describe results for domes with 150 µm base diameter (*i.e.*, $a = 75$ µm) and peak height $\delta \sim 4.4$ µm. The volume of the buckled plate is $V \sim 2.9 \times 10^4$ µm^3, which implies a heat capacity $C \sim 4.7 \times 10^{-8}$ J K^{-1}. Using the parameters mentioned produces $G_{\text{P}} \sim 0.5 \times 10^{-4}$ W K^{-1}. Furthermore, assuming $\kappa_{\text{air}} \sim 0.026$ W m^{-1} K^{-1} [126], and $\Delta_{\text{ave}} \sim 3$ µm for a 150 µm diameter buckle gives $G_{\text{A}} \sim 1.5 \times 10^{-4}$ W K^{-1}. As a first-order approximation, we thus assume $G \sim G_{\text{P}} + G_{\text{A}} = 2 \times 10^{-4}$ W K^{-1}. We can furthermore approximate the characteristic time constant for heating and cooling of the buckled mirror as $\tau = C/G \sim 200$ µs.

Both the flat and curved mirrors are four period a-Si/SiO_2 quarter-wave stacks at ∼1550 nm wavelength, although the upper (buckled) mirror is terminated by a half-wave a-Si layer [15, 82]. We know from previous work [82] that $R \sim 0.999$ for both mirrors, implying that $T + A \sim 0.001$ (neglecting scattering losses). However, T and A must be

Table 5.1: Effective medium parameters assumed for the buckled mirrors.

	Density	**Thermal conductivity**	**Specific heat capacity**	**Thermal expansion coefficient**
Symbol	ρ_{d} ($\mathrm{kgm^{-3}}$)	κ ($\mathrm{Wm^{-1}K^{-1}}$)	c_ρ ($\mathrm{Jkg^{-1}K^{-1}}$)	$\alpha(\mathrm{K^{-1}})$
Value	2240	1.5	720	3.6×10^{-6}

estimated separately to accommodate the models described here. From ellipsometry and spectrophotometry measurements (not shown), we estimated an extinction coefficient $k_{\mathrm{Si}} \sim 8 \times 10^{-4}$ at $\lambda_0 \sim 1600$ nm for our a-Si films, consistent with values reported in the literature [152]. Neglecting absorption in the SiO_2 layers, transfer matrix calculations then predict $R = 0.9991$ and $T = A = 0.00045$ for the lower mirror.We used these values in the model described by Eqs. 5.1-5.4 and neglected slight differences predicted for the optical properties of the upper and lower mirror.

5.3 Experimental results

Experimental transmission scans were obtained using a fiber-coupled tunable laser (Santec TSL-510), where either the wavelength or power was varied. For coupling to the microcavities, a fiber collimator with a nominal $1/e^2$ output beam diameter of ∼1.6 mm was connected in series with an objective lens (50x Mitutoyo Plan APO NIR). This resulted in a beam diameter of ∼5 µm at the input of the dome cavity. The chip containing the dome cavities was housed in a sealed chamber and fixed to a large copper plate for heat sinking purposes, with windows providing optical access. The input beam position and wavelength were adjusted in order to preferentially couple the fundamental transverse mode of the cavities. Note that the effective cavity height including mirror penetration [15] is ∼4.7 µm, or approximately $6\,.\,(\lambda/2)$ for resonant wavelengths in the 1550-1600 nm range. For the 150 µm base diameter cavities, the mode field radius of the fundamental transverse mode is $w_0 \sim 5.5$ µm [82]. We can thus estimate an input coupling efficiency $C_{\mathrm{E}} \sim [(2w_{\mathrm{I}}w_0)/(w_{\mathrm{I}}^2 + w_0^2)]^2 \sim 0.55$ [12], where $w_{\mathrm{I}} \sim 2.5$ µm is the mode field radius of the focused input beam.

Experiments were conducted to assess the maximum throughput at resonance. Defining the overall transmittance as $T_{\mathrm{T}} = P_{\mathrm{T}}/P_0$, the predicted maximum transmission can be expressed $T_{\mathrm{T,max}} = C_{\mathrm{E}}\psi^2$. For the values of T, A, and C_{E} mentioned, this produces

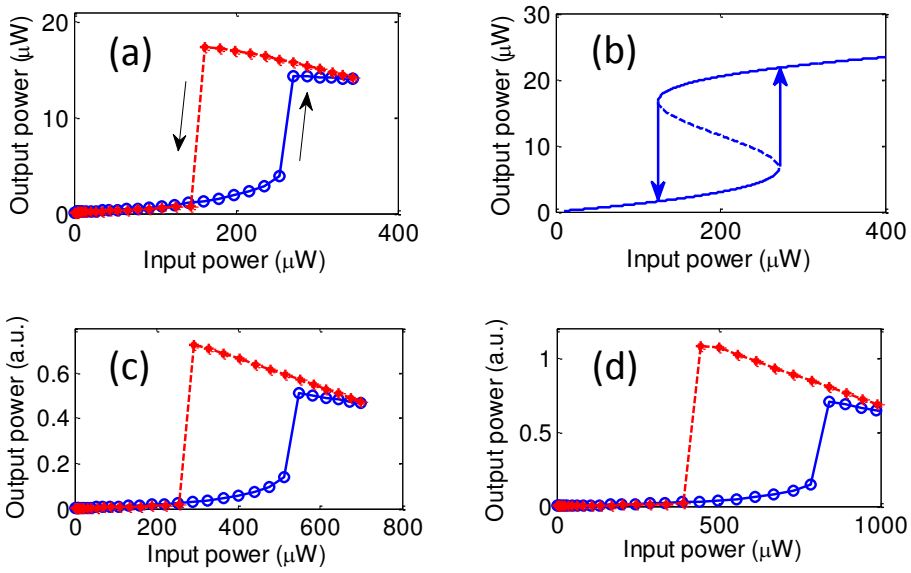

Figure 5.3: (a) Typical experimental hysteresis loop versus input power (P_0), with an initial detuning of ∼0.2 nm. (b) Predicted hysteresis loop versus input power for initial detuning of 0.13 nm. Experimental results for detuning of (c) ∼0.3 nm and (d) ∼0.4 nm are also shown.

$T_{\mathrm{T,max}} \sim 0.14$. Experimental results for several nominally identical cavities gave $T_{\mathrm{T,max}}$ in the 0.09-0.1 range, in reasonable agreement with theory and providing additional validation for the values of R, T, and A estimated above.

To explore hysteresis effects, the laser wavelength (λ) was initially fixed on the long wavelength side of a pre-established "unperturbed cavity" resonance (λ_{C}). We define an initial detuning parameter, $\delta\lambda_{\mathrm{D}} = \lambda - \lambda_{\mathrm{C}}$. For small positive values of $\delta\lambda_{\mathrm{D}}$, increasing the laser power causes heating of the buckled mirror and increases the length of the cavity, thus "pulling" the cavity resonance toward the fixed laser wavelength. This feedback results in a hysteresis loop for increasing and decreasing laser powers, with typical data shown in Fig. 5.3(a) for $\delta\lambda_{\mathrm{D}} \sim 0.2$ nm. The time between subsequent power settings is ∼250 ms for the laser used, which is much greater than the predicted thermal time constant for the dome. Thus, ignoring longer time scale effects discussed below, the scan can be characterized as adiabatic [12, 148], in the sense that there is sufficient time for the buckled plate to reach a steady-state temperature at each new power setting.

Figure 5.3(b) shows the hysteresis loop predicted by Eqs. 5.1-5.4, using the parameters described above and assuming $\delta\lambda_{\mathrm{D}} = 0.13$ nm. For $\delta\lambda_{\mathrm{D}} = 0.2$ nm (the experimental esti-

mate), the model predicted a "switch-up power" of ∼700 µW and a correspondingly larger hysteresis loop. For measurements on numerous cavities and with numerous values of the initial detuning, we found it was consistently necessary to use a slightly smaller detuning in the model, in order to get the best agreement. Nevertheless, experimental data for $\delta\lambda_D \sim 0.3$ and ∼0.4 nm (see Figs. 5.3(c) and 5.3(d)) show the expected trend of higher switch-up powers and larger hysteresis loops with increased detuning [142].

The experimental data in Fig. 5.3 deviates in other ways from the classic bistability loop [141,142]. For example, the upper branches for decreasing and increasing power do not overlap perfectly, and, for decreasing power, the slope of the curve shows an unexpected trend upward. We believe this behavior is mainly attributable to slight increases in the substrate temperature, not accounted for in our simple model. Note that, for high input powers, especially as the resonance condition approaches the laser wavelength, there is significant absorptive energy dissipation in the substrate-attached mirror. This absorption increases the substrate temperature slightly and, thus, shifts the underlying "unperturbed cavity" resonance toward longer wavelengths [15]. The effective offset between the laser wavelength and the cavity resonance wavelength is thereby reduced, in keeping with the discrepancy between the experimental and modeled value of the detuning parameter. Note that a shift in cavity resonance of ∼0.05 nm corresponds to a substrate temperature change of only ∼0.05 K for these cavities [15]. It is challenging to measure, let alone control, temperature with this degree of precision.

We tested this hypothesis by performing wavelength scans (see below), first at very low power, then at high power, and then again at low power. High power scans were confirmed to cause permanent redshifts of the underlying resonance observed at low power. The word "permanent" refers to the very long time scales associated with temperature changes of the substrate, which has a much larger heat capacity than a buckled mirror.

To avoid the need for high laser powers, an alternative strategy for assessing bistability is to perform an adiabatic scan of either cavity length [12, 148] or wavelength [128]. In the present case, scanning in the short-to-long wavelength direction (which we call a forward scan) is expected to produce a broadened and asymmetric line shape at high powers. Figure 5.4(a) shows typical cavity line shapes obtained by fixing the input coupling conditions and

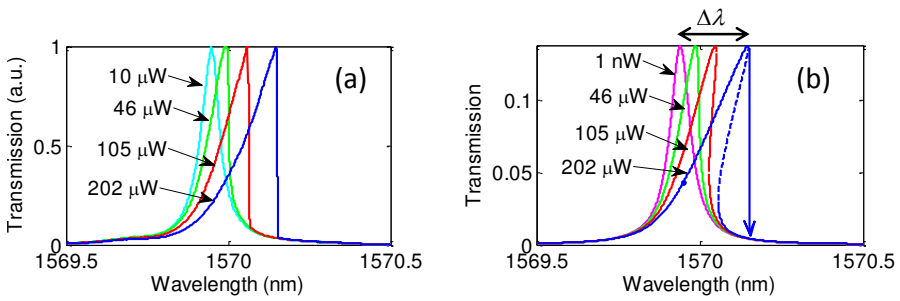

Figure 5.4: (a) Experimental transmission line shapes obtained by scanning from shorter to longer wavelength at various fixed input powers (P_0). (b) Hysteresis loops at fixed power as predicted by the analytical model.

power and scanning the tunable laser (at a rate of 1 nm/s) across the fundamental mode resonance. At low power, the line shape was identical for forward and backward scans, with a linewidth ~0.07 nm corresponding to $Q \sim 2.3 \times 10^4$. At higher power, the forward scan produces an asymmetric line shape peaked at a longer wavelength [128]. Figure 5.4(b) shows the hysteresis curves predicted by solving Eqs. 5.1-5.4 at fixed input power, and with λ_C set to the experimentally observed value (1569.94 nm) for the cavity from Fig. 5.4(a). The model produces excellent agreement with experimental observations, especially at low power.

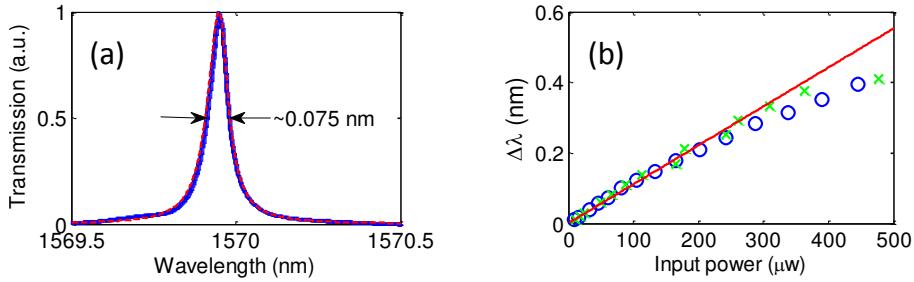

Figure 5.5: (a) Predicted (red dashed line) and measured (blue symbols) line shapes are shown for 10 μW input power. (b) Shift in peak transmission wavelength (relative to λ_C) is plotted versus the input power. Red line is the analytical prediction while the symbols show experimental results for two different domes.

The excellent agreement between the analytical model and the experiment is further illustrated by the data shown in Fig. 5.5(a). Even for the low input power case shown ($P_0 = 10$ μW), there is a noticeable asymmetric broadening of the cavity line shape. At a phenomenological level [148], the asymmetric line shape results because the mirror is slowly

pushed outward as resonance builds and then "snaps" back toward its original position (on the time scale $\tau \sim 200\,\mu s$ in the present case) when the wavelength exceeds $\sim \lambda_C + \Delta\lambda$. This is, of course, associated with the transition from the upper to lower branch of the hysteresis curves shown in Fig. 5.4(b). From the analytical model, the shift in peak wavelength can be estimated as

$$\Delta\lambda = \frac{\lambda_C}{\delta}\frac{\Delta L}{\Delta\Theta}\Delta\Theta_{max} \approx \frac{\lambda_C}{\delta}\frac{\Delta L}{\Delta\Theta}\frac{A\,.\,C_E\,.\,\psi^2}{G\,.\,T}P_0. \tag{5.5}$$

The predictions of Eq. 5.5 are plotted in Fig. 5.5(b), along with experimentally observed $\Delta\lambda$ for two different 150 µm base diameter cavities. In keeping with the discussion above, the model provides good predictive capability at lower powers.

5.4 Discussion and summary

In the above analysis, we have ignored the effects of radiation pressure. To justify this, we define $\Delta L \sim F_{PT}/K_{eff}$, where F_{PT} is an effective photothermal force associated with the mirror absorption and K_{eff} is an effective spring constant. This leads to

$$F_{PT} \approx K_{eff}\frac{\Delta L}{\Delta\Theta}\frac{P_{cav}A}{G}, \tag{5.6}$$

where $K_{eff} \sim 5000\,N\,m^{-1}$ [15]. By comparison, the radiation pressure force on the buckled mirror is given by $F_R = (2/c)P_{cav}$ [128], where c is the speed of light in vacuum. Using Eqs. 5.3 and 5.6 and the parameters from above, it follows that $F_{PT}/F_R > 10^3$ (similar to [149]), confirming that radiation pressure can be safely neglected. We also neglected changes in optical path length due to thermal expansion and thermo-optic and nonlinear index changes (Kerr effects) in the mirror layers. Maximum temperature changes of ~0.1 K are estimated from above, implying thermo-optic index changes $< 10^{-5}$ and thermally induced thickness changes <1 ppm. Furthermore, for peak circulating intensities $<10^6\,W/cm^2$, Kerr effect index changes $<10^{-8}$ are predicted, implying a negligible change in optical path length. Detailed study of these issues would require a numerical simulation of the mode profile within the mirror layers and is left for future work.

Chapter 6

Cut-off-based dual-taper reflectors in on-chip hollow waveguides[1]

We describe back-to-back (dual) tapers embedded within hollow Bragg waveguides clad by omnidirectional Si/SiO_2-based mirrors, and fabricated using a thin film buckling approach. The back-reflection of light subject to mode cutoff in the narrowed tunnel section results in a short-pass transmission characteristic. Thus, the dual taper can act as a waveguide filter with the upper pass-band edge determined by the lithographically controlled height of the tunnel section. We also report preliminary results on the use of these dual tapers as in-plane reflectors (for operation in the cutoff regime), with potential to enable a novel class of open-access hollow-waveguide microcavities.

6.1 Introduction

Axially varying waveguides with mode-cutoff sections have been widely used in the microwave domain, to construct spectral filters [153–155], to explore tunneling phenomena [156], and, more recently, as artificial, epsilon-near-zero (ENZ) media [157]. This is made possible by the low-loss, omnidirectional nature of a metallic reflector at microwave frequencies. As now well-known, dielectric Bragg mirrors of sufficiently high refractive index contrast can also provide an omnidirectional reflection band, thereby exhibiting quasi-metallic properties at optical frequencies [91]. This has led to proposals for mode confinement [158] and spectrometry [159] based on omnidirectional-clad optical waveguides. Nevertheless, the translation of microwave hollow waveguide components [153–157] into the optical domain remains a relatively unexplored theme.

[1]This chapter was published in *Optics Express*, vol. 25, no. 5, pp. 5101–5106, 2017.

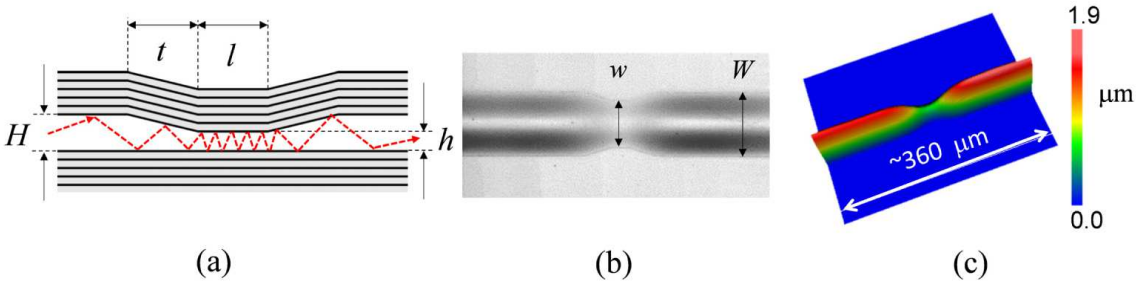

Figure 6.1: (a) Conceptual cross-sectional diagram of a dual taper in a slab Bragg waveguide. The red dotted line depicts the trajectory of a guided ray, at a wavelength not subject to cutoff in the tunnel section. (b) Microscope image showing an as-fabricated dual taper. (c) Surface relief plot of a dual taper extracted using an optical profilometer.

Meanwhile, there is great interest in the use of hollow waveguides (both fibers and integrated waveguides) for applications that require close interactions between light and gas- or liquid-phase media. These applications include sensing and atomic spectroscopy [160], and increasingly lie within the realm of quantum information science [161]. Notably, hollow waveguides with interference-based claddings (*e.g.*, Bragg or ARROW waveguides) can also be designed to act as highly selective spectral filters [114, 162]. By augmenting these properties with methods for engineering the dispersion and axial confinement of guided modes [161], it is expected that a host of new applications in quantum optics might be plausible [163, 164].

We have previously described a thin-film buckling process that can produce axially varying (in both width and height) hollow Bragg waveguides on a chip [83]. In the present work, we used this process to fabricate back-to-back (dual) taper structures. We demonstrate that these dual tapers act as short-pass filters, by reflecting longer wavelength light subject to mode cutoff. We also show preliminary results for a hollow 3-D microcavity formed by cascading two nominally identical dual-taper 'mirrors' [165].

6.2 Device design and fabrication

A schematic diagram of the dual-taper structure, for the case of a slab Bragg waveguide system, is shown in Fig. 6.1(a). The structure is nominally symmetric, with input and output waveguides designed to support one or more guided modes across a spectral range of interest. A central 'tunnel' section is sufficiently narrow such that some longer wavelengths

are subject to mode cutoff. Design parameters include the core heights of the input (H) and tunnel (h) sections, the length of the tapers (t), the length of the tunnel section (l), and the number of periods in and composition of the Bragg cladding mirrors.

When guided light encounters a tapered waveguide section, the associated 'bounce' angle (from a ray optics perspective) becomes increasingly normal relative to the cladding mirrors as the waveguide core narrows [159]. However, provided the wavelength lies within the omnidirectional band of the claddings, and provided the cladding mirrors are sufficiently reflective, radiation loss can be low. For wavelengths that remain guided within the tunnel section, it follows that reasonably efficient transmission through the dual taper is expected, albeit with some slowing and excess radiation of light. On the other hand, for wavelengths subject to cutoff in the tunnel section, back-reflection into reverse propagating modes is anticipated, again with some slowing and excess radiation of light inside the tapered region. Thus, as verified below, one can expect this structure to behave both as a short-pass filter and as a spectrally selective reflector of guided light [165].

While conceptually simple, the proposed structure is not trivial to fabricate for operation at optical frequencies. We employed a buckling self-assembly approach, which is capable of producing axially non-uniform, 3-D hollow waveguides [15, 83, 159]. Figures 6.1(b) and 6.1(c) show microscope and surface relief images, respectively, for a typical dual taper fabricated by appropriate patterning of a low-adhesion layer within a multilayer stack (the pattern is indicated by the perimeter of the waveguide in Fig. 6.1(b)). Since the height of the resulting delamination buckle is approximately proportional to the width of the low-adhesion feature [83], the core heights h and H are easily varied by adjusting the width of the low adhesion strip inside (w) and outside (W) the tunnel region.

6.3 Dual-taper 'mirrors' - experimental results

The hollow waveguides produced by buckling self-assembly have low height-to-width aspect ratio, such that slab-waveguide models can accurately predict their guiding properties [83, 159]. In the following, experimental results on the channel waveguides were corroborated using transfer matrix and finite-element (COMSOL) models of analogous 2-D structures, by equating the slab core thickness to the peak height of the 3-D buckled

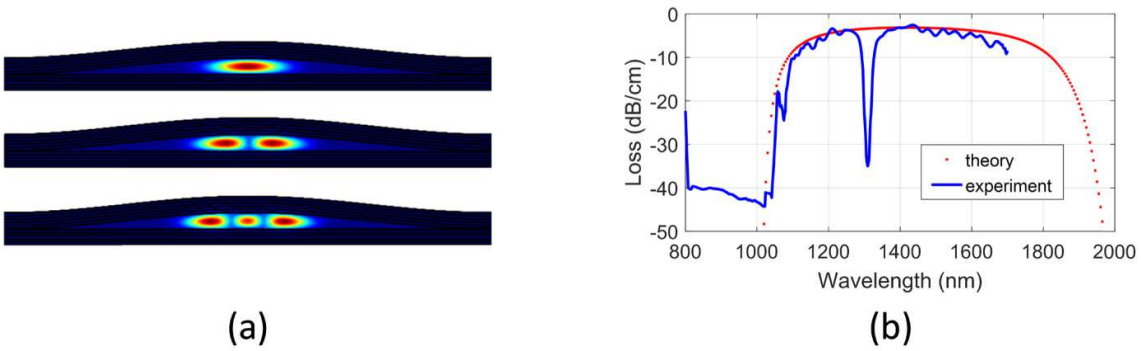

Figure 6.2: (a) Theoretical mode-field profiles for the 3 lowest-loss modes (all TE-polarized) of a waveguide with $W = 60$ µm and $H = 2$ µm. The predicted effective indices are ∼0.92, 0.91, and 0.90, respectively. (b) Spectrally-dependent transmission for a waveguide with $H \sim 1.8$ µm, as measured using a supercontinuum source and OSA (solid), and as predicted by a slab-waveguide model (symbols).

waveguide. The waveguides studied here have 5-period a-Si/SiO_2 Bragg mirrors satisfying a quarter-wavelength condition at ∼1550 nm wavelength. The indices of the films are close to the values reported elsewhere [15] (n∼1.46 and ∼3.7), corresponding to layer thicknesses of ∼265 and ∼104 nm for SiO_2 and a-Si, respectively. These mirrors provide an omnidirectional band spanning the ∼1300-1700 nm range.

In the following, we focus mainly on waveguides with $W = 60$ µm, for which the buckling process produced $H \sim 2$ µm. Numerical simulations (COMSOL) were used to assess the air-guided modes for the 3-D structure, and representative modes are shown in Fig. 6.2(a) (with independently scaled axes, for the sake of clarity). As previously reported [83], the dominant low-loss modes are TE-polarized and have a single lobe in the vertical direction. Thus, a transfer-matrix-based solution [159] for the fundamental TE mode of an analogous slab waveguide provides an accurate prediction of the spectral transmission properties (see Fig. 6.2(b)). In addition to radiation loss, the models incorporated loss arising from absorption in the a-Si layers, which have extinction coefficient $k_{Si} \sim 10^{-3}$ at 1600 nm wavelength [15]. The experimental scan in Fig. 6.2(b) was obtained using a supercontinuum light source (Koheras, ∼600-1700 nm) and an optical spectrum analyzer (OSA, Anritsu). It was normalized to a base scan taken without a sample and scaled using waveguide loss (∼3 dB/cm in the 1550 nm wavelength range) estimated by fitting to scattered light streaks (see below). As shown, the straight guides exhibit a low-loss propagation band in the

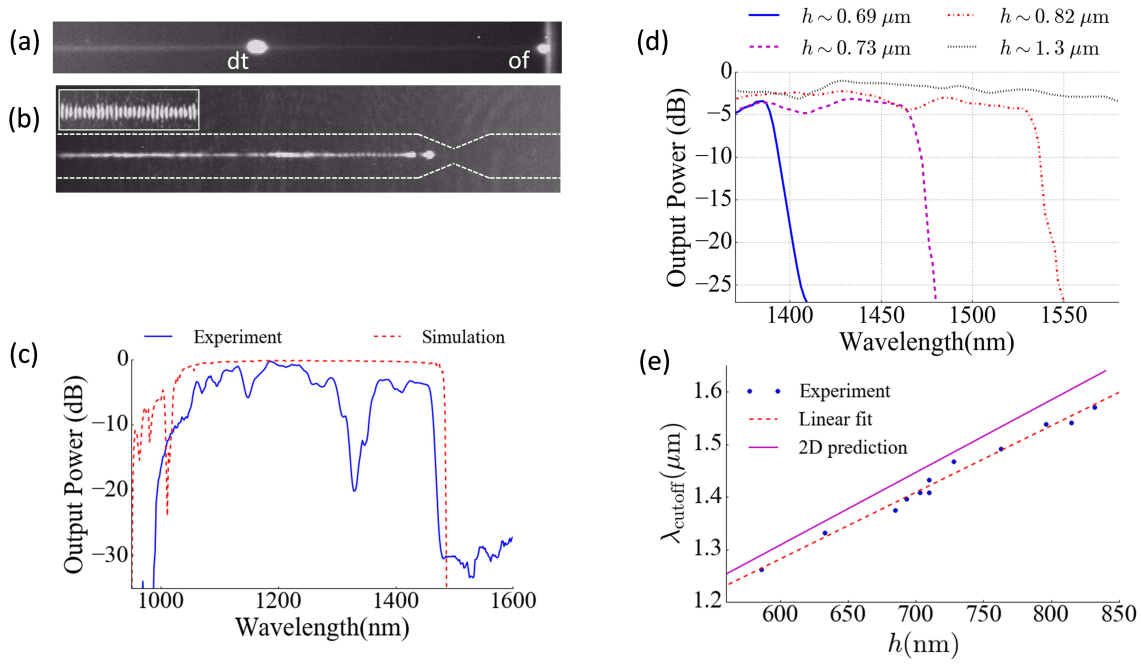

Figure 6.3: (a) Scattered light image for a waveguide containing a dual taper, excited by the supercontinuum source. The locations of the dual taper (dt) and the output facet (of) are labeled. (b) Scattered light image for excitation by a laser tuned to 1602 nm, which is subject to cutoff within the tunnel section for the case shown. The waveguide boundaries are indicated by the dashed line. Inset: higher magnification image of a portion of the standing wave, with period ∼1 µm. (c) Experimental versus theoretically predicted transmission for a dual taper with $h \sim 0.73$ µm. (d) Experimental short-pass transition edges for various dual tapers. (e) Cut-off wavelength versus tunnel height, as measured for a variety of dual tapers and as predicted by an analytical slab model.

∼1100-1800 nm wavelength range. The notch at ∼1300 nm is due to the interaction of TM-polarized light with the 'sidewalls' of the buckled guide, as explained elsewhere [83]. It should be possible to eliminate this notch through slight modifications to the Bragg mirrors [166]. In general, there is significant scope for filter customization in waveguides with interference-based claddings [114, 162].

Next, we explored the properties of waveguides containing dual tapers. Figure 6.3(a) shows a typical scattered light image obtained using the supercontinuum source. The bright central spot is the location of the dual taper, which causes increased scattering and radiation of guided light. Nevertheless, it is clear that some of the light is transmitted and remains well guided towards the output facet. Conversely, Fig. 6.3(b) shows a scattered light image obtained using a laser source, where the laser wavelength is subject to cutoff in the

tunnel section. A lensed fiber was aligned so as to excite primarily the fundamental mode (see Fig. 6.2(a)) in this case. Owing to low roughness-induced scatter in these buckled waveguides, we typically observe little coupling between co-propagating modes [83]. As shown, light incident on the taper is efficiently back-reflected into the reverse-propagating mode, forming a standing-wave of high visibility over the entire input section (several mm).

The spectrally-dependent transmission for a typical dual-taper waveguide (with $h \sim 0.73$ µm, $t \sim 30$ µm, and $l \sim 20$ µm), measured using the supercontinuum source and the OSA, is shown in Fig. 6.3(c). Also shown is the predicted transmission obtained using COMSOL for an analogous slab structure (see Fig. 6.1(a)). While the input waveguide supports low-loss propagation for wavelengths up to ∼1800 nm (see Fig. 6.2(b)), the dual taper introduces an abrupt, short-pass transmission edge, attributable to mode cutoff in the tunnel section for wavelengths above ∼1480 nm in the case shown. This behavior is well-replicated by the numerical results; the slight discrepancy in the transition wavelength can be attributed mainly to the neglect of transverse confinement in the slab model as discussed below. Figure 6.3(d) shows several representative short-pass transmission edges for different values of the tunnel height h. The steepness of the transition is an important filter property [167]; the results shown indicate a 10 dB slope factor (*i.e.*, the width of the 10 dB transition region as a percentage of the transition wavelength) $< 1\%$, and edge steepness ~ -2 dB/nm. This slope was found to increase with increasing tunnel length l.

In keeping with the discussion above, the transition edge is expected to correlate with the onset of cutoff in the tunnel section. In a 2-D approximation, the cutoff wavelength can be assessed analytically [92, 168]:

$$\lambda_C = \frac{[(L_T + L_B)/2]\,\lambda_B + 2h}{[(L_T + L_B)/2] + m}. \tag{6.1}$$

Here, $\lambda_B = 1550$ nm is the Bragg center wavelength of the cladding mirrors, $m = 1$ is the vertical mode order, and L_T and L_B are phase shift coefficients for the top and bottom mirrors, respectively. Note that for $h = \lambda_B/2$, $\lambda_C = \lambda_B$ is correctly predicted [92]. The phase shift coefficients depend on the mirror composition, and can be approximated analytically (see Eqs. (10) and (13) in [168], for example, which are valid for wavelengths near λ_B). For the claddings used here, we estimated $L_T \sim 0.43$ and $L_B \sim 0.44$. The analytical dependence

from Eq. 6.1, for the mirror parameters described above, is plotted in Fig. 6.3(e) along with the experimentally determined transition wavelengths (using a −10 dB criterion). The analytical model was found to be in excellent agreement with the 2-D COMSOL results (*e.g.*, Figure 6.3(c)), indicating that the slight offset between theory and experiment in Fig. 6.3(e) can be attributed to the transverse confinement present in the buckled waveguides [159].

6.4 Microcavities with cutoff-based axial confinement

A recent theoretical work by Wang *et al.* [165] described a Bragg-fiber-based optical microcavity, with transverse confinement provided by omnidirectional mirrors and longitudinal confinement provided by mode cutoff sections. Mesoscopic cavities of this type within on-chip hollow waveguides would be of interest for a variety of applications reliant on the quantum optics of gas-phase media [163, 164], but are difficult to realize using conventional Bragg grating or photonic crystal mirrors [161].

Figures 6.4(a) and 6.4(b) show images of a nominally symmetric microcavity formed by directly cascading two dual-taper mirrors, with $t = 30$ µm, $l = 0$ µm, $w = 42$ µm, and $W = 60$ µm. In other cases, a straight section was inserted between the dual tapers. For brevity, we focus on the cavity shown, for which the buckling process resulted in $h \sim 760$ nm corresponding to a cutoff transition at $\lambda \sim 1480$ nm, and a peak height inside the cavity ∼1.04 µm, less than the height of the input and output waveguides ($H \sim 2$ µm). This implies relatively small mode volume (V_{M}), but likely sub-optimal coupling efficiency. A more detailed study of these trade-offs is left for future work.

Experiments were conducted using a tunable laser (Santec, 1520-1620 nm). As shown in Fig. 6.4(c), it was possible to excite cavity modes by adjusting the laser wavelength and input coupling conditions. For the mode shown, we estimated $V_{\mathrm{M}} < 100\lambda^3$. The theoretical mode field profile (COMSOL) for an analogous slab structure is shown in Fig. 6.4(d), revealing excellent qualitative agreement. Figure 6.4(e) shows the predicted spectral transmission for the slab structure, with a series of resonant transmission peaks near the cut-off transition edge of the dual tapers. Note that the transition edge has lower slope than above, since $l = 0$ here. The peaks exhibit decreasing linewidth (increasing Q) and magnitude as the wavelength increases above the cut-off [165], which can be attributed to the dual-taper

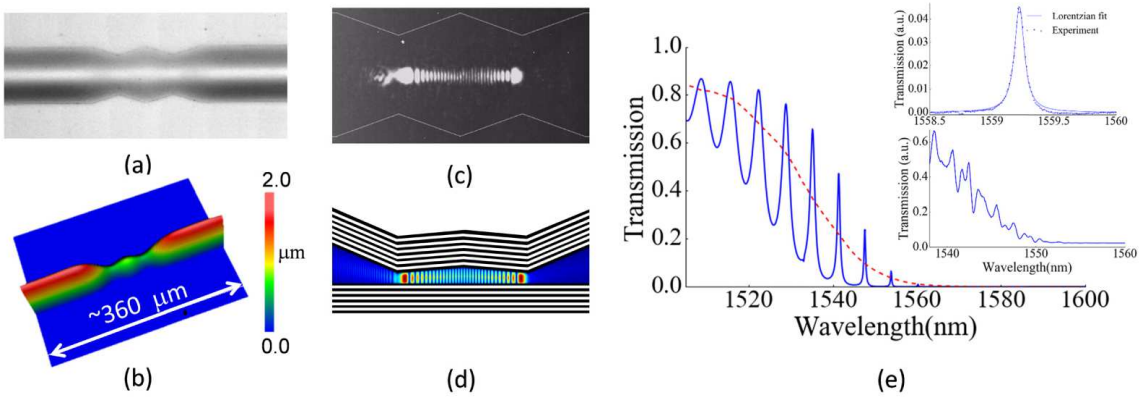

Figure 6.4: (a) Microscope image of a microcavity bounded by dual-taper mirrors. (b) Surface relief image. (c) Scattered light image for a typical resonant mode. (d) Simulated mode field intensity plot for an analogous slab waveguide cavity. (e) Simulated transmission for the analogous slab structure. The red dashed line shows the predicted transmission for a single dual taper in this case. Insets: experimental long- and short-range transmission scans.

mirrors providing increased effective reflectance, but also increased radiative loss. The lower inset in Fig. 6.4(e) shows an experimental scan; discrepancies (in the observed FSR, *etc.*) can be partly attributed to neglect of transverse confinement and multimodal effects in the slab model. Also, such long-range spectral scans were complicated by experimental instabilities. By isolating individual modes in shorter-range scans and increasing detector gain (for example, see the upper inset of Fig. 6.4(e)), we have measured cavity linewidths < 0.1 nm nm, corresponding to cavity $Q > 10^4$, in good agreement with the theoretical predictions. Notably, this combination of Q and V_{M} implies potential for cooperativity $C > 1$ [161], making these cavities intriguing candidates for quantum information studies.

The lower transmission for the high Q modes is indicative of high absorption and radiation losses in the cutoff sections. This could be improved through the use of higher reflectance cladding mirrors, by increasing the number of periods and reducing material loss [165]. Experimental transmission was even lower than predicted; non-optimized coupling, light scattering, and cavity asymmetry [154] are likely major factors. For example, h of the two tunnel sections was mismatched by ∼5 percent for the cavity considered above. Generally speaking, there is significant potential to optimize the fabrication process and the critical cavity parameters – mode volume, finesse, linewidth, *etc.*– through lithographic control of the cavity dimensions and improvement of the Bragg claddings. These improvements

are left for future work.

6.5 Summary and conclusions

We fabricated back-to-back (dual) tapers within integrated hollow Bragg waveguides, and showed that they can be exploited as short-pass transmission filters or cutoff-based reflectors. Preliminary results for 3-D microcavities having axial confinement provided by these dual-taper reflectors were also reported. With further refinement, applications in atomic spectroscopy and sensing are envisioned.

Chapter 7

Conclusions

7.1 Summary of research contributions

The primary goal of this thesis was to exploit thin-film buckling techniques to fabricate on-chip microcavities qualified for applications in CQED and lab-on-a-chip systems. However, the work was not limited to fabrication of new devices, but also included a study of pre-existing buckled-dome microcavities. In what follows, a summary of results and contributions of this PhD work is presented.

7.1.1 Small-mode-volume FPCs

Arrays of cavities were fabricated with high areal density (thousands per square centimeter) by controlled formation of delamination buckles within a-Si/SiO_2 multilayer films. The fabricated devices exhibited fundamental (longitudinal and transverse) mode volume as small as $\sim 1.3\lambda^3$, with $Q = \mathcal{F} \sim 1800$. The small mode volume, along with high Q-factor give rise to a high Purcell factor of ~ 100. Hence, these cavities hold promise as a platform for Purcell enhancement of 1550-nm-range emitters.

In addition, by appropriate design of a patterned low-adhesion layer, high-yield fabrication of channel-connected domes was realized. The channels might facilitate the injection of fluids or gas into the core of the buckled cavities, while also providing the possibility to optically trap quantum emitters in CQED applications.

7.1.2 Thermomechanical characterization of buckled-dome FPCs

The buckled mirror is inherently a flexible plate; thus, buckled FPCs can be mechanically tuned, and might also be used for optomechanical studies. To this end, knowledge about

thermal and mechanical properties of the buckled FPCs is essential. Hence, theoretical and experimental studies were carried out on pre-existing buckled cavities (fabricated in 2011 [82] using a-Si/SiO_2 multilayer films). Extensive data on morphological and optical properties of larger domes with diameters in the range of 200-400 µm had been presented in [82]; however, for thermomechanical characterization, we restricted our attention mainly to smaller domes with 100 µm diameter. For those cavities, optical studies revealed a mode volume as low as $\sim 10\lambda^3$ at 1550 nm wavelength.

Given the coupling between in-plane stress and out-of-plane deflection of the top mirror in buckled FPCs, cavity length can be thermally adjusted, and thereby the resonance wavelength can be tuned to a targeted wavelength. According to optical measurements, 100 µm-diameter domes manifested thermal tunability of ∼1 nm/K, corroborated by our theoretical model. Therefore, the thermal dependence allows an expedient tuning technique, and in future work might be augmented by integrating electrodes to thermally control the resonance wavelength of individual cavities.

Finally, a 'thermomechanical calibration' technique was employed to estimate vibrational resonance frequencies by monitoring the thermally-induced variations in an otherwise steady-state optical signal tuned near an optical resonance frequency of a cavity. Measurements on numerous cavities, ranging from 100 to 250 µm in diameter, indicated that the top mirror vibrates with frequencies in the MHz range, in good agreement with a theoretical analysis derived from the literature on the mechanics of plates and shells. In addition, invoking some of the same literature, the effective spring constants and effective masses of the buckled mirrors were estimated.

7.1.3 Bistability of buckled-dome FPCs

It was observed that the optical transmission of buckled FPCs clearly broadened at increased input powers as low as 100 µW. This prompted us to undertake a study of bistability in the buckled microcavities. Amongst various impacts of light on the buckled mirror, such as radiation pressure, thermo-electric and nonlinear index changes, photothermal effects (*i.e.*, residual absorption in mirror layers) was shown to have the primary influence on the resulting bistability and hysteresis. The bistable behavior was approximated using a

theoretical model, which showed good agreement with our optical measurements.

7.1.4 Cutoff-based-mirror microcavities

This project was mainly motivated by the idea of incorporating cutoff-based in-plane mirrors into hollow waveguides to axially confine light. This could enable a new class of microcavities, potentially useful for enhancing the light-matter interaction inside the core of a hollow waveguide, while not obstructing the passage of fluid or gas media [163, 164]. A few approaches for axial confinement of light in hollow waveguides have been proposed in the literature, such as modulation of the refractive index of a photoresist (deposited inside the inner core or injected into selected holes) of a hollow core photonic crystal fiber (HCPC) and integration of photonic crystal membranes into a HCPC [169]. Chip-scale implementations of Bragg mirrors into ARROW waveguides by etching selected thin-film layers has also been proposed [161, 169]. Although possible, these techniques are difficult to realize and require several fabrication steps.

Adapting the buckling process, we fabricated axially varying waveguides with embedded (back-to-back) dual-tapers, having a central 'tunnel' section subject to cutoff. This enables high reflection of light within a certain wavelength range. Numerous dual-taper waveguides were studied and optically measured, showing a cutoff wavelength, above which transmission is very low, while remaining highly transmitting at shorter wavelengths. These measurements were well-replicated by 2D numerical simulations of analogous slab waveguide structures.

Furthermore, hollow waveguides containing two cascaded dual tapers were designed and studied, with the aim of realizing 3D confinement of light for the applications mentioned above. From preliminary measurements, $Q > 10^4$ was estimated for some cavities, in good agreement with theoretical predictions. Mode volume for a 100 µm length cavity was shown to be $< 100\lambda^3$, implying cooperativity $C > 1$. Thus, this class of optical resonator could be an excellent choice for CQED studies.

7.2 Future work

7.2.1 buckled-dome microcavities

Buckled-dome microcavities have potential to be an excellent choice for quantum information and lab-on-a-chip system studies, thanks to their high Q-factor and small mode volume. However, there still exist several avenues for future studies. As noted in Chapter 2, the reflectance of a Bragg mirror is ultimately limited by the scattering and absorption losses of the constituent layers. Thus, in order to increase the reflectance of these mirrors, and in turn, to attain higher reflectance-limited finesse, a-Si layers could be replaced by hydrogenated amorphous silicon, which is known to have lower loss in the near infrared [152].

While the thermal dependence of the cavity resonance is useful as a tuning mechanism, it is also associated with thermal instability, especially for CQED applications where resonance wavelength stability on the order of 1 pm is sought [72]. In future work, this might be mitigated by growing multilayer films with effective CTE that is better matched to the CTE of the substrate. In that case, an alternative tuning mechanism, such as electro-static tuning, might be needed.

In a preliminary study, cavities intersecting with channel waveguides were fabricated as described in Chapter 3. The waveguides might provide a conduit for liquid or gaseous analytes to be introduced into the cavity volume. Fabricating an interface to introduce such analytes is another opportunity left for future work. One possible method could be etching reservoirs at the entrance of waveguide channels, and enclosing these by a thick PDMS layer. In this way, liquids could be injected through the holes perforated in PDMS and then made to flow into the waveguide cores.

7.2.2 Cutoff-based-mirror microcavities

The resonance transmission of dual-taper microcavities was shown to be very low, and this was attributed to radiation losses at the cutoff sections and absorption in the silicon layers. As noted above, absorption losses might be mitigated by the use of hydrogenated silicon films, which might then also enable the use of higher number of periods in the mirrors (to improve reflectance). Numerical simulations have shown that by keeping the same number of periods, but reducing the extinction coefficient, transmission can be increased. In addition,

this class of resonator was found to exhibit a higher degree of thermal stability compared to the dome-shaped cavities. Nonetheless, a complete thermomechanical characterization is left for future work.

Bibliography

[1] M. Born and E. Wolf, *Principles of optics: electromagnetic theory of propagation, interference and diffraction of light*. Elsevier, 2013.

[2] G. R. Fowles, *Introduction to modern optics*. Courier Corporation, 1975.

[3] P. Atherton, N. K. Reay, J. Ring, and T. Hicks, "Tunable fabry-perot filters," *Optical Engineering*, vol. 20, no. 6, pp. 206805–206805, 1981.

[4] K. J. Vahala, "Optical microcavities," *Nature*, vol. 424, no. 6950, pp. 839–846, 2003.

[5] L. P. Schuler, J. S. Milne, J. M. Dell, and L. Faraone, "Mems-based microspectrometer technologies for nir and mir wavelengths," *Journal of Physics D: Applied Physics*, vol. 42, no. 13, p. 133001, 2009.

[6] A. Yariv and P. Yeh, *Photonics: Optical Electronics in Modern Communications (6th Edition)*. Oxford University Press, 2006.

[7] C. J. Hood, H. Kimble, and J. Ye, "Characterization of high-finesse mirrors: Loss, phase shifts, and mode structure in an optical cavity," *Physical Review A*, vol. 64, no. 3, p. 033804, 2001.

[8] P. Tayebati, P. Wang, M. Azimi, L. Maflah, and D. Vakhshoori, "Microelectromechanical tunable filter with stable half symmetric cavity," *Electronics Letters*, vol. 34, no. 20, pp. 1967–1968, 1998.

[9] R. A. Crocombe, "Mems technology moves process spectroscopy into a new dimension," *Spectroscopy Europe*, vol. 16, no. 3, pp. 16–19, 2004.

[10] M. Ebermann, N. Neumann, K. Hiller, E. Gittler, M. Meinig, and S. Kurth, "Recent advances in expanding the spectral range of mems fabry-perot filters," in *MOEMS-MEMS*, pp. 75940V–75940V, International Society for Optics and Photonics, 2010.

[11] P. R. Dolan, G. M. Hughes, F. Grazioso, B. R. Patton, and J. M. Smith, "Femtoliter tunable optical cavity arrays," *Optics letters*, vol. 35, no. 21, pp. 3556–3558, 2010.

[12] D. Hunger, T. Steinmetz, Y. Colombe, C. Deutsch, T. W. Hänsch, and J. Reichel, "A fiber fabry-perot cavity with high finesse," *New Journal of Physics*, vol. 12, no. 6, p. 065038, 2010.

[13] A. Muller, E. B. Flagg, J. R. Lawall, and G. S. Solomon, "Ultrahigh-finesse, low-mode-volume fabry-perot microcavity," *Optics letters*, vol. 35, no. 13, pp. 2293–2295, 2010.

[14] L. Greuter, S. Starosielec, D. Najer, A. Ludwig, L. Duempelmann, D. Rohner, and R. J. Warburton, "A small mode volume tunable microcavity: development and characterization," *Applied physics letters*, vol. 105, no. 12, p. 121105, 2014.

[15] M. H. Bitarafan, H. Ramp, T. W. Allen, C. Potts, X. Rojas, A. J. R. MacDonald, J. P. Davis, and R. G. DeCorby, "Thermomechanical characterization of on-chip buckled dome fabry-perot microcavities," *JOSA B*, vol. 32, no. 6, pp. 1214–1220, 2015.

[16] C. Potts, A. Melnyk, H. Ramp, M. Bitarafan, D. Vick, L. LeBlanc, J. Davis, and R. DeCorby, "Tunable open-access microcavities for on-chip cavity quantum electrodynamics," *Applied Physics Letters*, vol. 108, no. 4, p. 041103, 2016.

[17] P. Zijlstra, P. M. Paulo, and M. Orrit, "Optical detection of single non-absorbing molecules using the surface plasmon resonance of a gold nanorod," *Nature nanotechnology*, vol. 7, no. 6, pp. 379–382, 2012.

[18] J. N. Anker, W. P. Hall, O. Lyandres, N. C. Shah, J. Zhao, and R. P. Van Duyne, "Biosensing with plasmonic nanosensors," *Nature materials*, vol. 7, no. 6, pp. 442–453, 2008.

[19] Y. Sun and X. Fan, "Optical ring resonators for biochemical and chemical sensing," *Analytical and bioanalytical chemistry*, vol. 399, no. 1, pp. 205–211, 2011.

[20] I. M. White, H. Zhu, J. D. Suter, N. M. Hanumegowda, H. Oveys, M. Zourob, and X. Fan, "Refractometric sensors for lab-on-a-chip based on optical ring resonators," *IEEE Sensors Journal*, vol. 7, no. 1, pp. 28–35, 2007.

[21] P. Domachuk, I. Littler, M. Cronin-Golomb, and B. Eggleton, "Compact resonant integrated microfluidic refractometer," *Applied Physics Letters*, vol. 88, no. 9, p. 093513, 2006.

[22] D. Dorfner, T. Zabel, T. Hürlimann, N. Hauke, L. Frandsen, U. Rant, G. Abstreiter, and J. Finley, "Photonic crystal nanostructures for optical biosensing applications," *Biosensors and Bioelectronics*, vol. 24, no. 12, pp. 3688–3692, 2009.

[23] Y. Liu and H. Salemink, "Photonic crystal-based all-optical on-chip sensor," *Optics express*, vol. 20, no. 18, pp. 19912–19920, 2012.

[24] I. M. White and X. Fan, "On the performance quantification of resonant refractive index sensors," *Optics express*, vol. 16, no. 2, pp. 1020–1028, 2008.

[25] W. Song, X. Zhang, A. Liu, C. Lim, P. Yap, and H. M. M. Hosseini, "Refractive index measurement of single living cells using on-chip fabry-perot cavity," *Applied physics letters*, vol. 89, no. 20, p. 203901, 2006.

[26] S. Campopiano, R. Bernini, L. Zeni, and P. M. Sarro, "Microfluidic sensor based on integrated optical hollow waveguides," *Optics letters*, vol. 29, no. 16, pp. 1894–1896, 2004.

[27] M. R. Islam, M. M. Ali, M. H. Lai, K. S. Lim, and H. Ahmad, "Chronology of fabry-perot interferometer fiber-optic sensors and their applications: a review," *Sensors*, vol. 14, no. 4, pp. 7451–7488, 2014.

[28] Y. Guo, H. Li, K. Reddy, H. S. Shelar, V. R. Nittoor, and X. Fan, "Optofluidic fabry-perot cavity biosensor with integrated flow-through micro-/nanochannels," *Applied Physics Letters*, vol. 98, no. 4, p. 041104, 2011.

[29] Z. Ran, Y. Rao, H. Deng, and X. Liao, "Miniature in-line photonic crystal fiber etalon fabricated by 157 nm laser micromachining," *Optics letters*, vol. 32, no. 21, pp. 3071–3073, 2007.

[30] T. Wei, Y. Han, Y. Li, H. L. Tsai, and H. Xiao, "Temperature-insensitive miniaturized fiber inline fabry-perot interferometer for highly sensitive refractive index measurement," *Optics Express*, vol. 16, no. 8, pp. 5764–5769, 2008.

[31] A. Trichet, J. Foster, N. Omori, D. James, P. Dolan, G. Hughes, C. Vallance, and J. Smith, "Open-access optical microcavities for lab-on-a-chip refractive index sensing," *Lab on a Chip*, vol. 14, no. 21, pp. 4244–4249, 2014.

[32] J. Hu, X. Sun, A. Agarwal, and L. C. Kimerling, "Design guidelines for optical resonator biochemical sensors," *JOSA B*, vol. 26, no. 5, pp. 1032–1041, 2009.

[33] M. I. Cheema, C. Shi, A. M. Armani, and A. G. Kirk, "Optimizing the signal to noise ratio of microcavity sensors," *IEEE Photonics Technology Letters*, vol. 26, no. 20, pp. 2023–2026, 2014.

[34] T. Yoshie, L. Tang, and S. Y. Su, "Optical microcavity: sensing down to single molecules and atoms," *Sensors*, vol. 11, no. 2, pp. 1972–1991, 2011.

[35] X. Zhou, L. Zhang, and W. Pang, "Performance and noise analysis of optical microresonator-based biochemical sensors using intensity detection," *Optics Express*, vol. 24, no. 16, pp. 18197–18208, 2016.

[36] L. Chin, A. Liu, C. Lim, X. Zhang, J. Ng, J. Hao, and S. Takahashi, "Differential single living cell refractometry using grating resonant cavity with optical trap," *Applied Physics Letters*, vol. 91, no. 24, p. 243901, 2007.

[37] L. Chin, A. Liu, C. Lim, C. Lin, T. Ayi, and P. Yap, "An optofluidic volume refractometer using fabry-perot resonator with tunable liquid microlenses," *Biomicrofluidics*, vol. 4, no. 2, p. 024107, 2010.

[38] R. St-Gelais, J. Masson, and Y. A. Peter, "All-silicon integrated fabry-perot cavity for volume refractive index measurement in microfluidic systems," *Applied physics letters*, vol. 94, no. 24, p. 243905, 2009.

[39] H. Shao, D. Kumar, and K. L. Lear, "Single-cell detection using optofluidic intracavity spectroscopy," *IEEE Sensors Journal*, vol. 6, no. 6, pp. 1543–1550, 2006.

[40] P. Liu, H. Huang, T. Cao, Z. Tang, X. Liu, Z. Qi, M. Ren, and H. Wu, "An optofluidics biosensor consisted of high-finesse fabry-perot resonator and micro-fluidic channel," *Applied Physics Letters*, vol. 100, no. 23, p. 233705, 2012.

[41] P. Liu, H. Huang, T. Cao, X. Liu, Z. Qi, Z. Tang, and J. Zhang, "An ultra-low detection-limit optofluidic biosensor with integrated dual-channel fabry-perot cavity," *Applied Physics Letters*, vol. 102, no. 16, p. 163701, 2013.

[42] H. Wu, H. Huang, M. Bai, P. Liu, M. Chao, J. Hu, J. Hao, and T. Cao, "An ultra-low detection-limit optofluidic biosensor based on all glass fabry-perot cavity," *Optics express*, vol. 22, no. 26, pp. 31977–31983, 2014.

[43] A. A. Trichet, P. R. Dolan, D. James, G. M. Hughes, C. Vallance, and J. M. Smith, "Nanoparticle trapping and characterization using open microcavities," *Nano Letters*, vol. 16, no. 10, pp. 6172–6177, 2016.

[44] M. Mader, J. Reichel, T. W. Hänsch, and D. Hunger, "A scanning cavity microscope," *Nature communications*, vol. 6, 2015.

[45] C. Vallance, A. A. Trichet, D. James, P. R. Dolan, and J. M. Smith, "Open-access microcavities for chemical sensing," *Nanotechnology*, vol. 27, no. 27, p. 274003, 2016.

[46] H. Kelkar, D. Wang, D. Martín-Cano, B. Hoffmann, S. Christiansen, S. Götzinger, and V. Sandoghdar, "Sensing nanoparticles with a cantilever-based scannable optical cavity of low finesse and sub-λ^3 volume," *Physical Review Applied*, vol. 4, no. 5, p. 054010, 2015.

[47] X. Liang, A. Liu, C. Lim, T. Ayi, and P. Yap, "Determining refractive index of single living cell using an integrated microchip," *Sensors and Actuators A: Physical*, vol. 133, no. 2, pp. 349–354, 2007.

[48] B. Helbo, A. Kristensen, and A. Menon, "A micro-cavity fluidic dye laser," *Journal of Micromechanics and Microengineering*, vol. 13, no. 2, p. 307, 2003.

[49] M. T. Hill and M. C. Gather, "Advances in small lasers," *Nature Photonics*, vol. 8, no. 12, pp. 908–918, 2014.

[50] A. J. Kuehne and M. C. Gather, "Organic lasers: Recent developments on materials, device geometries, and fabrication techniques," *Chemical Reviews*, vol. 116, no. 21, pp. 12823–12864, 2016.

[51] D. M. Coles, A. A. Trichet, P. R. Dolan, R. A. Taylor, C. Vallance, and J. M. Smith, "Diffusion-driven continuous-wave-pumped organic dye lasers," *Laser & Photonics Reviews*, vol. 9, no. 5, pp. 538–544, 2015.

[52] W. Wang, C. Zhou, T. Zhang, J. Chen, S. Liu, and X. Fan, "Optofluidic laser array based on stable high-q fabry-perot microcavities," *Lab on a Chip*, vol. 15, no. 19, pp. 3862–3869, 2015.

[53] R. K. Patel, A. A. Trichet, D. M. Coles, P. R. Dolan, S. M. Fairclough, M. A. Leontiadou, S. Tsang, D. J. Binks, E. Jang, H. Jang, *et al.*, "Gain spectroscopy of solution-based semiconductor nanocrystals in tunable optical microcavities," *Advanced Optical Materials*, vol. 4, no. 2, pp. 285–290, 2016.

[54] T. Zhang, C. Zhou, W. Wang, and J. Chen, "Generation of low-threshold optofluidic lasers in a stable fabry-perot microcavity," *Optics & Laser Technology*, vol. 91, pp. 108–111, 2017.

[55] T. D. Ladd, F. Jelezko, R. Laflamme, Y. Nakamura, C. Monroe, and J. L. O'Brien, "Quantum computers," *Nature*, vol. 464, no. 7285, pp. 45–53, 2010.

[56] N. Gisin and R. Thew, "Quantum communication," *Nature photonics*, vol. 1, no. 3, pp. 165–171, 2007.

[57] N. Thomas-Peter, B. J. Smith, A. Datta, L. Zhang, U. Dorner, and I. A. Walmsley, "Real-world quantum sensors: evaluating resources for precision measurement," *Physical review letters*, vol. 107, no. 11, p. 113603, 2011.

[58] V. Giovannetti, S. Lloyd, and L. Maccone, "Advances in quantum metrology," *Nature photonics*, vol. 5, no. 4, pp. 222–229, 2011.

[59] I. Aharonovich, A. D. Greentree, and S. Prawer, "Diamond photonics," *Nature Photonics*, vol. 5, no. 7, pp. 397–405, 2011.

[60] A. Reiserer and G. Rempe, "Cavity-based quantum networks with single atoms and optical photons," *Reviews of Modern Physics*, vol. 87, no. 4, p. 1379, 2015.

[61] H. Mabuchi and A. Doherty, "Cavity quantum electrodynamics: coherence in context," *Science*, vol. 298, no. 5597, pp. 1372–1377, 2002.

[62] H. J. Kimble, "The quantum internet," *Nature*, vol. 453, no. 7198, pp. 1023–1030, 2008.

[63] S. Ritter, C. Nölleke, C. Hahn, A. Reiserer, A. Neuzner, M. Uphoff, M. Mücke, E. Figueroa, J. Bochmann, and G. Rempe, "An elementary quantum network of single atoms in optical cavities," *Nature*, vol. 484, no. 7393, pp. 195–200, 2012.

[64] F. Liang and Q. Quan, "Detecting single gold nanoparticles (1.8 nm) with ultrahigh-q air-mode photonic crystal nanobeam cavities," *Acs Photonics*, vol. 2, no. 12, pp. 1692–1697, 2015.

[65] R. Miura, S. Imamura, R. Ohta, A. Ishii, X. Liu, T. Shimada, S. Iwamoto, Y. Arakawa, and Y. Kato, "Ultralow mode-volume photonic crystal nanobeam cavities for high-efficiency coupling to individual carbon nanotube emitters," *Nature communications*, vol. 5, 2014.

[66] A. Goban, C.-L. Hung, S.-P. Yu, J. Hood, J. Muniz, J. Lee, M. Martin, A. McClung, K. Choi, D. E. Chang, *et al.*, "Atom–light interactions in photonic crystals," *Nature communications*, vol. 5, p. 3808, 2014.

[67] M. Fox, *Quantum optics: an introduction*, vol. 15. OUP Oxford, 2006.

[68] H. Kaupp, T. Hümmer, M. Mader, B. Schlederer, J. Benedikter, P. Haeusser, H. C. Chang, H. Fedder, T. W. Hänsch, and D. Hunger, "Purcell-enhanced single-photon emission from nitrogen-vacancy centers coupled to a tunable microcavity," *Physical Review Applied*, vol. 6, no. 5, p. 054010, 2016.

[69] T. Steinmetz, Y. Colombe, D. Hunger, T. Hänsch, A. Balocchi, R. Warburton, and J. Reichel, "Stable fiber-based fabry-perot cavity," *Applied Physics Letters*, vol. 89, no. 11, p. 111110, 2006.

[70] G. Cui, J. Hannigan, R. Loeckenhoff, F. Matinaga, M. Raymer, S. Bhongale, M. Holland, S. Mosor, S. Chatterjee, H. Gibbs, *et al.*, "A hemispherical, high-solid-angle optical micro-cavity for cavity-qed studies," *Optics express*, vol. 14, no. 6, pp. 2289–2299, 2006.

[71] G. Biedermann, F. Benito, K. Fortier, D. Stick, T. Loyd, P. Schwindt, C. Nakakura, R. Jarecki Jr, and M. Blain, "Ultrasmooth microfabricated mirrors for quantum information," *Applied Physics Letters*, vol. 97, no. 18, p. 181110, 2010.

[72] C. Derntl, M. Schneider, J. Schalko, A. Bittner, J. Schmiedmayer, U. Schmid, and M. Trupke, "Arrays of open, independently tunable microcavities," *Optics express*, vol. 22, no. 18, pp. 22111–22120, 2014.

[73] G. V. Prakash, L. Besombes, T. Kelf, J. J. Baumberg, P. Bartlett, and M. Abdelsalam, "Tunable resonant optical microcavities by self-assembled templating," *Optics letters*, vol. 29, no. 13, pp. 1500–1502, 2004.

[74] Y. Colombe, T. Steinmetz, G. Dubois, F. Linke, D. Hunger, and J. Reichel, "Strong atom–field coupling for bose–einstein condensates in an optical cavity on a chip," *Nature*, vol. 450, no. 7167, pp. 272–276, 2007.

[75] M. Trupke, E. A. Hinds, S. Eriksson, E. Curtis, Z. Moktadir, E. Kukharenka, and M. Kraft, "Microfabricated high-finesse optical cavity with open access and small volume," *Applied Physics Letters*, vol. 87, no. 21, p. 211106, 2005.

[76] M. Trupke, J. Goldwin, B. Darquié, G. Dutier, S. Eriksson, J. Ashmore, and E. Hinds, "Atom detection and photon production in a scalable, open, optical microcavity," *Physical review letters*, vol. 99, no. 6, p. 063601, 2007.

[77] S. Johnson, P. R. Dolan, and J. M. Smith, "Diamond photonics for distributed quantum networks," *Progress in Quantum Electronics*, 2017.

[78] J. Benedikter, T. Hümmer, M. Mader, B. Schlederer, J. Reichel, T. W. Hänsch, and D. Hunger, "Transverse-mode coupling and diffraction loss in tunable fabry-perot microcavities," *New Journal of Physics*, vol. 17, no. 5, p. 053051, 2015.

[79] M. Uphoff, M. Brekenfeld, G. Rempe, and S. Ritter, "Frequency splitting of polarization eigenmodes in microscopic fabry-perot cavities," *New Journal of Physics*, vol. 17, no. 1, p. 013053, 2015.

[80] D. Najer, M. Renggli, D. Riedel, S. Starosielec, and R. J. Warburton, "Fabrication of mirror templates in silica with micron-sized radii of curvature," *Applied Physics Letters*, vol. 110, no. 1, p. 011101, 2017.

[81] T. Purdy and D. Stamper-Kurn, "Integrating cavity quantum electrodynamics and ultracold-atom chips with on-chip dielectric mirrors and temperature stabilization," *Applied Physics B*, vol. 90, no. 3-4, pp. 401–405, 2008.

[82] T. Allen, J. Silverstone, N. Ponnampalam, T. Olsen, A. Meldrum, and R. DeCorby, "High-finesse cavities fabricated by buckling self-assembly of a-si/sio$_2$ multilayers," *Optics express*, vol. 19, no. 20, pp. 18903–18909, 2011.

[83] E. Epp, N. Ponnampalam, W. Newman, B. Drobot, J. McMullin, A. Meldrum, and R. DeCorby, "Hollow bragg waveguides fabricated by controlled buckling of si/sio$_2$ multilayers," *Optics express*, vol. 18, no. 24, pp. 24917–24925, 2010.

[84] M. H. Bitarafan and R. G. DeCorby, "Small-mode volume, channel-connected fabry-perot microcavities on a chip," *Optica*, in press.

[85] M. Bass, E. V. Stryland, D. R. Williams, and W. L. Wolfe, *Handbook of optics*, vol. 2. McGraw-Hill New York, 1995.

[86] H. Bilger, P. Wells, and G. Stedman, "Origins of fundamental limits for reflection losses at multilayer dielectric mirrors," *Applied optics*, vol. 33, no. 31, pp. 7390–7396, 1994.

[87] F. Bielsa, A. Dupays, M. Fouché, R. Battesti, C. Robilliard, and C. Rizzo, "Birefringence of interferential mirrors at normal incidence," *Applied Physics B: Lasers and Optics*, vol. 97, no. 2, pp. 457–463, 2009.

[88] J. D. Joannopoulos, S. G. Johnson, J. N. Winn, and R. D. Meade, *Photonic crystals: molding the flow of light*. Princeton university press, 2011.

[89] H. A. Macleod, *Thin-film optical filters*. CRC press, 4th ed., 2010.

[90] J. N. Winn, Y. Fink, S. Fan, and J. Joannopoulos, "Omnidirectional reflection from a one-dimensional photonic crystal," *Optics letters*, vol. 23, no. 20, pp. 1573–1575, 1998.

[91] Y. Fink, J. N. Winn, S. Fan, C. Chen, J. Michel, J. D. Joannopoulos, and E. L. Thomas, "A dielectric omnidirectional reflector," *Science*, vol. 282, no. 5394, pp. 1679–1682, 1998.

[92] D. I. Babic and S. W. Corzine, "Analytic expressions for the reflection delay, penetration depth, and absorptance of quarter-wave dielectric mirrors," *Quantum Electronics, IEEE Journal of*, vol. 28, no. 2, pp. 514–524, 1992.

[93] B. Saleh and M. Teich, *Fundamental of photonics*. John Wiley & Sons, New York, 1991.

[94] J. S. Moon and A. M. Shkel, "Analysis of imperfections in a micromachined tunable-cavity interferometer," in *SPIE's 8th Annual International Symposium on Smart Structures and Materials*, pp. 46–53, International Society for Optics and Photonics, 2001.

[95] R. Syms, "Principles of free-space optical microelectromechanical systems," *Proceedings of the Institution of Mechanical Engineers, Part C: Journal of Mechanical Engineering Science*, vol. 222, no. 1, pp. 1–18, 2008.

[96] A. Siegman, "Hermite–gaussian functions of complex argument as optical-beam eigenfunctions," *JOSA*, vol. 63, no. 9, pp. 1093–1094, 1973.

[97] Wikipedia, "Gaussian beam — wikipedia, the free encyclopedia," 2015. [Online; accessed 3-April-2015].

[98] J. T. Verdeyen, "Laser electronics," *Laser electronics/2nd edition/, by JT Verdeyen, Englewood Cliffs, NJ, Prentice Hall, 1989, 640 p.*, 1989.

[99] M. Bitarafan, H. Ramp, C. Potts, T. Allen, J. Davis, and R. DeCorby, "Bistability in buckled dome microcavities," *Optics letters*, vol. 40, no. 22, pp. 5375–5378, 2015.

[100] T. Tamir, "Leaky waves in planar optical waveguides," *Nouvelle Revue d'Optique*, vol. 6, no. 5, p. 273, 1975.

[101] S. O. Kasap, *Optoelectronics and photonics: principles and practices*. Prentice Hall, 2012.

[102] A. Yariv and P. Yeh, "Optical waves in crystal propagation and control of laser radiation," 1983.

[103] M. W. Moon, K. R. Lee, K. H. Oh, and J. W. Hutchinson, "Buckle delamination on patterned substrates," *Acta Materialia*, vol. 52, no. 10, pp. 3151–3159, 2004.

[104] M. H. Bitarafan, C. A. Potts, and R. G. DeCorby, "Cut-off-based dual-taper reflectors in on-chip hollow waveguides," *Optics Express*, vol. 25, no. 5, pp. 5101–5106, 2017.

[105] V. Khanna, "Adhesion–delamination phenomena at the surfaces and interfaces in microelectronics and mems structures and packaged devices," *Journal of Physics D: Applied Physics*, vol. 44, no. 3, p. 034004, 2010.

[106] J. W. Hutchinson and Z. Suo, "Mixed mode cracking in layered materials," *Advances in applied mechanics*, vol. 29, pp. 63–191, 1991.

[107] A. Melnyk, C. Potts, T. Allen, and R. DeCorby, "Visible-range hollow waveguides by guided buckling of ta_2 o_5/sio_2 multilayers," *Applied optics*, vol. 55, no. 13, pp. 3645–3649, 2016.

[108] Y. M. Sabry, D. Khalil, and T. Bourouina, "Monolithic silicon-micromachined free-space optical interferometers onchip," *Laser & Photonics Reviews*, vol. 9, no. 1, pp. 1–24, 2015.

[109] A. D. Melnyk, "Fabrication of visible range hollow bragg waveguides," Master's thesis, University of Alberta, 2016.

[110] R. Pennington, G. D'Alessandro, J. Baumberg, and M. Kaczmarek, "Spectral properties and modes of surface microcavities," *Physical Review A*, vol. 79, no. 4, p. 043822, 2009.

[111] A. A. Trichet, P. R. Dolan, D. M. Coles, G. M. Hughes, and J. M. Smith, "Topographic control of open-access microcavities at the nanometer scale," *Optics express*, vol. 23, no. 13, pp. 17205–17216, 2015.

[112] A. Bick, C. Staarmann, P. Christoph, O. Hellmig, J. Heinze, K. Sengstock, and C. Becker, "The role of mode match in fiber cavities," *Review of Scientific Instruments*, vol. 87, no. 1, p. 013102, 2016.

[113] L. Brovelli and U. Keller, "Simple analytical expressions for the reflectivity and the penetration depth of a bragg mirror between arbitrary media," *Optics communications*, vol. 116, no. 4-6, pp. 343–350, 1995.

[114] P. Measor, B. S. Phillips, A. Chen, A. R. Hawkins, and H. Schmidt, "Tailorable integrated optofluidic filters for biomolecular detection," *Lab on a chip*, vol. 11, no. 5, pp. 899–904, 2011.

[115] J. Thompson, T. Tiecke, N. de Leon, J. Feist, A. Akimov, M. Gullans, A. Zibrov, V. Vuletić, and M. Lukin, "Coupling a single trapped atom to a nanoscale optical cavity," *Science*, vol. 340, no. 6137, pp. 1202–1205, 2013.

[116] W. Liang, Y. Huang, A. Yariv, Y. Xu, and S.-Y. Lin, "Modification of spontaneous emission in bragg onion resonators," *Optics express*, vol. 14, no. 16, pp. 7398–7419, 2006.

[117] M. Metcalfe, "Applications of cavity optomechanics," *Applied Physics Reviews*, vol. 1, no. 3, p. 031105, 2014.

[118] O. Painter, "Microphotonics: Playing with atoms," *Nature Photonics*, vol. 1, no. 11, pp. 615–616, 2007.

[119] L. Duan, "Quantum physics: A strong hybrid couple," *Nature*, vol. 508, no. 7495, pp. 195–196, 2014.

[120] A. Abdelrahman, T. Mukai, H. Häffner, and T. Byrnes, "Coherent all-optical control of ultracold atoms arrays in permanent magnetic traps," *Optics express*, vol. 22, no. 3, pp. 3501–3513, 2014.

[121] Z. Di, H. V. Jones, P. R. Dolan, S. M. Fairclough, M. B. Wincott, J. Fill, G. M. Hughes, and J. M. Smith, "Controlling the emission from semiconductor quantum dots using ultra-small tunable optical microcavities," *New Journal of Physics*, vol. 14, no. 10, p. 103048, 2012.

[122] B. Hauer, C. Doolin, K. Beach, and J. Davis, "A general procedure for thermomechanical calibration of nano/micro-mechanical resonators," *Annals of Physics*, vol. 339, pp. 181–207, 2013.

[123] L. B. Freund and S. Suresh, *Thin film materials: stress, defect formation and surface evolution*. Cambridge University Press, 2004.

[124] M. de Lima Jr, R. Lacerda, J. Vilcarromero, and F. Marques, "Coefficient of thermal expansion and elastic modulus of thin films," *Journal of Applied Physics*, vol. 86, no. 9, pp. 4936–4942, 1999.

[125] R. Thielsch, A. Gatto, and N. Kaiser, "Mechanical stress and thermal-elastic properties of oxide coatings for use in the deep-ultraviolet spectral region," *Applied optics*, vol. 41, no. 16, pp. 3211–3217, 2002.

[126] J. J. Talghader, "Thermal and mechanical phenomena in micromechanical optics," *Journal of Physics D: Applied Physics*, vol. 37, no. 10, p. R109, 2004.

[127] O. Paul and H. Baltes, "Mechanical behavior and sound generation efficiency of prestressed, elastically clamped and thermomechanically driven thin film sandwiches," *Journal of Micromechanics and Microengineering*, vol. 9, no. 1, p. 19, 1999.

[128] R. S. Tucker, D. M. Baney, W. V. Sorin, and C. A. Flory, "Thermal noise and radiation pressure in mems fabry-perot tunable filters and lasers," *IEEE Journal of selected topics in quantum electronics*, vol. 8, no. 1, pp. 88–97, 2002.

[129] M. Zalalutdinov, K. L. Aubin, R. B. Reichenbach, A. T. Zehnder, B. Houston, J. M. Parpia, and H. G. Craighead, "Shell-type micromechanical actuator and resonator," *Applied Physics Letters*, vol. 83, no. 18, pp. 3815–3817, 2003.

[130] E. Epp, N. Ponnampalam, J. McMullin, and R. Decorby, "Thermal tuning of hollow waveguides fabricated by controlled thin-film buckling," *Optics express*, vol. 17, no. 20, pp. 17369–17375, 2009.

[131] C. Y. Wang and C. M. Wang, *Structural vibration: exact solutions for strings, membranes, beams, and plates*. CRC Press, 2013.

[132] W. Soedel, "A natural frequency analogy between spherically curved panels and flat plates," *Journal of Sound and Vibration*, vol. 29, no. 4, pp. 457–461, 1973.

[133] M. Williams, B. Griffin, B. Homeijer, B. Sankar, and M. Sheplak, "Vibration of post-buckled homogeneous circular plates," in *Ultrasonics Symposium, 2007. IEEE*, pp. 1617–1620, IEEE, 2007.

[134] C. Ng and R. White, "Dynamic behaviour of postbuckled isotropic plates under in-plane compression," *Journal of sound and vibration*, vol. 120, no. 1, pp. 1–18, 1988.

[135] P. H. Kim, C. Doolin, B. D. Hauer, A. J. MacDonald, M. R. Freeman, P. E. Barclay, and J. P. Davis, "Nanoscale torsional optomechanics," *Applied Physics Letters*, vol. 102, no. 5, p. 053102, 2013.

[136] S. Łukasiewicz, "Introduction of concentrated loads in plates and shells," *Progress in Aerospace Sciences*, vol. 17, pp. 109–146, 1976.

[137] R. F. Barron and B. R. Barron, *Design for thermal stresses*. John Wiley & Sons, 2011.

[138] H. M. Jensen and M. Thouless, "Effects of residual stresses in the blister test," *International Journal of Solids and Structures*, vol. 30, no. 6, pp. 779–795, 1993.

[139] R. Jones, "Remarks on the approximate analysis of the nonlinear behavior of shallow shells," *Journal of Structural Mechanics*, vol. 3, no. 2, pp. 157–161, 1974.

[140] M. R. Holmes, T. Shang, A. R. Hawkins, M. Rudenko, P. Measor, and H. Schmidt, "Micropore and nanopore fabrication in hollow antiresonant reflecting optical waveguides," *Journal of Micro/Nanolithography, MEMS, and MOEMS*, vol. 9, no. 2, pp. 023004–023004, 2010.

[141] H. Gibbs, *Optical bistability: controlling light with light*. Elsevier, 2012.

[142] P. Meystre and M. Sargent, *Elements of quantum optics*, ch. 8, pp. 209–222. Springer Science & Business Media, 2007.

[143] D. Miller, "Refractive fabry-perot bistability with linear absorption: Theory of operation and cavity optimization," *IEEE Journal of Quantum Electronics*, vol. 17, no. 3, pp. 306–311, 1981.

[144] P. Meystre, E. Wright, J. McCullen, and E. Vignes, "Theory of radiation-pressure-driven interferometers," *JOSA B*, vol. 2, no. 11, pp. 1830–1840, 1985.

[145] M. Vogel, C. Mooser, K. Karrai, and R. Warburton, "Optically tunable mechanics of microlevers," *Applied Physics Letters*, vol. 83, no. 7, pp. 1337–1339, 2003.

[146] Y. W. Hu, Y. F. Xiao, Y. C. Liu, and Q. Gong, "Optomechanical sensing with on-chip microcavities," *Frontiers of Physics*, vol. 8, no. 5, pp. 475–490, 2013.

[147] P. Pirani, G. Appenzeller-Combe, and W. Lukosz, "Thermal-expansion-induced sub-milliwatt optical bistability in air-spaced fabry-perot resonators with metal mirrors," *Optics communications*, vol. 75, no. 3-4, pp. 326–331, 1990.

[148] K. An, B. Sones, C. Fang-Yen, R. Dasari, and M. Feld, "Optical bistability induced by mirror absorption: measurement of absorption coefficients at the sub-ppm level," *Optics letters*, vol. 22, no. 18, pp. 1433–1435, 1997.

[149] C. Metzger, I. Favero, A. Ortlieb, and K. Karrai, "Optical self cooling of a deformable fabry-perot cavity in the classical limit," *Physical Review B*, vol. 78, no. 3, p. 035309, 2008.

[150] F. Marino, M. De Rosa, and F. Marin, "Canard orbits in fabry-perot cavities induced by radiation pressure and photothermal effects," *Physical Review E*, vol. 73, no. 2, p. 026217, 2006.

[151] J. M. Larkin and A. J. McGaughey, "Thermal conductivity accumulation in amorphous silica and amorphous silicon," *Physical Review B*, vol. 89, no. 14, p. 144303, 2014.

[152] H. Piller and E. Palik, *Handbook of optical constants of solids*, vol. 2. 1985.

[153] G. F. Craven and C. Mok, "The design of evanescent mode waveguide bandpass filters for a prescribed insertion loss characteristic," *IEEE Transactions on Microwave Theory and Techniques*, vol. 19, no. 3, pp. 295–308, 1971.

[154] P. W. Baumeister, "Optical tunneling and its applications to optical filters," *Applied optics*, vol. 6, no. 5, pp. 897–905, 1967.

[155] C. C. Tang, "Delay equalization by tapered cutoff waveguides," *IEEE Transactions on Microwave Theory and Techniques*, vol. 12, no. 6, pp. 608–615, 1964.

[156] A. Enders and G. Nimtz, "Photonic-tunneling experiments," *Physical Review B*, vol. 47, no. 15, p. 9605, 1993.

[157] B. Edwards, A. Alù, M. G. Silveirinha, and N. Engheta, "Reflectionless sharp bends and corners in waveguides using epsilon-near-zero effects," *Journal of Applied Physics*, vol. 105, no. 4, p. 044905, 2009.

[158] M. Povinelli, M. Ibanescu, S. G. Johnson, and J. Joannopoulos, "Slow-light enhancement of radiation pressure in an omnidirectional-reflector waveguide," *Applied physics letters*, vol. 85, no. 9, pp. 1466–1468, 2004.

[159] R. DeCorby, N. Ponnampalam, E. Epp, T. Allen, and J. McMullin, "Chip-scale spectrometry based on tapered hollow bragg waveguides," *Optics express*, vol. 17, no. 19, pp. 16632–16645, 2009.

[160] M. Giraud-Carrier, C. Hill, T. Decker, J. A. Black, H. Schmidt, and A. Hawkins, "Perforated hollow-core optical waveguides for on-chip atomic spectroscopy and gas sensing," *Applied physics letters*, vol. 108, no. 13, p. 131105, 2016.

[161] G. Bappi, J. Flannery, R. Al Maruf, and M. Bajcsy, "Prospects and limitations of bottom-up fabricated hollow-core waveguides," *Optical Materials Express*, vol. 7, no. 1, pp. 148–157, 2017.

[162] H. K. Chiu, C. H. Chang, C. H. Hou, C. C. Chen, and C. C. Lee, "Wavelength-selective filter based on a hollow optical waveguide," *Applied optics*, vol. 50, no. 2, pp. 227–230, 2011.

[163] U. Vogl, A. Saß, F. Vewinger, M. Weitz, A. Solovev, Y. Mei, and O. G. Schmidt, "Light confinement by a cylindrical metallic waveguide in a dense buffer-gas environment," *Physical Review A*, vol. 83, no. 5, p. 053403, 2011.

[164] A. J. Kruchkov, "One-dimensional bose-einstein condensation of photons in a microtube," *Physical Review A*, vol. 93, no. 4, p. 043817, 2016.

[165] W. Wang, W. Zhang, W. Xing, L. Shi, Y. Huang, and J. Peng, "A novel 3-d microcavity based on bragg fiber dual-tapers," *Lightwave Technology, Journal of*, vol. 27, no. 18, pp. 4145–4150, 2009.

[166] G. R. Hadley, J. G. Fleming, and S. Y. Lin, "Bragg fiber design for linear polarization," *Optics letters*, vol. 29, no. 8, pp. 809–811, 2004.

[167] S. Y. Chou, K. C. Hsu, N. K. Chen, S. K. Liaw, Y. S. Chih, Y. Lai, and S. Chi, "Analysis of thermo-optic tunable dispersion-engineered short-wavelength-pass tapered-fiber filters," *Journal of Lightwave Technology*, vol. 27, no. 13, pp. 2208–2215, 2009.

[168] W. Shen, X. Liu, B. Huang, Y. Zhu, and P. Gu, "The effects of reflection phase shift on the optical properties of a micro-opto-electro-mechanical system fabry-perot tunable filter," *Journal of Optics A: Pure and Applied Optics*, vol. 6, no. 9, p. 853, 2004.

[169] C. Haapamaki, J. Flannery, G. Bappi, R. Al Maruf, S. Bhaskara, O. Alshehri, T. Yoon, and M. Bajcsy, "Mesoscale cavities in hollow-core waveguides for quantum optics with atomic ensembles," *Nanophotonics*, vol. 5, no. 3, pp. 392–408, 2016.

[170] M. Kline, *Calculus: an intuitive and physical approach*. Courier Corporation, 1998.

[171] S. R. Choi, J. W. Hutchinson, and A. Evans, "Delamination of multilayer thermal barrier coatings," *Mechanics of Materials*, vol. 31, no. 7, pp. 431–447, 1999.

Appendix A

Derivations

A.1 Radius of curvature of a circular buckle

It is straightforward to derive the local RoC for a dome-shaped cavity using Eq. 2.58. The curvature of a function $y(r)$ is calculated by [170]:

$$\kappa = \frac{1}{\rho} = \frac{|y''|}{(1+y'^2)^{3/2}}. \tag{A.1}$$

Taking first and second derivatives of $\Delta(r) \approx \delta[0.2871 + 0.7129 J_0(\mu r)]$ and substituting into Eq. A.1 results in:

$$\rho(r) = \frac{\left(1 + [0.7129.\delta.J_1(\mu r)(\mu/a)]^2\right)^{3/2}}{0.7129.\delta.\left[J_0(\mu r) - J_1(\mu r)/\mu r\right].(\mu/a)^2}. \tag{A.2}$$

The minimum RoC is at the peak of the Bessel function, and is given by:

$$\mathrm{RoC}(0) = \frac{2.8}{\delta}.\left(\frac{a}{\mu}\right)^2. \tag{A.3}$$

A.2 Thermal tuning of a circular buckle

As discussed in Chapter 2, the peak height of a circular buckle, within certain limits, is given by:

$$\delta = h\sqrt{\left(1.96\left(\frac{\sigma}{\sigma_c}\right) - 1\right)}. \tag{A.4}$$

Choi *et al.* [171] showed that the biaxial compressive stress of a buckled segment is subject to a thermal change ($\Delta\Theta$) due to the difference in the coefficient of thermal expansion (CTE) between the top plate and the substrate, *i.e.*, $\Delta\alpha$. This change in stress with temperature is given by:

$$\frac{\Delta\sigma}{\Delta\Theta} = \frac{E}{1-\nu}\Delta\alpha. \tag{A.5}$$

In order to find the rate of peak height change with temperature, one can use

$$\frac{\Delta\delta}{\Delta\Theta} = \frac{\Delta\delta}{\Delta\sigma}.\frac{\Delta\sigma}{\Delta\Theta}. \tag{A.6}$$

The first term on the right hand side can be worked out from Eq. A.4, and is expressed:

$$\frac{\Delta\delta}{\Delta\sigma} \approx 0.98\frac{h^2}{\delta.\sigma_c}. \tag{A.7}$$

Substituting Eqs. A.7 and A.5 into Eq. A.6 leads to

$$\frac{\Delta\delta}{\Delta\Theta} \approx 0.8.(1+\nu)\frac{a^2}{\delta}\Delta\alpha. \tag{A.8}$$

A.3 Bistability

As discussed in Chapter 5, the temperature increase in the buckled plate can be estimated as

$$\Delta\Theta \approx P_{\text{cav}}A/G, \tag{A.9}$$

where G and A are the constant thermal conductance and the absorptance of the buckled mirror, respectively, and P_{cav} is the power of the forward component of the standing wave inside the cavity and is given by

$$P_{\text{cav}} = P_{\text{in}}T_{\text{C}}/T, \tag{A.10}$$

in which T_C is the cavity transmission given in Eq. 5.1 and T is the transmittance of the buckled mirror. Combining Eqs. A.8, A.9, and A.10, photothermal change in cavity length can be easily worked out as follows:

$$\Delta\delta = \left(\frac{\Delta\delta}{\Delta\Theta}\right)\Delta\Theta \approx \frac{0.8\,.\,(1+\nu)\,.\,a^2\,.\,\alpha\,.\,P_{\text{in}}\,.\,A}{\delta\,.\,T\,.\,G}\,.\,T_{\text{C}}\,. \tag{A.11}$$

It was also shown, in Chapter 5, that a $\Delta\lambda$ shift occurs in the maximum output of a buckled microcavity due to photothermal bistability (see Fig. 5.4). This shift is related to the maximum change in temperature at a constant input power and can be expressed

$$\Delta\lambda = \frac{\Delta\lambda}{\Delta\delta}.\frac{\Delta\delta}{\Delta\Theta}.\Delta\Theta_{\text{max}}. \tag{A.12}$$

The first term on the right hand side of Eq. A.12 can be easily worked out from the resonance condition of a Fabry-Perot resonator and is given by:

$$\frac{\Delta\lambda}{\Delta\delta} = \frac{\lambda_{\text{C}}}{\delta}, \tag{A.13}$$

where λ_C is the resonance wavelength of the cold cavity. Combining Eqs. A.9 and A.10, and replacing P_{in} by $C_E P_0$ the thermal change is written

$$\Delta\Theta \approx \frac{C_E.P_0.T_C.A}{G.T}. \tag{A.14}$$

It follows that, the maximum change in temperature is found when T_C is maximum, *i.e.*, $T_C = \psi^2$ in which ψ is the potential transmittance of the buckled mirror. Thus:

$$\Delta\Theta_{max} \approx \frac{C_E.P_0.\psi^2.A}{G.T}. \tag{A.15}$$

Therefore, substituting Eqs. A.13 and A.15 in Eq. A.12 leads to

$$\Delta\lambda = \frac{\lambda_C}{\delta}\frac{\Delta\delta}{\Delta\Theta}\Delta\Theta_{max} \approx \frac{\lambda_C}{\delta}\frac{\Delta\delta}{\Delta\Theta}\frac{A\,.\,C_E\,.\,\psi^2}{G\,.\,T}P_0. \tag{A.16}$$

The effective photothermal force was defined as:

$$F_{PT} \approx K_{eff}.\Delta\delta. \tag{A.17}$$

This equation can be re-written as

$$F_{PT} \approx K_{eff}.\left(\frac{\Delta\delta}{\Delta\Theta}\right)\Delta\Theta. \tag{A.18}$$

Substituting Eq. A.9 into Eq. A.18 leads to the following expression:

$$F_{PT} \approx K_{eff}.\left(\frac{\Delta\delta}{\Delta\Theta}\right)\frac{P_{cav}A}{G}. \tag{A.19}$$

A.4 Estimation of effective spring constant

In this section, equations to estimate the effective spring constants of buckled dome micro-cavities are derived with the help from literatures on shallow spherical shells and buckled structures. As mentioned in Chapter 4, the effective spring constant is predicated on the definition and the type of the load. Here we used $K_{eff} = F/\Delta\delta$, in which $\Delta\delta$ is the deflection of the central portion of the buckled plate arising from the load and F is a concentrated or distributed load, as described below.

A.4.1 Shell model for concentrated loads

Lukasiewicz has shown that the deflection of a shell at its midpoint undergoing a circular concentrated force (F) with radius w can be estimated by [136]:

$$\Delta\delta = \frac{\sqrt{12(1-\nu^2)}}{\pi}\frac{FR_{\mathrm{S}}}{Eh^2}\left[\underbrace{\frac{1}{w^2}+\frac{1}{w}\ker' w}_{\mathrm{I}} - \underbrace{\frac{1}{2}(1+\nu)k_{\mathrm{R}}\ln\sqrt{2k_{\mathrm{R}}}-\frac{1}{4}k_{\mathrm{R}}}_{\mathrm{II}}\right] + \underbrace{\frac{3}{5\pi}(1+\nu)(2-\nu)\frac{F}{Eh}\left[\ker w+\frac{w\ker' w}{2(2-\nu)}\right]}_{\mathrm{III}}. \quad (A.20)$$

where R_{S} is the radius of curvature of the shell, ker′ is the first derivative of Kelvin-real function [137], $w = w_1/l$ in which w_1 is the radius of the load and l is called characteristic length and is given by:

$$l = \frac{\sqrt{R_{\mathrm{S}}h}}{\sqrt[4]{12(1-\nu^2)}}, \quad (A.21)$$

and $k_{\mathrm{S}} = l^2/R_{\mathrm{S}}^2$. Based on the parameters represented in Chapter 4 for the pre-existing buckled-dome microcavities, one can find the second and third terms of Eq. A.20 are three orders of magnitude smaller than the first term. Thus, the effective spring constant can be estimated by ignoring those terms as follows:

$$K_{\mathrm{eff}} \approx \frac{\pi Eh^2}{\sqrt{12(1-\nu^2)}.R_{\mathrm{S}}.\left[1/w^2+1/w\ker' w\right]}. \quad (A.22)$$

A.4.2 Buckle model for concentrated loads

Jensen and Thouless [138] numerically calculated the central deflection of a buckled dome structure as a function of concentrated load and residual stress, and their results are depicted in Fig. A.1. From this figure, it can be found that the slope of the curves (for $3 < \sigma/\sigma_c < 10$) near the vertical axis is fairly constant and is ~ 1. Thus, the approximately constant relation between the deflection at midpoint ($W(0)$) and the point load (P) leads to an estimation of the effective spring constant as follows:

$$K_{\mathrm{eff}} \approx \frac{32\pi.E.h^3}{a^2.3(1-\nu^2)}. \quad (A.23)$$

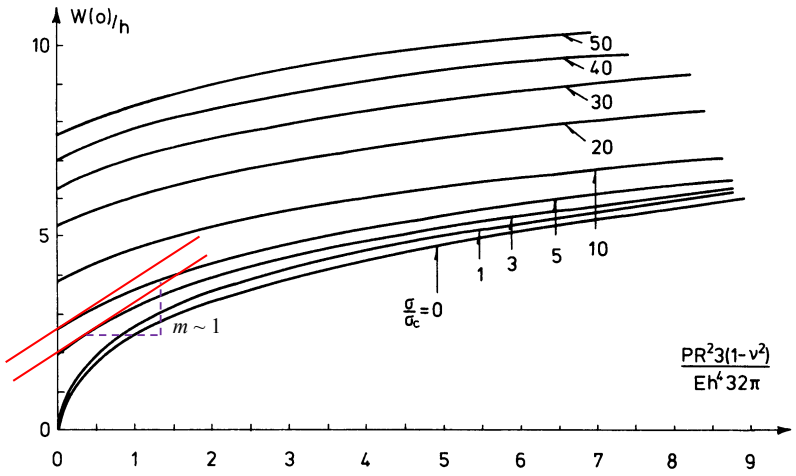

Figure A.1: Midpoint deflection (W_0) of a buckled feature as a function of point load P for various residual stresses. R is the radius of the buckled feature. Tangent lines near vertical axis are shown in red with approximately identical slope of ~ 1. Adapted from [138].

A.4.3 Shell model for distributed loads

In the work by Jones [139], the central deflection of uniformly loaded shallow shells were estimated by a simplified theory. In that work, the central deflection was estimated

$$\Delta\delta = \frac{qa^4}{64D\left[1 + (1+\nu)a^4/8R_S^2h^2\right]}, \tag{A.24}$$

where q is the uniformly distributed normal load. Thus, to estimate the effective spring constant on the basis of this model, one should replace q by $F/\pi a^2$. It follows that

$$K_{\text{eff}} = F/\Delta\delta = 64\pi.D\left[1 + (1+\nu)\left(\frac{a^4}{8R_S^2h^2}\right)\right]\Big/a^2. \tag{A.25}$$

Appendix B

Bistability modeling

In order to predict the bistability curves for a buckled-dome microcavity, one should solve Eqs. 5.1-5.2. Combining these equations results in a cubic equation as follows:

$$ax^3 + bx^2 + cx + d = 0, \tag{B.1}$$

where $x = P_{\text{out}}/P_0$ is the overall transmission, $a = K_{\text{F}}(\chi\omega/c)^2$, $b = 2K_{\text{F}}\chi\omega\theta_0/c$, $c = 1 + K_{\text{F}}\theta_0^2$, and $d = -C_{\text{E}}\psi^2$. Here, χ is defined as the coefficient of cavity height change with input power, *i.e.*, $\Delta\delta = \chi P_0$, and is given by:

$$\chi = \frac{0.8.(1+\nu).a^2.\alpha.P_0.A}{\delta.T.G}, \tag{B.2}$$

and $\theta_0 = L_{\text{eff}}(\omega - \omega_{\text{cav}})/c$.

The following Python code simulates the bistability behavior of a 150 µm-diameter dome-shaped cavity at a fixed input wavelength, set at the red-side of the resonance wavelength of a cold cavity, and over a range of input power, creating a plot identical to Fig. 5.3(b). The code, indeed, finds the roots of the cubic equation at three intervals, say at small and high input power where it only finds one real root and at middle range power where there are three real roots.

```
from numpy import *
from matplotlib.pylab import *
c = 3e8                 # speed of light
nu = 0.2                # Poissons coefficient
a = 75e-6               # radius of the buckled cavity
alpha = 3.6e-6          # coefficient of thermal expansion of the buckled plate
delta = 4.4e-6          # height of the buckled cavity
L_eff = 4.7e-6          # effective length of the cavity
R = 0.9991              # reflectance of the Bragg mirror
T = 0.00045             # transmittance of the Bragg mirror
A = 0.00045             # absorptance of the Bragg mirror
```

```
PT = T/(T+A)            # potential transmission
KF = 4*R/(1-R)**2       # coefficient of finesse
G = 2e-4                # thermal conductance
lam_cav = 1569.94e-9    # resonance wavelength for an unperturbed cavity
f_cav = c/lam_cav         # resonance frequecy of the cavity
omega_cav = 2*pi*f_cav    # angular resonance frequecy of the cavity
lam0 = lam_cav+0.13e-9    # input laser wavelength (red-detuned)
f = c/lam0              # frequency
omega = 2*pi*f          # angular frequency
CE = 0.55               # coupling efficiency
th0 = L_eff*(omega-omega_cav)/c # single pass phase shift - nearest multiple
    of 2*pi
P0 = linspace(0,0.4e-3,10000) # array for input power
d0 = -PT**2*CE                # constant for cubic equation
chi = (0.8*(1+nu)*a**2*alpha*P0*A)/(delta*T*G)
P01 = []; Pout1 = []          # input and output power for the first  power
    range with only one root
P02 = []; Pout2 = []      # input and output power for the middle power range
    (fisrt root)
P03 = []; Pout3 = []      # input and output power for the middle power range
    (second root)
P04 = []; Pout4 = []      # input and output power for the middle power range
    (third root)
P05 = []; Pout5 = []      # input and output power for the last   power range
    with only one root
root = [0]                    # root for each input power
qp = 0                        # counter for input power array
while len(root)==1:           # find the single root for the lowest power
    range
    a0 = KF*(omega/c)**2*chi[qp]**2   # first coefficient for cubic equation
    b0 = 2*KF*th0*(omega/c)*chi[qp]   # second coefficient for cubic equation
    c0 = 1+KF*th0**2        # third coefficient for cubic equation
    coeff = [a0,b0,c0,d0]           # coefficient of cubic equation
    rootsComplex = roots(coeff)     # to find roots of cubic equation
    root = rootsComplex[isreal(rootsComplex)] # to select real roots
    if len(root)==1:
        Pout1.append(root[0]*P0[qp]*1e6)
        P01.append(P0[qp]*1e6)
        qp = qp+1
while len(root)==3:
    a0 = KF*(omega/c)**2*chi[qp]**2
    b0 = 2*KF*th0*(omega/c)*chi[qp]
    c0 = 1+KF*th0**2
    coeff = [a0,b0,c0,d0]
    rootsComplex = roots(coeff)
    root = rootsComplex[isreal(rootsComplex)]
    if len(root)==3:
        Pout2.append(root[0]*P0[qp]*1e6)
        P02.append(P0[qp]*1e6)
        Pout3.append(root[1]*P0[qp]*1e6)
        P03.append(P0[qp]*1e6)
        Pout4.append(root[2]*P0[qp]*1e6)
        P04.append(P0[qp]*1e6)
        qp = qp+1
while qp < len(P0):
    a0 = KF*(omega/c)**2*chi[qp]**2
    b0 = 2*KF*th0*(omega/c)*chi[qp]
    c0 = 1+KF*th0**2
    coeff = [a0,b0,c0,d0]
```

```
    rootsComplex = roots(coeff)
    root = rootsComplex[isreal(rootsComplex)]
    if len(root)==1:
        Pout5.append(root[0]*P0[qp]*1e6)
        P05.append(P0[qp]*1e6)
        qp = qp+1
plot(P01,Pout1,'-b',P02,Pout2,'-b',P03,Pout3,'--b',P04,Pout4,'-b',P05,Pout5,'-b')
gca().get_xaxis().get_major_formatter().set_useOffset(False) # remove offset from axis label
xlabel("Input power ($\mu$W)")
ylabel("Output power ($\mu$W)")
show()
```

The following Python code simulates the bistability in a 150 µm-diameter buckled cavity at fixed input power and over 1 nm wavelength range around the cold cavity resonance. The method is identical to the above code and is based on finding the roots of the cubic equation at three different wavelength ranges.

```
from numpy import *
from matplotlib.pylab import *
c = 3e8             # speed of light
nu = 0.2            # Poissons coefficient
a = 75e-6           # radius of the buckled cavity
alpha = 3.6e-6      # coefficient of thermal expansion of the buckled plate
L_eff = 4.7e-6      # effective length of the cavity
R = 0.9991          # reflectance of the Bragg mirror
T = 0.00045         # transmittance of the Bragg mirror
A = 0.00045         # absorptance of the Bragg mirror
PT = T/(T+A)        # potential transmission
KF = 4*R/(1-R)**2   # coefficient of finesse
G = 2e-4            # thermal conductance
delta = 4.4e-6      # height of the buckled cavity
lam_cav = 1569.94e-9 # resonance wavelength for an unperturbed cavity
f_cav = c/lam_cav       # resonance frequecy of the cavity
omega_cav = 2*pi*f_cav # angular resonance frequecy of the cavity
CE = 0.55           # coupling efficiency
d0 = -PT**2*CE      # constant for cubic equation
Dlam = 1e-9         # wavelength window for simulation
lam = linspace(lam_cav-Dlam/2,lam_cav+Dlam/2,10000) # wavelength array
P0 = 105e-6         # assumend input power
chi = (0.8*(1+nu)*a**2*alpha*P0*A)/(delta*T*G) # rate of cavity height change: dL = chi * T_tot
lam1 = []; T_tot1 = [] # wavlength and total transmission for the first wavelength range with only one root
lam2 = []; T_tot2 = [] # wavlength and total transmission for the middle wavelength range (first root)
lam3 = []; T_tot3 = [] # wavlength and total transmission for the middle wavelength range (second root)
lam4 = []; T_tot4 = [] # wavlength and total transmission for the middle wavelength range (third root)
lam5 = []; T_tot5 = [] # wavlength and total transmission for the last wavelength range with only one root
root = [0]
ql = 0   # counter for input wavelength array
while len(root)==1:
```

```
    f = c/lam[ql]
    omega = 2*pi*f
    th0 = L_eff*(omega-omega_cav)/c  # single pass phase shift - nearest multiple of 2*pi
    a0 = KF*(omega/c)**2*chi**2     # first coefficient for cubic equation
    b0 = 2*KF*th0*(omega/c)*chi     # second coefficient for cubic equation
    c0 = 1+KF*th0**2                # third coefficient for cubic equation
    coeff = [a0,b0,c0,d0]           # coefficient for cubic equation
    rootsComplex = roots(coeff)
    root = rootsComplex[isreal(rootsComplex)] # to select real roots
    if len(root)==1:
        T_tot1.append(root[0])
        lam1.append(lam[ql]*1e9)
        ql = ql + 1
while len(root)==3:
    f = c/lam[ql]
    omega = 2*pi*f
    th0 = L_eff*(omega-omega_cav)/c
    a0 = KF*(omega/c)**2*chi**2
    b0 = 2*KF*th0*(omega/c)*chi
    c0 = 1+KF*th0**2
    coeff = [a0,b0,c0,d0]
    rootsComplex = roots(coeff)
    root = rootsComplex[isreal(rootsComplex)]
    if len(root)==3:
        T_tot2.append(root[0])
        lam2.append(lam[ql]*1e9)
        T_tot3.append(root[1])
        lam3.append(lam[ql]*1e9)
        T_tot4.append(root[2])
        lam4.append(lam[ql]*1e9)
        ql = ql + 1
while ql < len(lam):
    f = c/lam[ql]
    omega = 2*pi*f
    th0 = L_eff*(omega-omega_cav)/c
    a0 = KF*(omega/c)**2*chi**2
    b0 = 2*KF*th0*(omega/c)*chi
    c0 = 1+KF*th0**2
    coeff = [a0,b0,c0,d0]
    rootsComplex = roots(coeff)
    root = rootsComplex[isreal(rootsComplex)]
    if len(root)==1:
        T_tot5.append(root[0])
        lam5.append(lam[ql]*1e9)
        ql = ql + 1
plot(lam1,T_tot1,'-b',lam2,T_tot2,'-b',lam3,T_tot3,'--b',lam4,T_tot4,'--b',
    lam5,T_tot5,'-b')
gca().get_xaxis().get_major_formatter().set_useOffset(False) # remove axis label offset
xlabel("Wavelength (nm)")
ylabel("Transmission (a.u.)")
show()
```

Appendix C

COMSOL simulations

All finite element simulations in this thesis were performed using the 'Wave Optics Module', which is an add-on package for COMSOL Multiphysics allowing electromagnetic wave simulations at optical frequencies. This module consists of two physics interfaces, one of which is 'Wave Optics', suitable for systems in which wavelength is comparable with the studied structure. For the simulations represented in this thesis, a study type called 'Electromagnetic Waves, Frequency Domain' was used. Because there are numerous resources and tutorials for a variety of optical structures (available online), only specific considerations related to the simulation of the buckled structures are presented in the following.

Critical considerations in these simulations include (i) method for defining the device structure and (ii) the boundary conditions. The second order 'scattering boundary condition' (SBC) offers very low reflection up to $\sim$75° incident angle where the reflection approaches to $\sim$10 %. This would be sufficient for most of our simulations. Therefore, given its simplicity compared to the 'perfectly matched layer' (PML) boundary condition, second order SBC was used as the boundary condition.

For buckled-dome microcavities, the cross-sectional profile was extracted from 3D data measured using a ZYGO profilometer. Then, a polynomial function of degree 20 was fit to the experimental profile. This function was subsequently used to create thin layers borders, which were then converted to solids with assigned materials. Thanks to the cylindrical summery of dome-shaped cavities, we used '2D Axisymmetry' geometry design which was faster compared to the actual 3D device simulation (see Fig. C.1). In the Frequency Domain study, Eigenfrequency was chosen to find the resonance frequencies of the designed dome.

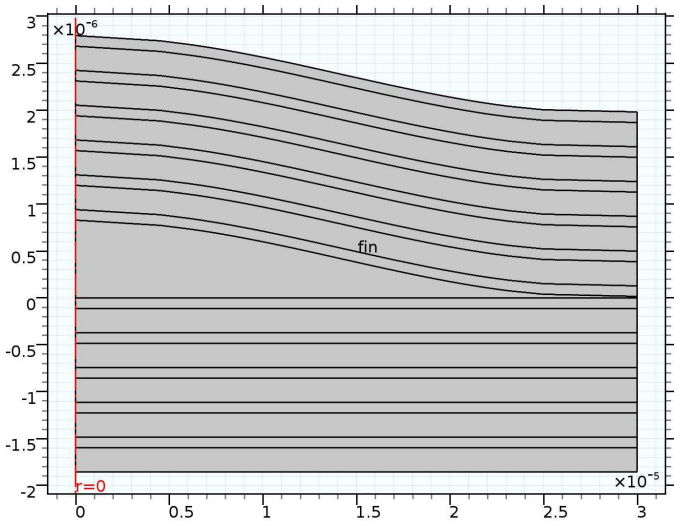

Figure C.1: Designed buckled-dome cavity in COMSOL.

The mode volume for each Eigenfrequency is calculated by defining Eq. 2.30 as a parameter in **Definitions** under **Component 1**, taking advantage of the built-in **integration** and **Maximum** functions in **Component Couplings** under **Definitions**.

Another important simulation was performed to calculate transmission and reflection in the slab-model of a dual-taper-waveguide cavity. The structure was easily made by initially creating straight lines passing through points shown in Fig. C.2(a). These lines represents the inner border of the top mirror. Parallel lines were subsequently created so as to build high- and low-index-layer thicknesses. The resulting lines were ultimately converted to a solid in which materials were assigned to the corresponding domains (see Fig. C.2(b) and C.2(c)). Ports were defined as shown in Fig. C.2(c), one of which was used to define and launch and couple a plane wave TE mode while the other was off and solely played a monitor role. Sweeping wavelength over the desired range led to S-parameters, based on which transmission and reflection were finally calculated as $|S21|^2$ and $|S11|^2$, respectively.

It should be noted that both mentioned COMSOL simulations have been validated by finite-difference-time-domain (FDTD) method using "MIT Electromagnetic Equation Propagation" (Meep) software package.

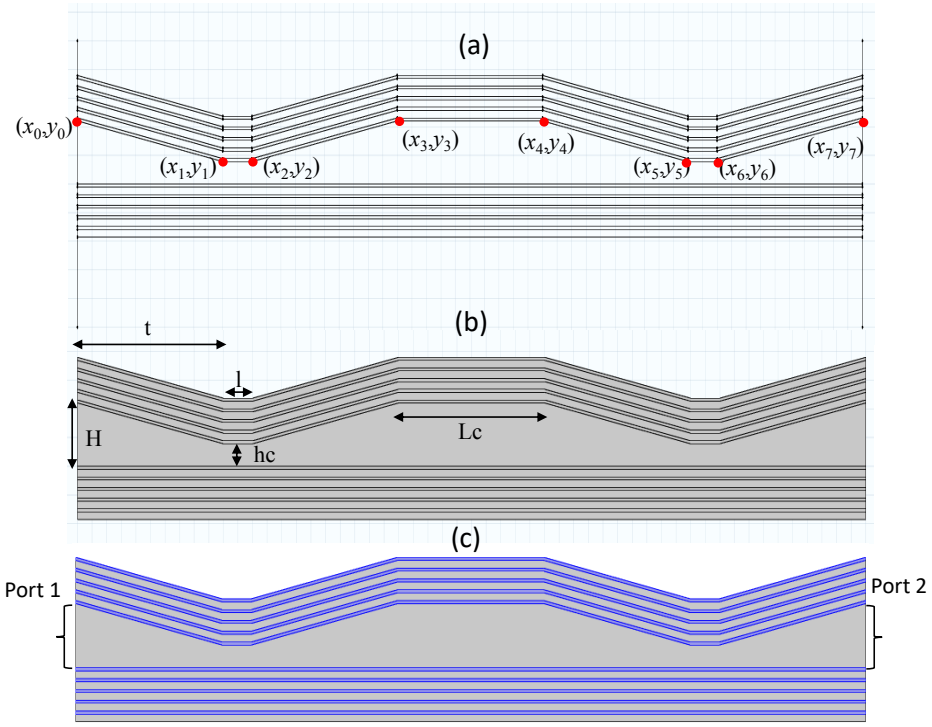

Figure C.2: Schematic of a typical dual-taper-waveguide cavity in COMSOL where (a) shows all required parametric curves along with defined points as parameters, and (b) represents the finished structure with design parameters. (c) The structure during material definition, showing selected layers related to silicon.